TECHNISCHE UNIVERSITÄT MÜNCHEN

Institut für Radiochemie

Optimisation of the PGAA instrument at FRM II for low background and 2D measurements

Lea Canella

Vollständiger Abdruck der von der Fakultät für Chemie der Technischen Universität München zur Erlangung des akademischen Grades eines
Doktors Naturwissenschaften (Dr. rer. nat)
genehmigten Dissertation.

Vorsitzender: Univ.- Prof. Dr. K. Köhler
Prüfer der Dissertation:
1. Univ.- Prof. Dr. A. Türler, Universität Bern / Schweiz
2. Univ.- Prof. Dr. M. Schuster

Die Dissertation wurde am 26.01.2011 bei der Technischen Universität München eingereicht und durch die Fakultät für Chemie am 09.03.2011 angenommen.

Technische Universität München
Institut für Radiochemie

Optimisation of the PGAA instrument at FRM II for low background and 2D measurements

Advisor: Prof. Dr. Andreas TÜRLER

Dissertation of:
Lea CANELLA

Garching 2011

Abstract

At the beginning of 2008, the new Prompt Gamma-ray Activation Analysis (PGAA) facility started operation at the Forschungs-Neutronenquelle Heinz Maier-Leibnitz (FRM II). The main characteristic of this facility is the relatively intense cold neutron beam. This property is due to the special construction of the neutron beam guide; the last 7 m are elliptically tapered, which means that the neutrons are focused to the sample. This arrangement allows for a max. neutron flux of $6.07 \cdot 10^{10}\,\mathrm{cm}^{-2}\,\mathrm{s}^{-1}$, which is currently the highest cold neutron flux worldwide. Due to this high flux, the main problem encountered was the beam background, i.e. the radiation background created from irradiation of construction materials.
The first part of this work was dedicated to the optimisation of the instrument. The goal achieved was a reduction of the background by a factor of 15.
Once the instrument was optimised, measurements were dedicated to special elements like Cd, Sm, Eu, and Gd, that have very good characteristics for this method and to archaeological samples (old greek coins).
Another improvement of the instrument was the development of a 2D imaging system. A new setup was installed in order to obtain spacial information about the distribution of elements inside samples.
This imaging method was first applied on a small piece of the Allende meteorite with a different setup developed in the frame of the European Project ANCIENT CHARM. This setup was thought for 3D imaging, so conditions were not optimal for 2D mapping. With this insight a second setup was later built especially thought for this application. In particular the neutron field was reduced to a small spot of about 2x2 mm^2 and a two stage motor was built in order to allow the movement of the sample in two dimensions. Moreover, the possibility to evacuate the sample chamber was added. With this second setup the measurements on the Allende meteorite were repeated for a comparison.
The 2D-setup was also applied in the study of the new alloy U-Mo for nuclear research. Through a sputtering process, thin foils were produced from the target material. The goal of these measurements was to determine the distribution of U and Mo in these foils, and the local element ratio, in order to check the homogeneity. Nearby the foils, measurements on thin slices of the target material were also carried out in order to check eventual changes in the elemental distribution due to the sputtering process.

Zusammenfassung

Das Instrument zur Prompten Gamma Aktivierungsanalyse, PGAA, wurde im Jahr 2008 an der Forschungs-Neutronenquellen Heinz Maier-Leibnitz (FRM II) in Betrieb genommen. Mit einer maximalen Flussdichte von $6.07 \cdot 10^{10}\,\mathrm{cm^{-2}s^{-1}}$ verfügt das Instrument über einen der intensivsten kalten Neutronenstrahlen weltweit. Dies wird durch einen 7 m langen, elliptisch geformten Neutronenleiter erreicht, der den Strahl auf die Probenposition fokusiert. Bedingt durch diesen hohen Fluss entsteht durch die Aktivierung von Strukturmaterialien ein hoher Strahlungsuntergrund. Im Rahmen der Optimierung dieses Instumentes in dieser Arbeit wurde der Hintergrund auf 1/15tel der ursprünglichen Intensität reduziert.
Anschließende Messungen wurden mit archäologischen Proben durchgeführt, wobei besonderes Augenmerk auf die Elemente Cd, Sm, Eu und Gd gelegt wurde.
Ein neues Setup für zweidimensionale Messungen wurde entwickelt und installiert. Mit diesem Setup ist eine ortsaufgelöste Messung der Verteilung von Elementen innerhalb der Proben möglich. Diese Methode wurde für eine Verteilungsmessung einer gesputterten U-Mo-Folie verwendet. Das Ziel war dabei, mögliche durch den Sputterprozess bedingte Verschiebungen des U/Mo-Verhältnisses der Legierung aufzuzeigen und somit die Homogenität der produzierten Folien zu überprüfen. In diesem Zusammenhang wurde auch die Zusammensetzung des ursprünglichen Sputtertargets analysiert.
Die gleiche Methodik mit einem ähnlichen Setup wurde für eine Analyse eines Stückes des Allende-Meteoriten im Rahmen des eruopäischen ANCIENT CHARM Projektes angewendet. Dieses Setup war ursprünglich für 3D-Messungen ausgelegt und bildete die Grundlage für die oben beschriebene verbesserte 2D-Methodik. Vergleichsmessungen zeigen den Fortschritt durch den kleineren Strahlfleck (2x2 $\mathrm{mm^2}$) und die evakuierte Probenkammer.

Contents

CHAPTER 1

Introduction

"Analitycal chemistry is a scientific discipline that develops and applies methods, instruments, and strategies to obtain information on the composition and nature of the matter in space and time" by the Working Party on Analytical Chemistry of the Federation of European Chemical Society.

Nuclear activation analysis is the most known radioanalytical technique for the isotopic and elemental determination. This method is based on the reaction between the nuclei of the material and nuclear projectiles (neutrons, accelerated charged particles e.g. protons or gamma photons). This reaction can be written, for sake of simplicity, as:

target (projectile, light product) heavy product (1.1)

the light product created in the reaction can be similar to the projectile used, e. g. a neutron, proton, or a charge particle (e. g. protons, deuterons, tritons, or ^{4}He nuclei also called alpha particles). For chemical analysis the activation method involves the measurement of the amount of the light or heavy products in a known flux of projectiles and for a known time duration. The amount of the products are proportional to the number of targets atoms, thus the atom concentration. Usually these quantities are extremely small and conventional chemical methods are not usable. The measurements are then performed by nuclear physics methods.
Detection of the light products can be accomplished only during bombardment of the target; this kind of measurement is called *prompt activation analysis*. In contrast, when the heavy product is radioactive, the atom concentration can be determined through the measurement of the radioactivity. This second method is more commonly used and is called *delayed activation analysis*.
Most nuclear activation analyses use thermal neutrons as projectiles for three basic reasons:

- Neutrons are uncharged particles, thus the cross-section for activation (i. e. the probability to cause a nuclear reaction) is larger than that for charged particles.
- Since neutrons are uncharged particles, they can penetrate much deeper than charged particles and thus allow also the analysis of relatively bulky samples.
- Thermal neutrons react with most target nuclides by one reaction, namely the (n,γ) reaction. Therefore, any activated product can be formed only by one production channel.

In the following paragraphs the focus will be on the neutron activation methods, i. e. Instrumental Neutron Activation Analysis (INAA or NAA) and Prompt Gamma-ray Neutron Activation Analysis (PGNAA or PGAA) [1].

1.1 Fundamentals

The basic idea in neutron activation analysis (prompt and delayed) is to irradiate the nuclei of a sample with neutrons in order to induce nuclear reactions. The products of these nuclear reactions, usually radioactive nuclides, emit characteristic radiation that allows to identify and to quantify the isotopes under study.
Neutrons, which do not have an electric charge remain unaffected by the Coulomb-barrier of a nucleus, thus they have an higher probability to cause nuclear reactions compared to charged particles. Using these reactions, it is possible to widely investigate the composition of a material. Neutrons are usually classified according to their energies. In fig. 1.1 the energy of the neutrons and their application in research are described. The most important reaction in INAA and

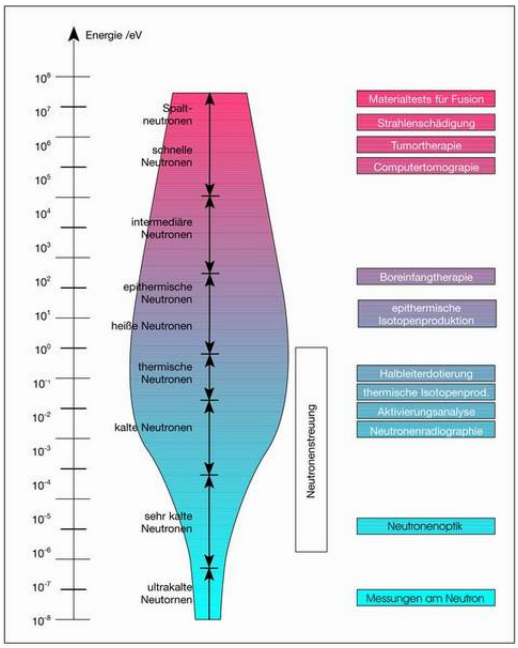

Figure 1.1: *Energy of neutrons and their application in a research reactor. The size of the colored area is proportional to the amount of neutrons available for the application at FRM II [2].*

PGAA is the radiative capture of thermal or low energy “cold” neutrons.
Whenever a nucleus absorbs a neutron a compound nucleus is formed whose excitation energy equals the binding energy plus the kinetic energy of the neutron. In fig. 1.2 a schematic view of the nuclear process is presented. The gamma-rays emitted by the de-excitation of the compound nucleus are studied by PGAA, while the gamma-rays emitted by the decay of the reaction product are studied by INAA. In both methods the elements or isotopes are analysed by measuring the energy and the intensity of the gamma-photons or emitted particles. In particular the energy of the gamma-rays emitted are characteristic for the isotope under study, and the number of

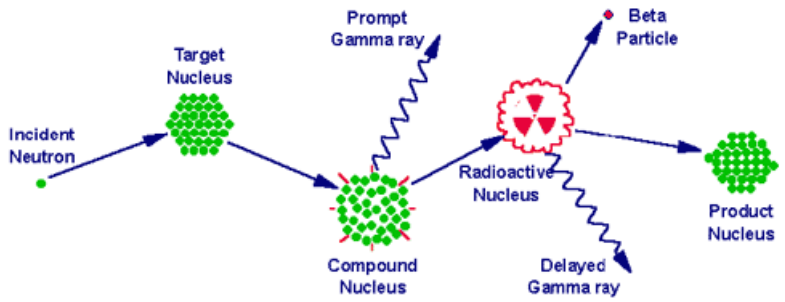

Figure 1.2: *The nuclear reaction at the basis of INAA and PGAA [3].*

emitted photons of that particular energy are proportional to the concentration of the isotope inside the sample.
INAA and PGAA are complementary, non-destructive, and multi-elemental analytical methods. The information obtained is also independent on the chemical form of the element analysed. This aspect can be regarded as an advantage as well as a disadvantage. In some cases information on the chemical form of the element is necessary, e. g. in speciation studies, which is not obtained with these two techniques [4].
PGAA complements, to some extend, the analysis of elements that cannot be measured by INAA. Since some elements cannot be determined with INAA either because the decay products have a too short half-life (< ms) or too long (months or years), or they decay without emitting gamma radiation, PGAA can represent an alternative method for the detection of these elements, e. g. light elements like H, B, C, and N. In fig. 1.3 the elements that can be detected with INAA are shown.

A big advantage of INAA is that the measurements are following the irradiations and the gamma-rays detection system has usually a low radiation background that enables a high analytical sensitivity, i. e. low detection limits. In fact this method is widely used in trace and ultra-trace elemental analysis because of this property. Moreover, the irradiations for INAA usually take place in the reactor core where a high neutron flux is available. In table 1.1 the detection limits for INAA assuming irradiation in a thermal equivalent neutron flux of about $1 \cdot 10^{13}\,\mathrm{cm}^{-2}\,\mathrm{s}^{-1}$ are given.

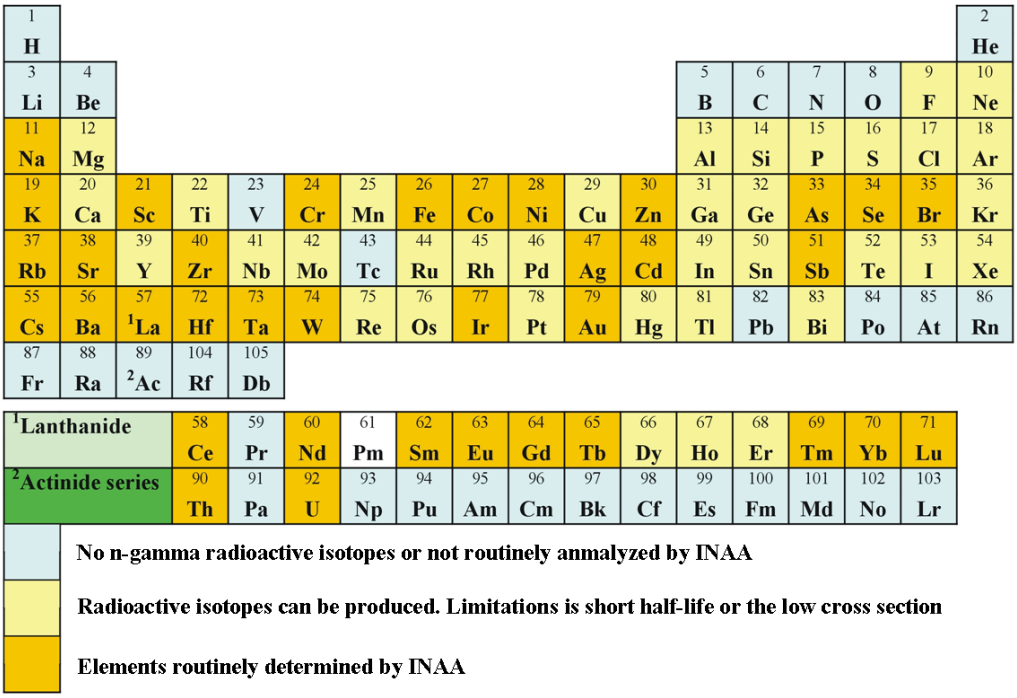

Figure 1.3: *Elements that can be detected with INAA [5].*

Detection limit [μg]	*Elements*
$1 \cdot 10^{-6}$	Dy, Eu
$1 - 10 \cdot 10^{-6}$	In, Lu, Mn
$10 - 100 \cdot 10^{-6}$	Au, Ho, Ir, Re, Sm, W
$0.1 - 1 \cdot 10^{-3}$	Ag, Ar, As, Br, Cl, Co, Cs, Cu, Er, Ga, Hf, I, La, Sb, Sc, Se, Ta, Tb, Th, Tm, U, V, Yb
$1 - 10 \cdot 10^{-3}$	Al, Ba, Cd, Ce, Cr, Hg, Kr, Gd, Ge, Mo, Na, Nd, Ni, Os, Pd, Rb, Rh, Ru, Sr, Te, Zn, Zr
$10 - 100 \cdot 10^{-3}$	Bi, Ca, K, Mg, P, Pt, Si, Sn, Ti, Tl, Xe, Y
$10 - 100 \cdot 10^{-3}$	Bi, Ca, K, Mg, P, Pt, Si, Sn, Ti, Tl, Xe, Y
$0.1 - 1$	F, Fe, Nb, Ne
10	Pb, S

Table 1.1: *Detection limits for INAA [3].*

In PGAA, the concurrent measurements with irradiation lower the analytical sensitivity of the technique, however, elements that are not easily measured by INAA can be well determined with this method, like for example H, B, C, N, V, and Pb. In fig. 1.4 the elements that can be determined with PGAA are shown with relative detection limits. Irradiations are in this case conducted outside the reactor core, and neutrons are "guided" from the reactor core to the samples through neutron beam guides. Thus the thermal equivalent neutron flux available is lower compared to INAA, usually it is about $1 \cdot 10^8\,\mathrm{cm}^{-2}\,\mathrm{s}^{-1}$.
The non-destructive property of the activation technique makes it suitable for archaeological samples where the continued integrity of the objects is of fundamental importance. PGAA, in

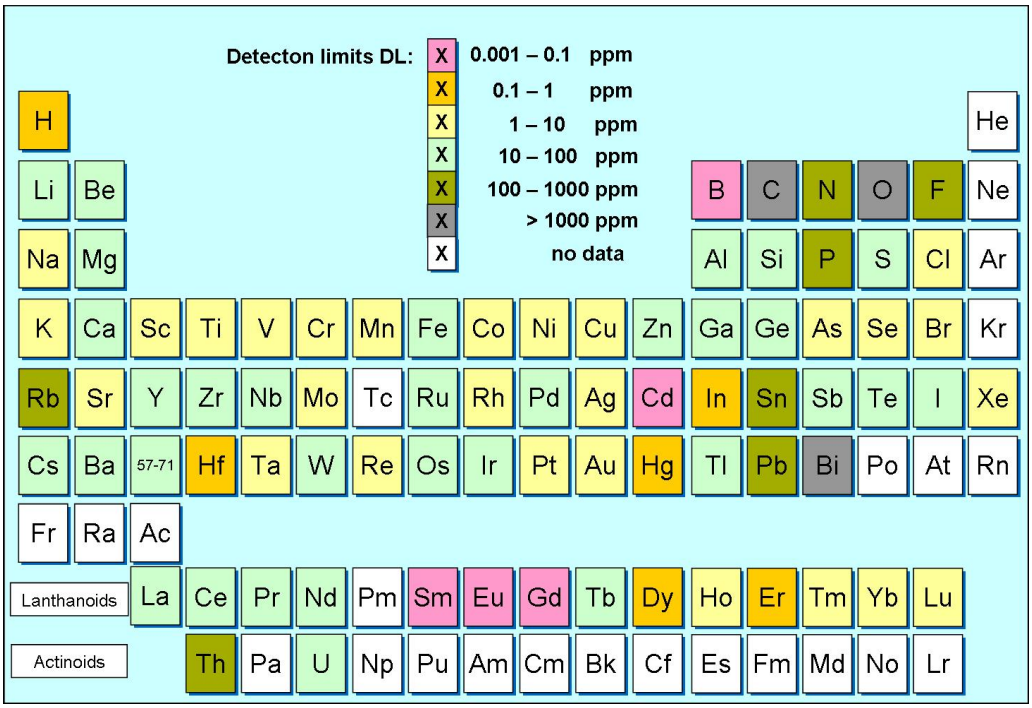

Figure 1.4: *Elements that can be detected with PGAA and their relative detection limit.*

this case is preferable to INAA. The different measurement modality (measuring position external to the reactor core) allows to measure an entire object (in case of relatively small artifacts), not requiring destructive sample taking.

1.2 Instrumentation for Activation Analysis

For INAA and PGAA the instrumentation necessary for analysis is a neutron source and a gamma-ray spectrometer. The main neutron sources available are: nuclear reactors, ion and electron accelerators (including neutron generators) and radioactive sources. In table 1.2 a list of the most commonly used neutron sources is presented.

Reaction	Average neutron energy [MeV]	Neutron yield
Photonuclear sopurces		
^{88}Y(γ,n)^{9}Be, $t_{1/2}$=106.6 d	0.16	$2.7 \cdot 10^{3}\,\mathrm{n\,s^{-1}\,GBq^{-1}}$
^{124}Sb(γ,n)^{9}Be, $t_{1/2}$=60.2 d	0.02	$5.1 \cdot 10^{3}\,\mathrm{n\,s^{-1}\,GBq^{-1}}$
Alpha emitter sources		
^{239}Pu(α,n)^{9}Be, $t_{1/2}$=2.4·10^{4} y	$3-5$	$2.7 \cdot 10^{5}\,\mathrm{n\,s^{-1}\,GBq^{-1}}$
^{226}Ra(α,n)^{9}Be, $t_{1/2}$=1600 y	3.6	$3 \cdot 10^{5}\,\mathrm{n\,s^{-1}\,GBq^{-1}}$
^{241}Am(α,n)^{9}Be, $t_{1/2}$=433 y	$3-5$	$6 \cdot 10^{4}\,\mathrm{n\,s^{-1}\,GBq^{-1}}$
Spontaneous fission source		
^{252}Cf, $t_{1/2}$=2.64 y	2.3	$2.3 \cdot 10^{12}\,\mathrm{n\,s^{-1}\,g^{-1}}$
Cockroft-Walton accelerators		
^{3}H(d,n)^{4}He	14.7	$10^{8}-10^{11}\,\mathrm{n\,s^{-1}}$
Cyclotron		
10μA of 30 MeV d on Be	Broad distribution	$2 \cdot 10^{11}\,\mathrm{n\,s^{-1}}$
Nuclear reactor		
Induced fission	Broad distribution	$10^{11}-10^{15}\,\mathrm{n\,cm^{-2}\,s^{-1}}$

Table 1.2: *Most used neutron sources for INAA [4].*

Typically, nuclear reactors are chosen as neutron sources for INAA and PGAA, where the available neutron flux is higher and thus the required irradiation times are shorter. For PGAA the introduction of neutron guides and cold neutron sources helped improving the analytical sensitivity, because they allow the transport of neutrons from the reactor core over large distances. By using slightly curved neutron guides, the hard gamma radiation form the reactor core is eliminated, i. e. the gamma-ray spectrometer at the sample position will detect a lower radiation background [1].
The detection system is the second fundamental element for INAA or PGAA measurements. Gamma-rays are interacting with the material through 3 main processes: photoelectric effect, Compton scattering and pair production. In fig. 1.5 the processes occurring with the interaction of gamma-rays and the detector crystal and the response of the gamma spectrometer, i.e. the gamma-ray spectrum, are shown. The first gamma-ray detectors used were inorganic scintillation detectors like sodium-iodide crystals doped with Tl. In the '60s, semiconductor detectors, e.g. lithium drifted Ge-detectors or high purity Ge-detectors, were developed and they started to substitute scintillation detectors. Inorganic scintillation detectors have a high detection efficiency with respect to semiconductor detectors, but the energy resolution is poor, as can be seen in fig. 1.6. Currently, mainly semiconductor detectors, in particular high purity Ge detectors (HPGe), are in use and thanks to their superior energy resolution. This propety allows the identification of more peaks, and thus increases the quality of the measurements. In particular for PGAA, the number of gamma-lines per element are enormous and a good energy-resolved spectrometer is thus essential. However, scintillation detectors can help to reduce the Compton background, especially in PGAA measurements. In this case they are used as anti-coincidence detectors to suppress Compton scattered gamma-rays events occurring in the HPGe detector.
After the acquisition of the gamma spectrum the analysis of the peaks is performed. The energies of the gamma-lines are used to identify elements inside the sample, and their activities are used to determine their amount.

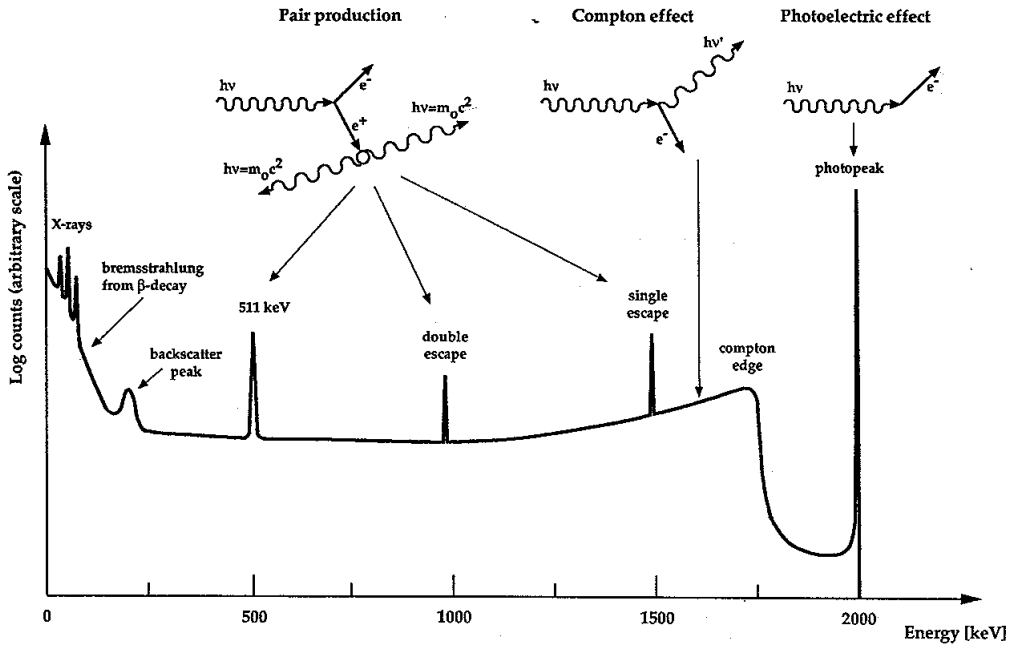

Figure 1.5: *Processes that occurs during the interaction of gamma-rays in the radiation detector and the spectrometer response, i.e. the gamma spectrum [6].*

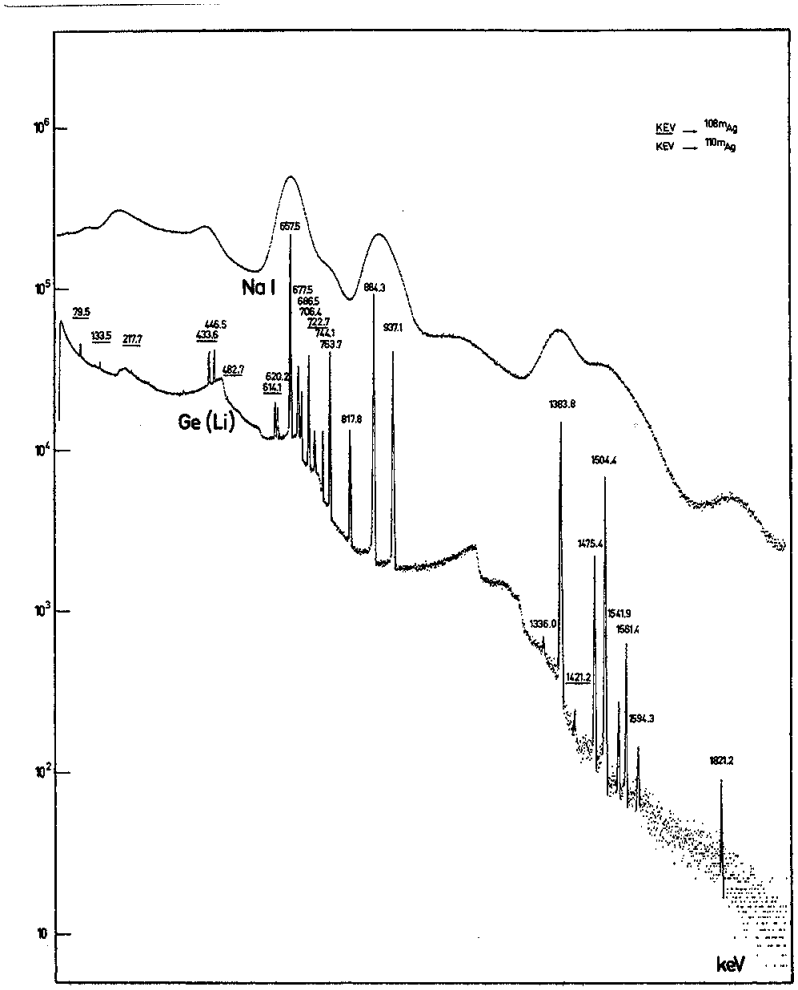

Figure 1.6: *Energy resolution difference in detector response between a NaI(Tl) scintillator detector and a Ge(Li) semiconductor detector (decay of* ^{108m}Ag *and* ^{110m}Ag*) [7].*

1.3 Aim of this work

This work is concentrating on the PGAA technique. Recently, at FRM II a new PGAA facility was installed, which has a very intense cold neutron flux. The characterisation and the optimisation of the instrument are a central part of this work. The need of such fine tuning is essential in order to deliver more accurate analytical information obtained through the measurements. The most important step was the reduction of the radiation background stemming from the irradiation of construction materials. For PGAA measurements, a low radiation background is essential in order to guarantee precise and sensitive analytical measurements.
As already mentioned, the PGAA method is sensitive to light elements as well as high cross-section elements like Gd, Sm, Eu, and Cd. The high neutron capture probability lowers the detection limits of these elements down to hundreds of ppb, and allows the detection of these elements also under difficult conditions, e.g. as thin films grown on a massive substrate. Cd can also be determined in difficult matrices, such as biological samples, where the high amount of water disturbs the measurements.
Moreover, the high neutron flux of this facility makes spatially resolved PGAA possible. Through the collimation of the neutron beam and the use of a multiple stage table, the samples can be scanned and spatial information about the distribution of the elements can be obtained. This feature was first developed in the framework of the European project ANCIENT CHARM. This ambitious project was aimed at 3D elemental distribution, and was tested in a 2D modality on a small meteorite sample. Encouraging results obtained were one of the reasons for a dedicated setup. This second setup was developed and the meteorite was used again to test the new 2D modality of PGAA. The comparison of the results on the meteorite showed a net improvement. The potential of the 2D setup is enormous.
This 2D feature turns PGAA into a very sensitive method in the determination of local concentrations, for example in alloys like UMo. UMo is a new alloy employed as fuel in nuclear reactors. From this material deposits are produced by sputtering from the target UMo material. The characterisation of both, target and samples, is very important and helps to optimise the production process.

CHAPTER 2

Prompt Gamma Activation Analysis: Fundamentals

Neutrons were discovered in 1932 by Chadwick [8]. The first observation of a gamma-ray emission during a neutron capture reaction was made in 1934 in two separate experiments, one performed by Chadwick's student Lea [9] and the second one performed by Fermi and collaborators [10]. In their experiments, the prompt gamma-line at 2223 keV from the $^{1}\mathrm{H}\,(n,\gamma)\,^{2}\mathrm{H}$ reaction was observed.
With the development of nuclear reactors, higher neutron fluxes became available and the study of prompt gamma-rays from nuclides for nuclear physics as well as elemental and isotopic analysis was carried out. The first reactor-based system for Prompt Gamma Activation Analysis (PGAA) experiments for elemental analysis was set up in 1966 by Isenhour and Morrison [11, 12] using a NaI(Tl) detector.
Improvements in analytical selectivity were accomplished in the late '60s with the development of high resolution semi-conductor detectors (lithium drifted germanium detectors), Compton suppression and pair spectrometers with both NaI(Tl) and Ge(Li) detectors.
Neutron guides and cold neutron sources helped in the further improvement of the sensitivity of this method (see chapter 1).
Starting from the '90s, the wider availability of low-energy guided neutron beams, made possible permanent and stand-alone PGAA systems for analytical purposes.[1]
Concerning the application of PGAA at the research reactor in Munich, the first PGAA experiments were carried out by Henkelmann et al. at the former FRM I with a thermal column [13, 14]. In 2005, the new research reactor FRM II started operation and was equipped with a new permanent PGAA station.

In the following chapter the theory behind the PGAA technique is described. An overview of the analytical methods is also given.[1]

2.1 Fundamentals of Prompt Gamma Activation Analysis

The most important reaction in PGAA, as already mentioned, is the radiative capture of thermal or low energy "cold" neutrons.
Whenever a nucleus absorbs a neutron a compound nucleus is formed whose excitation energy equals the binding energy plus the kinetic energy of the neutron. With slow neutrons (with an

[1] The references for the whole chapter, if not specified otherwise, are: [1, 15–18].

energy in the meV range), the capture state has a well-defined energy that equals the binding energy. The binding energy for a nucleon is between 6-10 MeV for about 80% of the stable nuclei and tends to increase with Z until Z=22 (Ti) and then to decrease. The decay of the compound nuclei takes place in about 10^{-16} s and the excited states of the product nucleus decay to the ground state in about $10^{-9} - 10^{-12}$ s, emitting a cascade of gamma-rays. These radiations are called *prompt* if their decay, following the capture reaction, takes place in a shorter time than the resolving time of the detection system, which is typically between 10 ns and 10 μs.
The prompt gamma-ray spectrum that is recorded shows two principal components: the primary component, consisting of direct 5-10 MeV gamma-rays from the capture state to lower excited states, usually below 2 MeV, and the secondary component, consisting of low-energy decays between the low-lying excited states. In fig. 2.1 the prompt gamma-rays scheme following the neutron capture by ^{59}Co is shown.

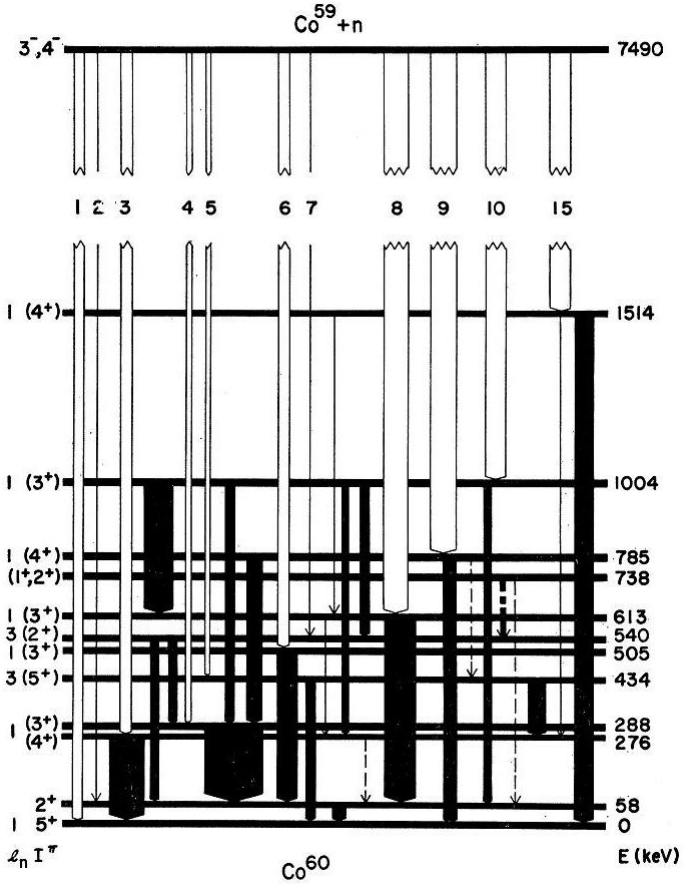

Figure 2.1: *Gamma-rays following thermal neutron capture by* ^{59}Co. *Primary transitions from the capture state are shown in white. Secondary transitions between the low-lying excited states are shown in black. The thickness of the lines are proportional to the transition intensity [19].*

Another important reaction that takes place during neutron irradiation is neutron capture with charged particle emission. This reaction is important for some light elements. The most important cases are: ^{3}He(n,p)^{3}H (its thermal cross section is 5222 b, for example this reaction is mainly used in neutron detectors), ^{6}Li(n,t)^{4}He (940 b), ^{14}N(n,p)^{14}C (1.83 b) where no gamma-rays are emitted and the ^{10}B(n,α)^{7}Li (3837 b) reaction where a gamma-ray of 478 keV is produced by the

excited level of the ^{7}Li nucleus. This reaction is also denoted by ^{10}B(n,$\alpha\gamma$)^{7}Li.
The cross section values above cited are for thermal neutron fluxes. In case of cold neutron fluxes these values generally increase because of the $1/v$-law behavior of the cross section, i.e. the cross section is inversely proportional to the velocity of the neutrons.
Other secondary processes may take place during neutron irradiation. Radiative neutron capture of epithermal neutron is a process occurring when the neutron beam as an epithermal component. The epithermal component of the neutron spectrum covers a larger energy range, and the energy of the capture state is not defined as for slow neutrons. Moreover, if a resonance is present, the capture state reaches a quasi-stationary level, which prolongates the half-life of the compound nucleus by 2-3 orders of magnitude. The levels excited in this way may present different branching ratios for the prompt gamma-rays. If the "daughter" nucleus after the capture is radioactive, the delayed gamma-rays produced in the decay can interfere with the prompt spectrum. This process is actually the fundamental process in Neutron Activation Analysis. Another effect, which produces to some extend "delayed" gamma-rays, is the isomeric transition. In this process the prompt gamma cascade can be delayed by metastable levels. Transitions with a half-life of more than 1 μs can be considered isomeric, usually half-lives for isomeric transitions are between seconds and hours. Neutron induced fission is a particular effect that can be observed when a fissile material, like ^{235}U is irradiated. In this case, a large number of fission products are produced and they decay with delayed and prompt gamma radiation with a total energy of 15 MeV/fission. Neutrons can interact with nuclei also through elastic and inelastic scattering events. Elastic scattering usually changes the direction and the energy of the incoming neutrons and this is the main process in neutron thermalisation. At low neutron energies, if the sample has a crystalline structure, neutrons undergo to so-called Bragg scattering effect that scatters neutron of a particular wavelength into a preferential direction. This effect is generally used to produce mono-energetic neutron beams. In contrast inelastic scattering occurs in presence of fast, i.e. energetic, neutrons. This process can happen only if the neutrons have an energy that is higher than the energy of the first excited state of the nucleus (threshold energy). If the neutron beam carries also a fast component, nuclear reaction with fast neutrons may take place. In this case, particle emission usually occurs. These reactions have generally a threshold energy, which is characteristic for the irradiated material. Following all the above mentioned processes, other secondary reactions may take place, e.g. characteristic X-rays can be emitted during or following the activation.
Fast charged particles, emitted in some neutron capture reactions, may produce secondary fast neutrons. This happens with high probability following the ^{6}Li(n,t)^{4}He reaction, where α-particles and fast tritons are released, causing secondary (t,n)- or (α,n)-reactions on ^{6}Li and ^{7}Li generating fast neutrons with energies up to 15 MeV. Another source of secondary fast neutrons are fissile materials. In this case fission neutrons are produced.
Annihilation radiation (511 keV) is almost always produced during a PGAA measurement, from β^{+} particles produced by some activation products but the main source is the pair production process.
When the radiation source is close to the detector, multiple Compton scattering of gamma-rays may occur increasing the Compton continuum in the low-energy range.

2.2 PGAA in equations

PGAA is mainly based on the radiative neutron capture reaction, therefore the most basic equation for this process is the reaction rate R:

$$R = \int_{E_{\min}}^{E_{\max}} N_0 \, \theta \, \sigma(E) \, \phi(E) \, dE, \tag{2.1}$$

where $\sigma(E)$ is the differential cross section, $\phi(E)dE$ is the differential flux density or fluence rate of particles with kinetic energy between E and $E + dE$, θ is the isotopic abundance of the irradiated element and N_0 is the atomic density which is connected with the mass m of the sample through the relation:

$$N_0 = \frac{m}{M} N_a, \tag{2.2}$$

M is the atomic mass of the element and N_a Avogadro's number ($6.022 \cdot 10^{23}$). This equation is valid if the target is thin and all absorption effects are negligible.
For thermal neutrons, the cross section is inversely proportional to the velocity of neutrons (1/v-law), the mean reaction rate can also be written as:

$$R_{th} \; = \; N_0 \, \sigma_0 \, \phi_{th}, \tag{2.3}$$

σ_0 is the isotopic cross section for the most probable neutron velocity (2200 m/s, E=0.025 eV), that corresponds to the maximum of the Maxwellian velocity distribution at room temperature 293 K and ϕ_{th} is the thermal neutron flux density.
In PGAA single gamma lines are detected. For the identification and analysis of the gamma lines it is useful to introduce the partial gamma-ray production cross section (for thermal neutrons) for the photon of a given energy E_γ:

$$\sigma_{\gamma,0} \; = \; \theta \, \sigma_0 \, P_\gamma, \tag{2.4}$$

where P_γ is the fraction of emitted gamma photons of energy E_γ per capture (i.e. emission probability). In this way, taking into account eq. 2.1, the count-rate (recorded events per time unit) ρ_γ of a given gamma detected photon is:

$$\rho_\gamma \; = \; \int_{E_{\min}}^{E_{\max}} \epsilon(E_\gamma) \, N_0 \, \sigma_\gamma(E) \, \phi(E) \, dE \tag{2.5}$$

where $\epsilon(E_\gamma)$ is the counting efficiency of the detector for the given energy of the photon and $\sigma_\gamma(E)$ is the quantity defined in eq. 2.4. In most real cases, the samples might not be considered as ideally thin. In this case the modification of the neutron field and the attenuation of gamma rays within the sample must be considered. The following expression takes these effects of the sample into account:

$$\rho_\gamma \; = \; \int_{\mathrm{V}} \int_{E_{\min}}^{E_{\max}} \frac{\mu(\boldsymbol{r})}{M} \, N_a \, \epsilon(E_\gamma, \boldsymbol{r}) \, \sigma_\gamma(E_n) \, \phi(E_n, \boldsymbol{r}) \, dE_n \, d\boldsymbol{r} \tag{2.6}$$

where $\mu(\boldsymbol{r})$ is the mass density as a function of the position $\boldsymbol{r}$ inside the sample (this takes also the inhomogeneity of the sample itself into account), $\phi(E_n,\boldsymbol{r})$ is the neutron flux as a function of the neutrons energy and position and considers also the inhomogeneity of the beam, self-shielding and neutron scattering of the sample, $\epsilon(E_\gamma,\boldsymbol{r})$ is the detector counting efficiency for the gamma-ray under analysis as a function of the position in the sample which corrects for gamma self-absorption and the geometric efficiency.
In reality, this complex expression can be avoided using some simplifying assumptions. The dependence of the position in the sample can be simplified if the facility has a relatively big sample-to-detector distance and, for the sake of reproducibility, a fixed geometry that allows a reproducible sample positioning in front of the detector. Moreover, the gamma self-absorption (see Appendix A) can be reduced if relatively thin and small samples are chosen. In this case, the counting efficiency can be replaced by $\epsilon(E_\gamma)$. The neutron self-shielding can also be corrected by simple expressions (see Appendix A) thus the neutron flux can be reduced to $\phi(E_n)$. Finally, for homogeneous samples, the mass density can be replaced with the real mass m.
In the next subsections, two limiting cases are presented. Both of them are described using the above mentioned approximations.

2.2.1 Thin sample approximation

When the sample is considered thin enough, i.e. transparent to neutrons, eq. 2.6 becomes:

$$\rho_\gamma,0 \;=\; \frac{m}{M}\, N_a\, \epsilon(E_\gamma) \int_{E_{\min}}^{E_{\max}} \sigma_\gamma(E_n)\, \phi(E_n)\, dE_n \;=\; \frac{m}{M}\, N_a\, \epsilon(E_\gamma)\, \sigma_{\gamma\,0}\, \phi_0 \tag{2.7}$$

In this expression, the integral can be replaced with the product of the thermal partial production cross section and ϕ_0, the so called **thermal equivalent neutron flux**, which is defined as:

$$\phi_0 \;=\; \frac{\sqrt{\pi}}{2}\, \frac{v_0}{v_T}\, \phi_r \tag{2.8}$$

where ϕ_r is the real flux, i.e. the number of neutrons per unit surface per second, the term $\sqrt{\pi}/2\, v_T$ is the mean velocity for neutrons following the Maxwellian distribution and v_0 is the velocity for thermal neutrons (i.e. 2200 m/s). This quantity is thus inversely proportional to the average velocity. The reaction rate thus increases for a cold neutron beam.

2.2.2 Black sample approximation

The second case takes into account a *black sample*. A sample is defined *black* if it absorbs all incoming neutrons. The count-rate does not depend on the cross section anymore but it is directly proportional to the number of neutrons;

$$\rho_\gamma^\infty \;=\; S\, \epsilon(E_\gamma)\, P_\gamma\, \phi_r, \tag{2.9}$$

where S is the surface area of the sample encountered by neutrons, ϕ_r is the real neutron flux and P_γ is the emission probability of the gamma line in analysis.

2.2.3 Real samples

In real cases, if the sample can be considered quite transparent to neutrons (for example an iron sample with a thickness of 10 mm transmits about 80% of the incoming thermal neutrons), eq. 2.7 can be used in the calculation. If the isotopes under study have a regular capture cross section ($1/v$-law), the thermal neutron capture cross section can also be used. For non-regular nuclides the Westcott factor, $g(T)$, has to be added to the cross section value in order to correct it.
When effects like neutron self-shielding and gamma self-absorption are not anymore negligible, correction factors have to be added (see Appendix A).

2.3 Characteristics of a PGAA measurement

PGAA is a complementary and, in few cases, competitive radioanalytical technique with respect to traditional NAA. The main properties of a PGAA measurement can be summarized as following:

- Multielemental and non-destructive analysis;
- Light elements analysis;
- Low activation of the samples;
- Bulk analysis thanks to the high penetration power of neutrons and prompt gammas.

Other characteristics that can be regarded as "disadvantages" of this method are:

- A large facility is required as neutron source;
- Lower analytical sensitivity and lower detection limits with respect to NAA;
- Prompt gamma spectra are far more complex than decay spectra;
- Scattered and fast neutrons cause detector degradation and a high amount of shielding materials is required.

The analytical results with PGAA are independent from the chemical state of the sample. If the samples, up to few grams, do not contain elements with extremely high cross-sections or a large average atomic number, they can be regarded as matrix-independent. That means, the gamma line intensities under study are not affected by the emissions of other elements in the sample.
In PGAA measurement and irradiation take place at the same time. The crossing point between the n-beam and the viewing solid angle of the collimated detector defines the active volume for the measurements. This feature can be very useful in case of the analysis of large inhomogeneous samples, e.g. archaeological samples.
The analytical sensitivity S for elements can be derived from eq. 2.6 and is dependent on the facility:

$$S = \frac{\rho_\gamma}{m} = \frac{N_a}{M}\,\sigma_{\gamma,0}\,\phi_0\,\epsilon\,(E)\,. \tag{2.10}$$

This quantity depends on the partial gamma-ray production cross section, the neutron flux and the counting efficiency. The last two terms vary from one facility to another. Generally, the

analytical sensitivity is lower than in NAA. In NAA, the samples are irradiated in an isotropic neutron field and then the decay gamma lines are later measured in a convenient geometry (almost in contact with the detector) that increases the geometric efficiency. In PGAA, the simultaneous irradiation and measurement causes a poorer geometric efficiency and generally the used neutrons are a low-divergent beam with a lower flux with respect to the flux in a reactor core. All these effects lower the analytical sensitivity of PGAA by a factor between $10^{-4} - 10^{-6}$ with respect to NAA.

2.3.1 Dynamic range and detection limits

Another characteristic of PGAA is the wide dynamic range. Any element in any matrix can be analysed within a broad concentration range. Therefore, the detection limits of elements are affected by the type and amount of the coexisting elements in the sample. Extensive work on detection limits in various matrices was published by C. Yonezawa [20]. Detection limits for 20 elements were calculated in different elemental matrices (biological, geological and environmental samples). In fig. 2.2, it is possible to see how the detection limits may vary in different matrices. From these data for B, Gd, Sm, and Cd the detection limits vary between 25 to 820 $^{ng}/_{g}$; 1.1 to

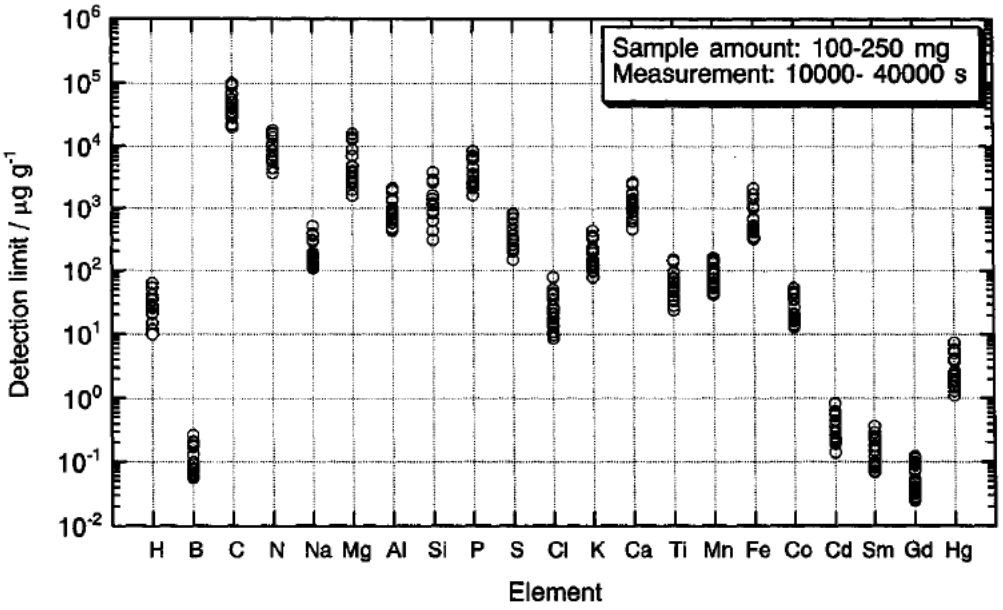

Figure 2.2: *Detection limits for 20 elements in various matrix.*

820 $^{\mu g}/_{g}$ for H, Na, S, Cl, K, Ti, Mn, Co, and Hg; and 0.031 to 10 % for C, N, Mg, Al, Si, P, Ca, and Fe.

In sea samples, the detection limits are much higher than those shown in fig. 2.2 because of the high amount of Cl in the matrix (the capture cross section for ^{35}Cl, 75.76 % isotopic abundance, is 43.60 b).

A more general expression for the detection limits (DLs) is the one defined by L. A. Currie [21]. The detection limit depends on the spectral background. The spectral background in PGAA is the spectrum of the prompt gamma-rays produced by the materials surrounding the sample

position. In a theoretical *background free* measurement, a peak can be distinguished with the help of few counts. In real cases, several hundreds of counts are necessary to distinguish a peak over the background base line. Commonly, DLs are calculated as three times the standard deviation of the number of background counts in the corresponding position of the considered peak N_{bgr}. The DL in mass units is then obtained with the following equation:

$$DL = \frac{3\sqrt{N_{bgr}}}{S\,t_m} \tag{2.11}$$

where S is the analytical sensitivity defined in eq. 2.10 and t_m is the duration of the background measurement.

2.4 Quantitative analysis

Elemental concentrations in a sample can be determined *absolutely* using eq. 2.6. In practice, this method is not so useful because of the large uncertainties in the measurement of the neutron spectrum as well as the neutron capture cross section as a function of neutron energy. Generally, a quantitative analysis is carried out using relative methods. The most common in PGAA are the *comparative method* and the *internal standardization method*, also called k_0*-method* because of its analogue to the well-known k_0-method in NAA.

2.4.1 Comparative method

With this method, the unknown concentration of an element is calculated by comparison with a well-known standard sample of the same element. The difficulty in the determination of the product of the neutron-capture count-rate and the emission probability of the gamma lines with the absolute method is overcome with the measurement of a known amount of the element under the same conditions as for the unknown sample. In this case, the analytical sensitivity defined in eq. 2.10, also called *specific count-rate*, is defined according to the measurable quantities in the standard sample:

$$S_{x,std} = \frac{N_{\gamma,x}\,/\,t_m}{m_{x,std}} \tag{2.12}$$

where $N_{\gamma,std}$ is the net peak area of the given gamma line of the analyte x in the standard sample, t_m is the measuring time and $m_{x,std}$ is the known mass of the analyte x. Once this quantity is measured, it is possible to obtain the unknown amount of the element under study in the sample according to the following expression:

$$m_{x,sample} = \frac{(N_{\gamma,x}\,/\,t_m)_{sample}}{S_{x,std}}. \tag{2.13}$$

One disadvantage of this method is that the sample and the standard material are measured in two different irradiations. Differences in the neutron flux between the sample and the measurement of the standard can be a source of error. To correct for these differences, a normalization of the peak count rate of the gamma rays of the analyte by those of a "monitor" irradiated at the same point in time is done. Examples for monitors are Ti or Cr foils.

Another approach is measuring *calibration curves*. Different standard samples are prepared with different concentrations of the analyte and then measured. The relation between the amount of the elements and the normalized peak count-rates were found to be linear. In this case, the analytical sensitivity is calculated from the slope of the curve, i.e. the calibration curve.
When using this method, it is very important to match as close as possible the elemental composition and the geometry of the standard to the sample in order to lower as much as possible all effects that affects the gamma rays detection efficiency.

2.4.2 PGAA k_0-method

As mentioned before, differences in geometry and sample composition cause problems in the correct evaluation of the gamma lines. These effects can be negligible with the use of an internal standard. Elemental determination in the *internal standardization method* is carried out using a calibration curve where the peak count ratios of the analyte and the internal standard are plotted versus the mass ratios of the analyte to the internal standard.
After the irradiation of a standard containing a known amount of analyte, x, and of the internal standard element, or comparator c, the ratio of the analytical sensitivities is obtained:

$$\frac{S_x}{S_c} = k_{r,c}(x). \tag{2.14}$$

The factor $k_{r,c}(x)$ is constant under the same experimental conditions (neutron spectra and detection efficiency). This method is also called ***ratio method***. H, Cl, Ti, Cr, Ni, Sm, and Hg have been used as comparator elements. The factors obtained with this method are not universal and they can be used only under the same experimental conditions where they were determined. By the use of the capture cross section for thermal neutrons and by normalizing for the detection efficiency, the k_r-factor become independent from the facility. The new k-factors are called k_0**-factors**, in analogy with the k_0-*method* in NAA, and are defined as follows:

$$k_{0,c} = \frac{S_x \,/\, \epsilon(E_{\gamma,x})}{S_c \,/\, \epsilon(E_{\gamma,c})} = \frac{\theta_x \, P_{\gamma,x} \, \sigma_{0,x} \,/\, M_x}{\theta_c \, P_{\gamma,c} \, \sigma_{0,c} \,/\, M_c} = \frac{\sigma_{\gamma,x} \,/\, M_x}{\sigma_{\gamma,c} \,/\, M_c} \tag{2.15}$$

where σ_γ are the partial gamma-ray production cross section as defined in eq. 2.4.
For the measurement of the k_0-factor, a very well calibrated gamma-ray spectrometer is necessary. In principle, every element can be used as a comparator. Generally the choice is H because it has just one gamma line and it is also a cross-section standard. Next to H, another comparator that is often used is Cl.
Moreover, from the k_0-values it is also possible to calculate the partial gamma ray production cross section using a well-known reference cross section and the atomic masses. Relative elemental contents of element x compared to element y in the same sample can be obtained using the expression:

$$\rho_{x:y} = \frac{S_x \,/\, \epsilon_x \, k_{0,c}(x)}{S_y \,/\, \epsilon_y \, k_{0,c}(y)}. \tag{2.16}$$

CHAPTER 3

Instrumentation 1: PGAA

Figure 3.1: *PGAA instrument at the Forschungs-Neutronenquelle Heinz Maier-Leibnitz (FRM II). Copyright W. Schürmann, Technische Universität München-TUM*

A PGAA facility consist of a neutron source, a neutron guide that directs the neutrons to the sample, a beam shutter to control the irradiation (in practice it starts and stops the irradiations), a reproducible sample positioning system, a gamma-ray spectrometer, a beam stopper and shielding to protect the detector and of course personnel from neutrons and gamma radiation. All around the world there are few functional PGAA facilities, each one with different characteristics.
In this chapter, the focus is on the PGAA facility installed at the Forschungs-Neutronenquelle Heinz Maier-Leibnitz (FRM II). The main characteristics and the peculiarity of this facility are described in detail. The optimisation of some parameters like neutron field and gamma-ray background are described and the first indicative detection limits and sensitivities for some elements, e.g. like H, B, or Pb, are calculated.

3.1 Instrumentation

3.1.1 Neutron source and neutron guide

The present PGAA instrument was originally located at the neutron spallation source SINQ of the Paul Scherrer Institut (PSI) Villingen, Switzerland [22]. In 2003, the need of a place for a new scattering instrument and the call of the PGAA responsible Dr. J. Jolie at the Universität zu Köln were the reasons of the removal of the PGAA facility from PSI. Meanwhile in 2004, the start of the operation of the new high flux research reactor in Munich offered the opportunity to install there the existing PGAA instrument.
The neutron guide of the instrument looks at the cold source in the reactor tank. The latter one is a cooled auxiliary moderator, in which a spectrum of low-energy neutrons is generated with a Maxwell distribution centered around approximately 5 meV. The moderator consists of liquid deuterium at about 25 K. The average (integral) neutron flux density in the cold source is approximatively $3 \cdot 10^{14}\,\mathrm{cm}^{-2}\,\mathrm{s}^{-1}$ (at a nominal reactor power of 20 MW; perturbed by flux depression), resulting in a cold neutron flux density of $9.1 \cdot 10^{13}\,\mathrm{cm}^{-2}\,\mathrm{s}^{-1}$ [2]. This generates a white spectrum of cold neutrons with an average energy of 1.83 meV or in wavelength units 6.7 Å and with a cadmium ratio of 9860.
The fingerprint of this facility is the neutron beam guide. All together the distance of the instrument from the cold source is about 51 m. The first section of the neutron guide is about 41 m long and curved with a radius of 390 m. The curvature of the beam guide is necessary to avoid the direct view of the reactor core, thus eliminating the hard gamma radiation radiating from it. Furthermore, the positioning of the instrument had to be chosen according to spatial limitations in the hall. The last 6.9 m of the neutron guide are straight and elliptically tapered and further divided into two units: a fixed 5.8 m long part and a removable one of 1.1 m, also called *elliptical nose* [23].

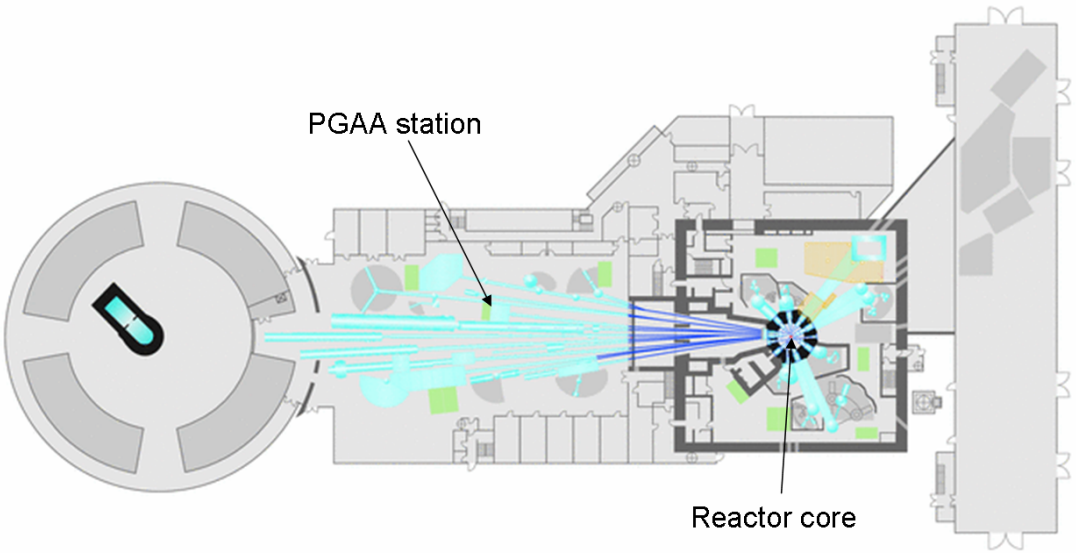

Figure 3.2: *View of the instruments at the Forschungs-Neutronenquelle Heinz Maier-Leibnitz (FRM II)*

The position of the elliptical nose defines two different geometries for measurements.
The first setup available, without the elliptical nose (setup 1, see fig.3.3(a)), has the neutron focus about 30 cm away from the end of the beam guide and the dimensions of the neutron field at the sample position are $34 \times 50\,\mathrm{mm}^2$. The maximum thermal equivalent neutron flux for this configuration is $2.42 \cdot 10^{10}\,\mathrm{cm}^{-2}\,\mathrm{s}^{-1}$ ($6.54 \cdot 10^{9}\,\mathrm{cm}^{-2}\,\mathrm{s}^{-1}$ for cold neutrons).
Using the elliptical nose (setup 2, see fig.3.3(b)) the dimensions of the neutron field are smaller (just $17 \times 19\,\mathrm{mm}^2$) but the maximal thermal equivalent neutron flux is increased about 2.5 times to $6.07 \cdot 10^{10}\,\mathrm{cm}^{-2}\,\mathrm{s}^{-1}$ ($1.64 \cdot 10^{10}\,\mathrm{cm}^{-2}\,\mathrm{s}^{-1}$ for cold neutrons) [2, 24]. In this second configuration the neutron focus was measured 9.5 cm away from the exit window. However, due to mechanical constraints, the sample can be placed only 11 cm away from the exit window. The current flux values were measured at that position.

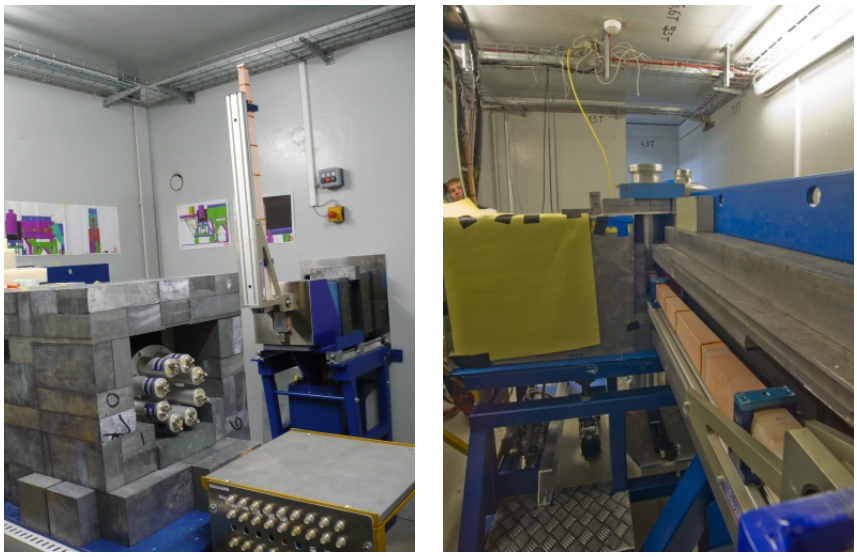

(a) Setup without elliptical nose (b) Setup with the elliptical nose

Figure 3.3: *The two different setup avilable at the PGAA instrument. Without 3.3(a) and with 3.3(b) elliptical nose.* [1]

Three attenuators (A1, A2 and A3) are installed about 20 m upstream of the sample position to allow for a more adjustable neutron flux. These attenuators are made of borated aluminum and are not in the direct view of the sample position, thus no additional gamma-ray background is created. Two of them are made out of slits (comb-like, horizontally for A1 and vertically for A2) and the third one has round holes. In table 3.1 the flux intensities for the two setups and for various attenuator configurations are given.

3.1.2 Detection system and sample environment

For the gamma-ray spectra acquisition, two standard Compton-suppressed gamma spectrometers are in use:

[1] Fig. 3.3(b) Copyright W. Schürmann, TUM.

Attenuator Setup	*Th. eq. Flux [$\mathrm{cm^{-2}\,s^{-1}}$]*	*Neutron transmission*
Setup 1, without elliptical nose		
full beam	$2.42 \cdot 10^{10}$	
A1	$4.12 \cdot 10^{9}$	17 %
A2	$4.40 \cdot 10^{9}$*	18 %
A3	$1.53 \cdot 10^{9}$	6 %
A1 + A3	$7.32 \cdot 10^{8}$	3.1 %
A2 + A3	$8.34 \cdot 10^{8}$	3.4 %
A1 + A2 + A3	$3.61 \cdot 10^{8}$	1.5 %
Setup 2, with elliptical nose		
full beam	$6.07 \cdot 10^{10}$	
A1	$7.18 \cdot 10^{9}$	12 %
A2	$7.66 \cdot 10^{9}$	13 %
A3	$2.41 \cdot 10^{9}$	4 %
A1 + A3	$1.71 \cdot 10^{9}$	2.8 %
A2 + A3	$1.92 \cdot 10^{9}$	3 %
A1 + A2 + A3	$7.84 \cdot 10^{8}$	1.3 %

Table 3.1: *Thermal equivalent neutron fluxes for the two setups and for some attenuator configurations. The relative error of the neutron flux values is 5%.The flux value A2 for setup 1 indicated by * was not measured due to technical problems. The value given is an estimated one.*

- Det.1: HPGe n-type detector with a relative efficiency of 60% (ORTEC poptop) inserted in an annulus of BGO scintillators (coaxial geometry, in fig.3.6 on the right);
- Det.2: HPGe n-type detector with a relative efficiency of 36% (Canberra) surrounded by a NaI(Tl)/BGO scintillation system (perpendicular geometry in fig.3.6 on the left).

Standard NIM (Nuclear Instrument Module) modules are used for the electronic instrumentation. The analysis of the shaped detector signals is made by an integrated ADC-MCA system (16k channels) developed at the Institut für Kernphysik, Universität zu Köln [25].
For the evaluation of the spectra and the calibration of the spectrometer (efficiency curve and non-linearity), the software Hypermet PC is in use [26, 27]. The efficiency and non-linearity calibration procedure followed for both detectors was the same as described in [28]. In fig. 3.4 the efficiency curve for the typical energy range for PGAA (from about 70 keV up to 11 MeV) is presented. The low energy region of the efficiency curve was obtained with the radioactive source ^{133}Ba and the calibrated radioactive source ^{152}Eu. For the high energy range, neutron capture reactions on N (urea), Cl (PVC - polyvinyl chloride) and Cr were used.
For the determination of the elemental composition of samples an Excel macro and the Excel sheet package called ProSpeRo (Prompt gamma Spectrum Rover) is used [29].
The sample chamber is made of Al with an inner diameter of 15 cm. The inside is covered with 90-95 % enriched ^{6}LiF-polymer [30] and the thin entrance window for neutrons is made of Zr, see fig. 3.5. On the base of the sample chamber a step motor is mounted. It allows to change up

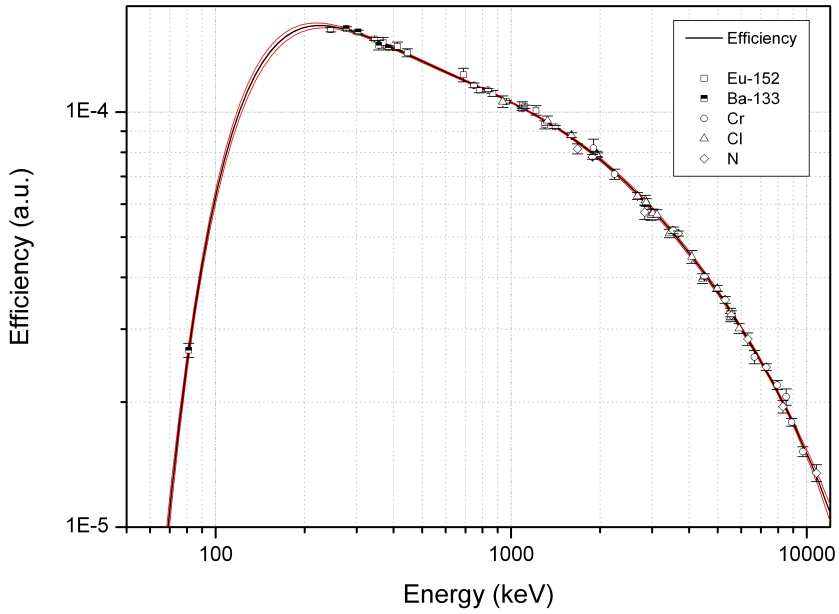

Figure 3.4: *Efficiency curve for the coaxial detector (60%).*

Figure 3.5: *View of the sample chamber in beam direction. It is possible to see the sample holder as well as the Zr neutron window behind it.*

to 6 samples mounted on a Teflon® sample holder. The samples are usually positioned inside a frame containing a grid of Teflon® strings that hold the sample itself in place.

3.1.3 Shielding

The main shielding of the instrument remained the same as at PSI (except for minor changes) and are described in detail in [22]. For high neutron-flux PGAA measurements the choice of the shielding materials is a very critical task and must be a compromise between the need to keep the beam background as low as possible and to fulfill radiation safety protection rules.
In fig.3.6 the main shielding material around the two gamma spectrometers are sketched.
Few changes were made to the coaxial spectrometer shielding (see fig. 3.6). The Pb wall in

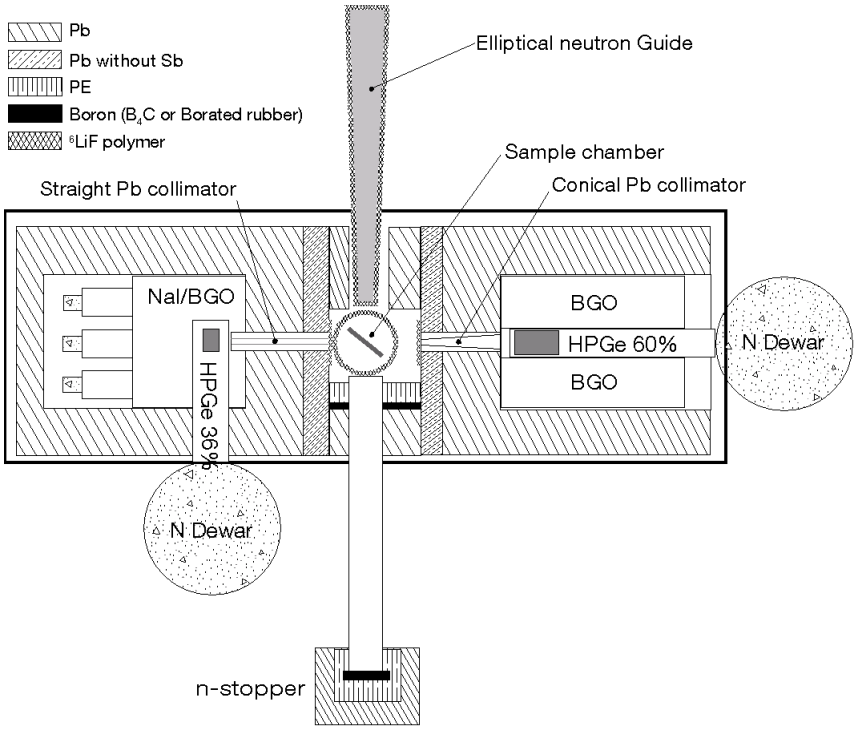

Figure 3.6: *Sketch of the shielding of the two spectrometers for the acquisition of the prompt spectra.*

front of the spectrometer was increased to 15 cm instead of 10 cm and the sample-to-detector distance was increased by about 5 cm to about 35 cm.
Due to the higher neutron flux compared to PSI, the shielding around the sample chamber had to be improved. A polyethylene wall was added between the sample chamber and the 10 cm thick Pb wall with the rear surface consisting of borated rubber, in order to slow down and catch fast neutrons produced by a secondary reaction in the ^{6}Li shielding materials (see fig.3.6).
Removable lead shielding in U-form was built for the removable elliptical nose. It is made of 10 cm thick lead covered inside with borated rubber. A sketch of the whole instrument, including the removable shielding *shells* for the elliptical nose is shown in fig.3.7.

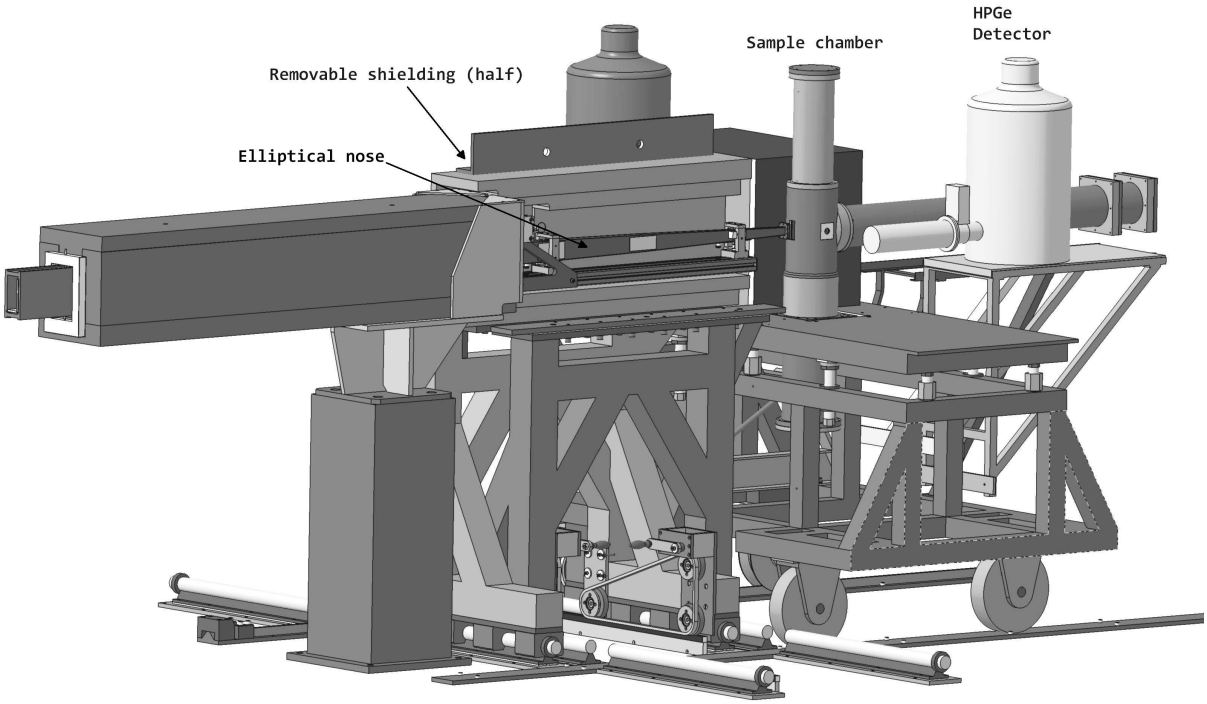

Figure 3.7: *3D-CAD-drawing of the PGAA instrument (setup 2). The removable shieldings for the elliptical nose are shown. Rails allow to shift the shieldings to both sides when the nose is not in use. The elliptical nose can then be tilted to a vertical position (setup 1).*

3.2 Background

Because PGAA measurements are done on-line, i.e. when the neutron beam is open, the acquired gamma-ray spectra are heavily influenced by neutron reactions that take place in the surrounding materials. A very low prompt gamma-ray background is necessary in order to achieve a high analytical sensitivity for real samples.
A common source of background is air, mainly due to the high amount of N (ca. 78 %). To minimize this contribution, nearly all measurements are carried out under vacuum conditions. Due to the high neutron flux, the optimisation of the total background count-rate[2] for this facility was not a trivial task.
The spectral differences between vacuum and air atmosphere inside the sample chamber are shown in fig. 3.8 .

3.2.1 Setup 2

For this setup the total count-rate at the beginning of operation was not so encouraging; it was around 3000 cps with 2 attenuators in beam (A1+A3, for the flux value see table 3.1). Efforts to reduce the background in this configuration were then carried out extensively.
In table 3.2 and fig. 3.9, the improvement of the total background count-rate with the elliptical

[2]Total count-rate: the integrated counts in the whole gamma spectra divided by the acquisition time.

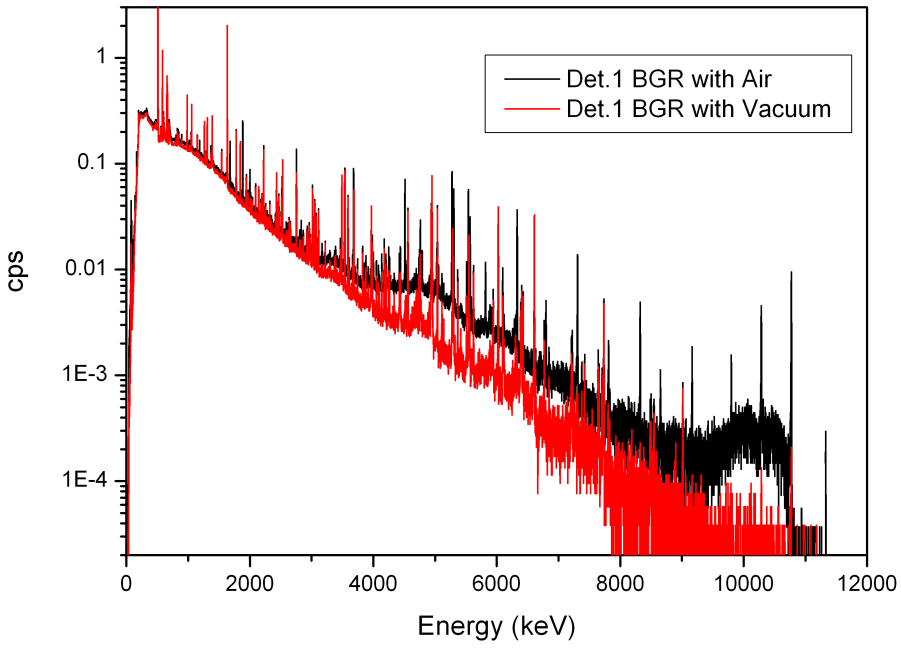

Figure 3.8: *Background Spectra with and without air.*

nose setup is presented. The chosen configurations of attenuators (A1+A3 and A2+A3) are the most common for standard PGAA measurements.

Date	*Total count-rate [cps]*	*Comments*
04/2008	3220	A1+A3, short measurement 1800s
05/2008	607	A1+A3, short meas., Pb shielding around elliptical nose
05/2008	325	A1+A2, short meas., Pb+Li shielding around elliptical nose
06/2008	339	A2+A3, new detector shieldings
01/2009	455	A2+A3, new Pb collimator in front of HPGe detector
04/2009	314	A2+A3, ^{6}LiF-polymer conical flight tube @ end of the n-guide
01/2010	192	A2+A3, new vacuum pump, 0.9 mbar instead of 15 mbar

Table 3.2: *Total count-rate for PGAA background measured with the elliptical nose. Measurements were carried out for 54 000 s, if not specified otherwise. The number of attenuators in the beam is an indirect indication for the neutron flux (see table 3.1).*

The measuring position with the elliptical nose is about 11 cm away from the end of the guide itself, thus the whole gamma spectrometer is quite near the end of the beam guide. From the analysis of the background spectra it was possible to identify the main sources of background:

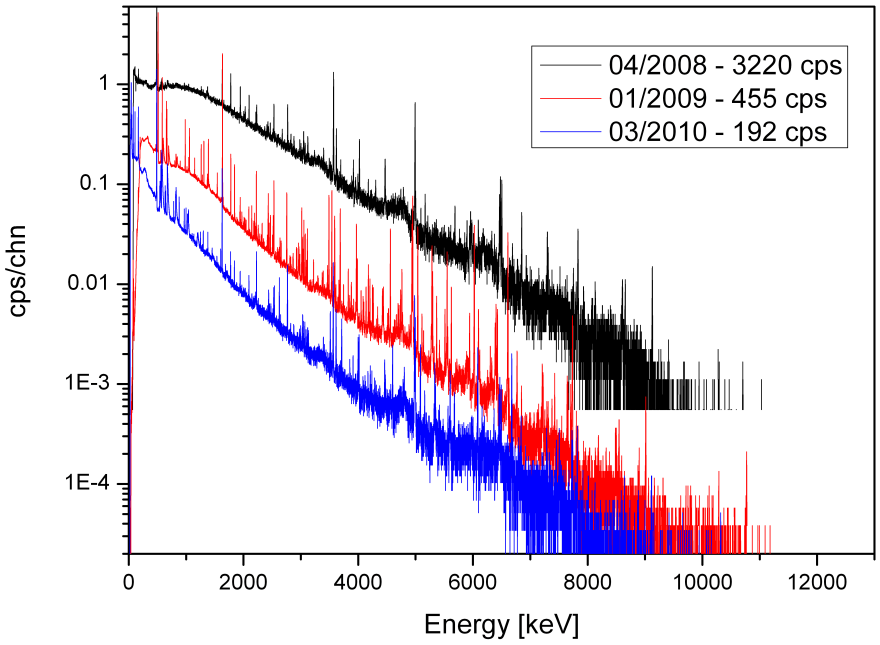

(a) Background full energy range

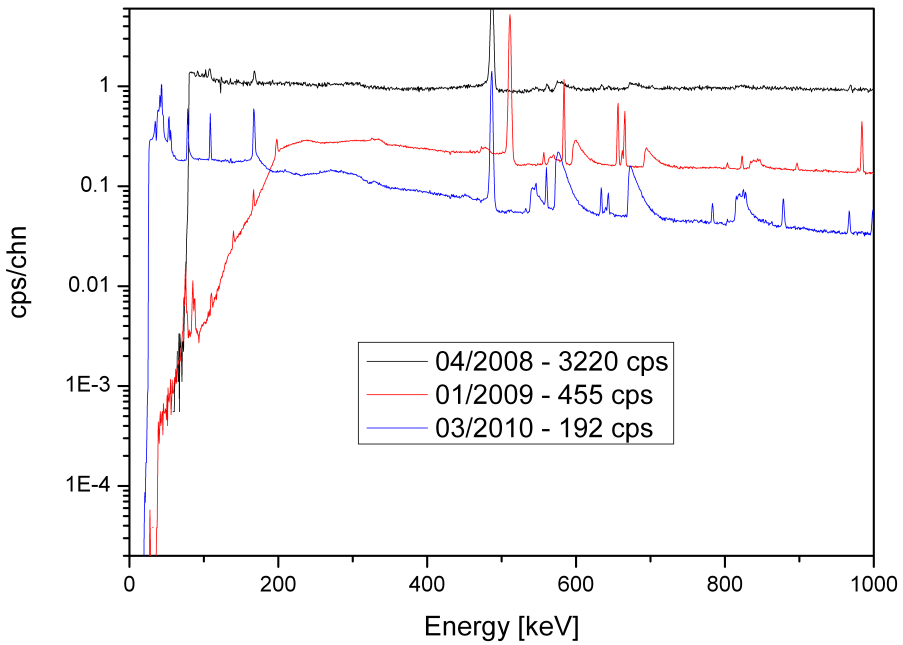

(b) Background low energy range

Figure 3.9: *Background spectra before, during and after instrument optimisation.*

Si and Na. These two elements are the main components of the neutron guide glass. In order to reduce the contribution of the glass, an extra Pb shielding was built around the end of the elliptical nose, see fig.3.10(a). The result was a reduction in the count-rate from 3000 cps to 600 cps.
An extra ^{6}LiF-polymer tube was added between the exit window of the neutron guide and the sample chamber's entrance window. This shielding cuts away most of the scattered and divergent neutrons along the path of the neutron beam. This detail brought a further improvement in the background count-rate to 325 cps.
In January 2009 the original Pb collimator (with 10 mm in diameter) in front of the coaxial detector was exchanged with a conical one (entrance diameter 10 mm, exit diameter 40 mm), see fig.3.10(b). This change optimises the use of the larger Ge crystal of this detector (volume of the Ge crystal about 1210 cm^3) with respect to the one used in the original setup at PSI. In this case the background count-rate was slightly increased from 339 cps to 455 cps.
An optimisation of the ^{6}LiF-polymer tube (fig.3.10(c)), in April 2009, between the end of the n-guide and the sample chamber brought again a reduction in the background count-rate (314 cps). The purpose was to reduce the shadow due to divergent neutrons around the useful neutron area of the beam. The optimal shape of the new tube would be elliptical according to the tapering of the neutron guide. For simplicity an easier geometry was chosen, i.e. a linear tapering shape. Dimensions were calculated based on the images of the neutron beam at the sample position.
The exchange of the vacuum pump in January 2010, brought a significant improvement of the vacuum conditions (from 10 mbar to less than 1 mbar) and of the background count-rate to only 192 cps.

3.2.2 Setup 1

In 2008, in collaboration with the PGAA group from Budapest, the first optimisation of this setup was carried out.
In this case a temporary boron carbide (B_4C) aperture was placed at the end of the neutron guide. The incoming beam was cut significantly in geometry (to about 20 x 16 mm^2) as well as in intensity ($8.37 \cdot 10^9$ cm^{-2} s^{-1} for the full beam).
The total count-rate achieved for this setup was of 580 cps.
In order to avoid such a drastic reduction of the neutron flux and in the mean time to reduce the contribution of divergent neutrons, the same solution as for setup 2 was used: a linearly tapered ^{6}LiF-polymer tube instead of the B_4C aperture was placed between the end of the neutron guide and the sample chamber entrance window. In this case the full neutron beam can be used. A total background total count-rate of 269 cps was achieved with attenuator 3 in the beam (i.e. with a thermal equivalent neutron flux of $1.53 \cdot 10^9$ cm^{-2} s^{-1}).

3.2.3 Discussion

In table 3.3 the main elements that affect background are listed. The main difference in the background count-rate with and without the elliptical nose is due to the dimension of the neutron field. For setup 1 the neutron field is larger than for setup 2 and thus the contribution of constructing and shielding materials is higher.

[3]Fig. 3.10(a) Copyright W. Schürmann, TUM

(a) Pb shielding around the elliptical nose

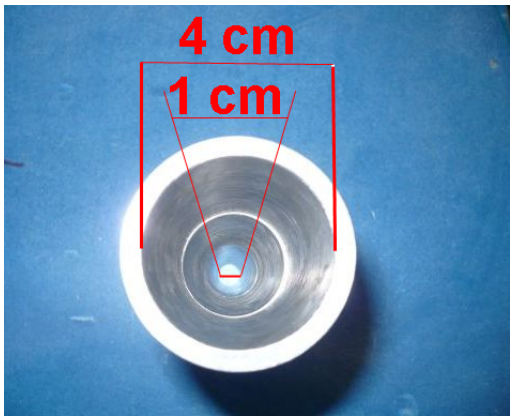

(b) Conical gamma collimator

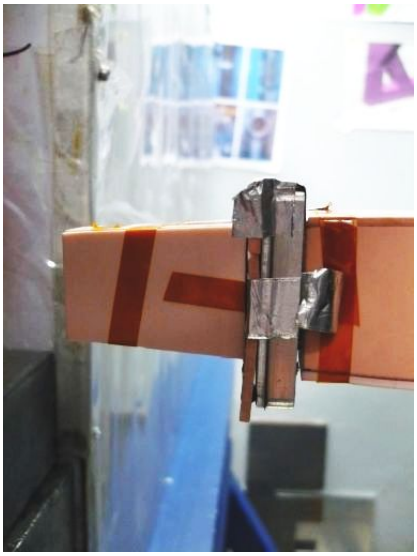

(c) LiF-polymer flight tube

Figure 3.10: *Steps for the optimisation of the background count-rate with setup 2.* [3]

H, B, Al, Ca, Fe, and Pb are the main elements in the materials of the sample chamber and of the shielding (mainly Pb). C and F are coming from the packing material for the samples which is a fluorinated ethylene propylene (FEP) foil. Na and Si are the main elements of the glass of the neutron beam guide. It is possible to notice how the neutron guide materials have a higher contribution to the background when the elliptical nose is used.

Element	*Setup 1, A3 [μg]*	*Setup 2, A2+A3 [μg]*
H	$2.80(3) \cdot 10^{-3}$	$2.34(7) \cdot 10^{-4}$
B	$1.67(2) \cdot 10^{-5}$	–
C	11.3(5)	0.33(1)
F	34.9(21)	1.03(6)
Na	$5.0(9) \cdot 10^{-3}$	$1.15(3) \cdot 10^{-2}$
Al	$4.42(10) \cdot 10^{-2}$	$5.1(2) \cdot 10^{-3}$
Si	$4.4(8) \cdot 10^{-3}$	$3.04(9) \cdot 10^{-2}$
Ca	$1.7(2) \cdot 10^{-3}$	$3.28(16) \cdot 10^{-3}$
Fe	$4.31(17) \cdot 10^{-3}$	$7.1(6) \cdot 10^{-4}$
Pb	$6.6(4) \cdot 10^{-2}$	$8.8(11) \cdot 10^{-3}$

Table 3.3: *Elements found in the background spectra without and with the elliptical nose.*

3.3 Analytical sensitivity and detection limits

Analytical sensitivities as well detection limits can be measured and evaluated as described in chapter 2.
Actually, it was not yet possible to carry out systematic measurements of the analytical sensitivity for the major elements measured at this PGAA instrument. Therefore, a calculation of the analytical sensitivities was done using eq. 2.10, with nuclear data taken from [15] and the measured neutron flux for standard PGAA measurements.
DLs for some elements were also estimated using a background spectrum with an empty FEP bag taken for 54 000 s. For the calculation of the background counts N_b inside the formula 2.11 the procedure cited in [18] was used. The interval dimensions I (in channels) chosen for the integration of the background counts was chosen as

$$I = 1.2\,w + 1 \tag{3.1}$$

where w is the full width at half maximum (FWHM) of the expected photon. The factor 1.2 is obtained form the mathematical treatment of the problem and the factor +1 is a rounding factor: one more channel should be taken into account for peak positions that do not coincide with the centre of the channel. In this case the DLs were calculated taking into account the change of the FWHM of the peaks across the large energy range of a PGAA spectrum, e.g. in the low energy region the FWHM for a peak is around 1-2 keV and at high energies it is around 7-8 keV. In table 3.4, the calculated analytical sensitivities and DLs for this facility are presented and compared with the DL obtained for the same facility when it was located at the Paul Scherrer Institute (PSI) and with the DLs of other PGAA facilities with a cold neutron beam; respectively the PGAA facility in Tokai at JAERI, in Budapest at BNC and in Gaithersburg at NIST [15, 23, 31, 32].
The DLs given in table 3.4 are just a qualitative indication on “how well” an element can be detected. For real samples there is always the influence of the main elements of the sample (sample matrix) that will modify the background for the minor or trace elements, and thus the detection limit.

Element	Energy	Sensitivity	DL FRM II	DL PSI	DL JAERI	DL BNC	DL NIST
	[keV]	[cps/mg]	[μg]	[μg]	[μg]	[μg]	[μg]
H	2 223.2	29.93	0.11	0.69	1.0	0.3	3
B	477.6	10 687.05	0.0018	0.0039	0.0023	0.0015	0.02
N	1 884.9	0.10	40.5	235	95	100	1100
N	5 269.2	0.08	11.3			60	
Si	3 539.0	0.29	14.9	63		24	400
S	841.0	1.50	7.48	23.8	9.4	10	75
S	5 420.6	0.44	1.73			10	
Cl	1 951.1	17.31	0.19			0.6	
K	770.3	3.19	2.00	7.8		4	44
Ca	1 942.7	0.86	4.89	26.7		11	140
Ti	1 381.7	12.17	0.29	2.05		0.9	10
Fe	352.3	0.91	11.7		16	20	140
Fe	7 631.1	0.36	1.98	28		9	
Ni	465.0	2.34	4.15	12	5.1	7	70
Ni	8 998.4	0.62	0.65			4	
Cd	558.3	2548.66	0.0028	0.0142	0.0070	0.006	0.05
Sm	334.0	5802.65	0.0019	0.0060	0.0030	0.003	0.03
Gd	182.0	10 131.11	0.0011	0.0035	0.0047	0.0022	0.015
Hg	368.0	201.92	0.051	0.143	0.045	0.08	0.44
Pb	7 367.8	0.02	28.1	330		150	2 600

Table 3.4: *Analytical sensitivities and detection limits for few elements and comparison with other PGAA facilities.*

3.4 Quality check

In order to check the reliability of the facility two standard reference materials (SRM) were measured in 2010 at both newly optimised positions. The SRM chosen were number 1646a, Estuarine Sediment, and number 1633b, coal fly ash, both provided by NIST (National Institute of Standards and Technology). A measurement for SRM 1646a was already performed at the beginning of 2009 with the elliptical nose (A2+A3 attenuators), the background count-rate was 455 cps (see table 3.2) and the acquisition time was 4600 s. The measurements carried out in 2010 were taken for 10800 s, with a total background count-rate of 192 cps for setup 2 (A2+A3 attenuators) and 269 cps for setup 1 (A3 attenuator in beam). The results for 1646a are presented in table 3.5.
Already in 2009 the instrument demonstrated a good performance. With the improvement of the background conditions in 2010, it was also possible to detect some trace elements like: V, Mn, Cd, Sm, and Gd. Moreover, the uncertainties were lowered compared to the measurement carried out in 2009 (this is quite evident in the determination of Cl). In the first case, uncertainties were between 3-5 % while in 2010 the maximum uncertainty was 3 %, of course, also thanks to the

Element	NIST	Ellipse 2009	Ellipse 2010	No Ell. 2010	PSI [33]
H	–	0.209(2)	0.186(3)	0.194(3)	–
B *ppm*	–	39.5(5)	45.1(6)	43.6(6)	41.8(11)
Na	0.741(17)	0.69(7)	0.690(21)	0.99(3)	–
Al	2.297(18)	2.18(9)	2.41(6)	2.17(6)	2.14(5)
Si	40.00(16)	40.1(6)	40.1(8)	40.2(8)	40.00
S	0.352(4)	0.37(2)	0.316(12)	0.312(11)	0.347(10)
Cl	–	0.66(22)	0.648(17)	0.615(17)	0.636(8)
K	0.864(16)	0.881(19)	0.87(3)	0.85(3)	0.84(2)
Ca	0.52(2)	0.65(3)	0.61(5)	0.615(25)	0.516(4)
Ti	0.456(21)	0.476(15)	0.494(12)	0.448(14)	0.473(10)
V *ppm*	44.8(8)	–	59.4(77)	64.0(64)	–
Mn *ppm*	234.5(28)	–	184.7(61)	232(12)	–
Fe	2.01(4)	2.00(5)	1.97(7)	1.90(6)	1.86(48)
Cd *ppm*	0.148(7)	–	0.12(5)	–	0.150(23)
Sm *ppm*	–	–	2.05(5)	2.11(5)	2.45(11)
Gd *ppm*	–	2.0(2)	2.4(1)	2.4(1)	2.64(8)

Table 3.5: *Standard Reference material 1646a: Estuarine sediment. Comparison between different setups (ell. stands for elliptical nose) and with the measurement made at PSI. If not specified all the values are in weight percent.*

prolonged measuring time.

For SRM 1633b results are shown in table 3.6. The measurements with the elliptical nose were taken for more than 10800 s due to software problems (acquisition time 22382 s).
It is possible to notice that for all measurements there are few differences in the determination of Na between the two different setups. In particular Na is overestimated without the elliptical nose. A possible explanation can be the difficulty to estimate precisely the amount of Na in the background spectrum.
Concerning the determination of trace elements, it is shown that for elements like Cd, Sm, and Gd (that have high capture cross section), the results are in good agreement. For the second SRM, coal fly ash 1633b, the number of trace elements found is higher compared to SRM 1646a, and the results are in quite good agreement with the certified ones again with the exception of Na.

Element	*NIST*	*Ellipse 2010*	*No Ell. 2010*	*PSI [33]*
H	–	0.086(1)	0.085(2)	–
B *ppm*	–	83.5(8)	80.0(8)	74.8(13)
Na	0.201(3)	0.39(3)	0.88(7)	–
Al	15.05(27)	16.2(3)	16.1(3)	14.25(5)
Si	23.02(8)	23.1(6)	22.7(5)	23.02
S	0.2075(11)	0.183(9)	0.207(19)	0.193(20)
K	1.95(3)	1.93(6)	2.07(5)	1.89(3)
Ca	1.51(6)	1.73(6)	1.62(6)	1.41(3)
Sc *ppm*	41[a]	36(2)	35(5)	–
Ti	0.791(14)	0.796(18)	0.853(23)	0.791(9)
V *ppm*	295.7(36)	415(21)	345(21)	–
Cr *ppm*	198.2(47)	265(29)	–	–
Mn *ppm*	131.8(17)	150(7)	140(21)	–
Fe	7.78(23)	8.14(19)	8.34(18)	7.25(12)
Ni *ppm*	120.6(18)	–	120(8)	–
Cu *ppm*	112.8(26)	140(21)	–	–
Sr *ppm*	1041(14)	1609(100)	1928(134)	–
Cd *ppm*	0.784(6)	0.69(7)	0.50(11)	0.81(4)
Sm *ppm*	20[a]	12.8(3)	13.3(3)	14.5(3)
Gd *ppm*	13[a]	14.4(7)	16.9(6)	17.7(7)

[a] *Value not certified.*

Table 3.6: *Standard Reference material 1633b: Constituent Elements in Coal Fly Ash. Comparison between different setups (ell. stands for elliptical nose) and with the measurement made at PSI. If not specified all the values are in weight percent.* [a] *value not certified*

All the optimisation steps, analytical sensitivities and DLs calculations were published in the following paper submitted and accepted in the scientific journal *Nuclear Instrumentation and Methods in Physics Reasearch Section A*, see Appendix B

CHAPTER 4

PGAA Highlights

With the optimised instrument (chapter 3), all following measurements were carried out. In this chapter, some highlights are described.
Elements like Cd, Sm, Gd are known to be non-$1/v$ nuclides, therefore, the particular k_0-values for this facility were measured. Moreover, the high cross section of these nuclides allowed particular measurements like the characterisation of EuO thin films doped with Gd and the determination of Cd down to 0.5 ppm in biological samples.
Another important field of application for PGAA is archeology. In this respect a small collection of ancient bronze coins was measured.

4.1 k_0-values for non-$1/v$ nuclides

The k_0-method has already been discussed in chapter 2. This method allows for a convenient and practical approach to multi-elemental and isotopic analysis in PGAA.
The k_0-factors can be either calculated starting from nuclear data (cross sections and emission probability of the prompt gamma-rays) of the analyte and the comparator element or directly measured. In case of regular nuclides, i.e. nuclides that have a $1/v$ cross section dependence in the cold-thermal energy range, the measured k_0-factors and the calculated ones are usually comparable. However, for some elements, the measured values have large discrepancies with the calculated values. This is the case for non-$1/v$ nuclides like ^{113}Cd, ^{149}Sm, ^{151}Eu, ^{155}Gd, and ^{157}Gd. The reason for the high cross sections of these nuclides is mainly caused by low-energy resonances, which partly overlap with the energy of the neutron spectrum used for irradiations [34, 35].
The effective cross section for a nuclide is defined as the cross section averaged over the neutron spectrum. In case of $1/v$-nuclides, this quantity is equal to the thermal cross section σ_0. When the nuclide is a non-$1/v$ absorber the effective cross section is no longer equal to σ_0. Corrections for this problem were calculated by Westcott for a Maxwellian thermal spectrum, the so-called *g-factors*. Using the Westcott convention the effective cross section is given by:

$$\hat{\sigma} = \sigma_0(g_W + rs) \tag{4.1}$$

where g_W is the Westcott g-factor, r is an index for the epithermal fraction in the neutron density and s is a parameter related to the reduced resonance integral. The r index can be obtained by measuring the Cd ratio. The Cd ratio for the PGAA facility at FRM II was determined to be

9860, which means that the epithermal fraction of the cold neutron spectrum available at the facility can be neglected. Since the Maxwellian shape of the neutron spectrum depends on the temperature, both terms g_W and s are then also dependent on the neutron temperature. The Westcott factor is defined as the ratio of the effective cross section for a Maxwellian spectrum $\hat{\sigma}_M$ to the thermal cross section σ_0:

$$g_W(T) = \frac{\hat{\sigma}_M(T)}{\sigma_0} = \frac{1}{\sigma_0 v_0}\int_0^\infty \rho_M(v,T)\sigma(v)vdv = \frac{1}{\sigma_0 v_0}\int_0^\infty \frac{4}{\sqrt{\pi}}\left(\frac{v}{v_T}\right)^3 e^{-(v/v_T)^2}\sigma(v)dv \quad (4.2)$$

where v_T is the most probable velocity for the Maxwellian distribution related to the temperature T by $v_T = v_0(T/T_0)^{1/2}$ [36].
The original set of g-values calculated by Westcott was evaluated for room temperature (293 K). Later, the tabulated values were expanded to a large temperature range, from 271 K up to 673 K, because of the different operating temperatures of different irradiation facilities [37]. The temperature range was then further expanded by Sublet et al. [38] down to 20 K. In fig. 4.1, the temperature dependence of the g-factors for the following isotopes is shown: ^{113}Cd, ^{149}Sm, ^{151}Eu, and ^{157}Gd.

For curved neutron mirror guides, the neutron spectrum can deviate from the Maxwellian

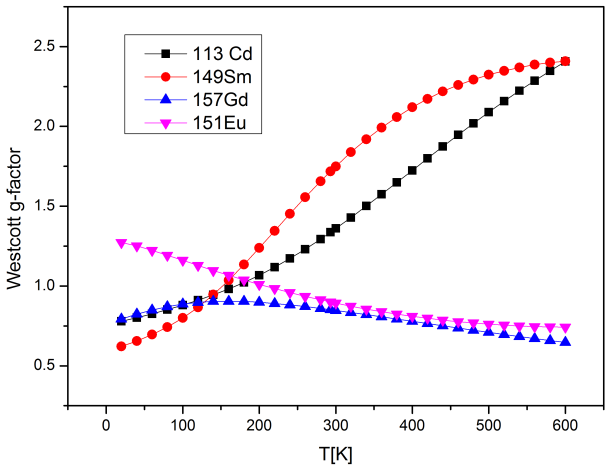

Figure 4.1: *Temperature dependence of the Westcott g-factor for* ^{113}Cd, ^{149}Sm, ^{151}Eu, *and* ^{157}Gd.

distribution, thus the tabulated Westcott g-factors are no longer valid. As the capture rate is dependent on the neutron spectrum, a generalized form is used, where the k_0-factor assumes the generalized form:

$$k_0 = \frac{S_x/\epsilon(E_{\gamma,x})}{S_c/\epsilon(E_{\gamma,c})}\cdot\frac{\hat{g}_c}{\hat{g}_x}\cdot\frac{\left(\frac{R_{Cd}}{R_{Cd}-1}\right)_c}{\left(\frac{R_{Cd}}{R_{Cd}-1}\right)_x} = k_{0(measured)}\cdot\frac{\hat{g}_c}{\hat{g}_x}\cdot\frac{\left(\frac{R_{Cd}}{R_{Cd}-1}\right)_c}{\left(\frac{R_{Cd}}{R_{Cd}-1}\right)_x} \quad (4.3)$$

where $S_{x(c)}$ are the analytical sensitivities for the analyte and the comparator, $\epsilon(E_{\gamma,x(c)})$ is the detector efficiency for the given energy of the gamma ray, $\hat{g}_{x(c)}$ is the effective g-factor and R_{Cd}

is the cadmium ratio [1]. The effective g-factors can be determined by direct calculation if the real neutron spectrum is known or by comparison of the measured k_0-factor with literature reference values. If a detailed neutron spectrum is available, the effective g-factor, only valid for one particular facility, can be calculated from the pointwise cross section using the following expression :

$$\hat{g} \equiv \frac{1}{\sigma_0 v_0} \frac{\int_0^{v_{Cd}} \rho_{th}(v)\sigma(v)vdv}{\int_0^{v_{Cd}} \rho_{th}(v)dv} = \frac{1}{\sigma_0 v_0} \int_0^{v_{Cd}} \rho_{th}(v)\sigma(v)vdv \tag{4.4}$$

The expression on the right side of eq. 4.4 is obtained if the velocity distribution $\rho_{th}(v)$ is normalized, that means the integral in the denominator of eq. 4.4 is equal to 1.

4.1.1 Measurements at the PGAA station

The current neutron spectrum (obtained with a TOF measurement described in [24]) at the PGAA facility at FRM II is shown in fig. 4.2 and compared with the cross sections for the non-$1/v$ nuclides: ^{113}Cd, ^{149}Sm, ^{151}Eu, and ^{157}Gd.

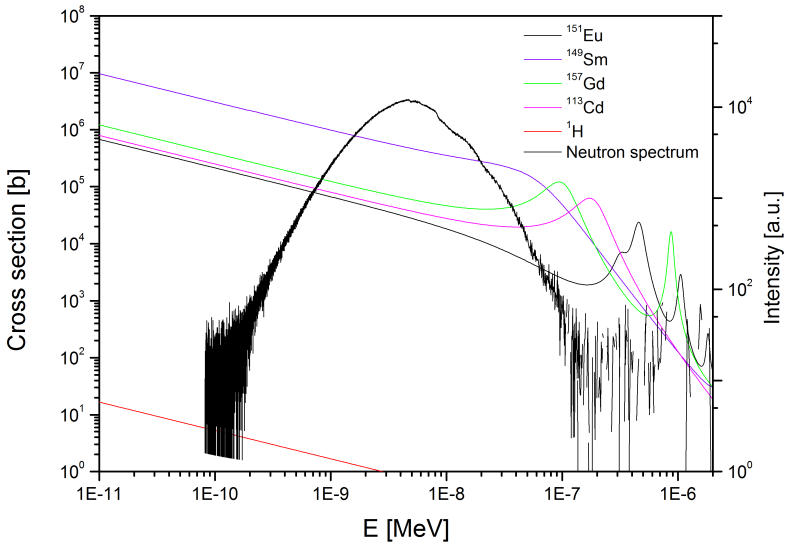

Figure 4.2: *Neutron spectrum of the PGAA facility overlapped with the cross section of the chosen isotopes.*

The k_0-values for Cd, Sm, Gd, and Eu were measured for the FRM II facility. The comparator chosen was H. Samples were prepared starting from salts of the respective elements (except for Cd). The salts were dissolved in 0.1 M nitric acid (HNO_3) in order to obtain stock solutions with concentrations around few mg/g. From these stock solutions, the concentration was diluted

[1] The cadmium ratio is used to characterise epithermal neutron fluxes. The cadmium ratio is defined as the ratio of the activity of a bare flux monitor, usually gold, and the activity of a flux monitoe covered with a Cd foil. The Cd foil (usually 1 mm thick) cuts all the thermal neutron with energies up to 0.5 eV, thus the activity of the covered monitor is given only from those neutron with energies over the Cd cutoff. Usually, in a well-thermalized neutron flux the Cd ratio is about 50. For a guided beam the ratio can be greater than 10^4.

down to tenths of ppm.
From the ratio of cross section, molar mass, isotopic abundance, and the detection efficiency for the analyte and the comparator, it is possible to estimate how much mass of the analyte and comparator are necessary for a comparable peak count-rate, i.e. the concentration of the final solution. From the calculations, ratios of 1:320 for Sm to H, 1:590 for Gd to H and 1:6 for Eu to H were found. Because Sm, Gd, and Eu have a very high cross sections, the mass ratios were kept very small in order to avoid self-shielding effects within the samples and also to keep the count-rate of the detector low enough to avoid distortions of the gamma peaks and over-saturation. The mass ratios in the final solutions were 1:4018 for Sm, 1:4844 for Gd, and 1:184 for Eu, respectively. Water, that is used as internal comparator, is known to scatter neutrons and thermalize them. This effect was kept as small as possible by using very small volumes (from 200 up to 300 μl) of the solutions for sample preparation. From the final solutions, three samples per element were prepared and sealed into 25 μm thick FEP-bags. The chemicals were purchased from Alfa Aesar. The concentrations of the solutions for Sm, Eu, and Gd as well as the samples masses are summarized in table 4.1.

Element	Salt	Stock solution conc. [mg/g]	Diluted solution conc. [μg/g]	Sample masses [mg]
Sm	$Sm(NO_3)_3 \cdot 6\,H_2O$	2.8	27.8	245; 264; 295
Eu	$Eu(NO_3)_3 \cdot 6\,H_2O$	3.4	606	244; 195; 224
Gd	$GdCl_3 \cdot 6\,H_2O$	2.3	23.1	243; 265; 226

Table 4.1: *Concentrations of the solutions and of the samples prepared for the k_0-value measurements of Sm, Gd, and Eu.*

The Cd samples were prepared starting from a standard solution (for ICP and AAS measurements) with a concentration of 999.9 mg/l. The calculated ratio for Cd to H is 1:100. The mass ratio of the standard solution is 1:111 for Cd to H. Two samples were prepared for k_0 measurements: the first one directly from the Cd solution, while the second one was obtained by dilution of the standard solution with a dilution factor of 1:2 resulting in a mass ratio of 1: 221 of Cd to H. FEP-bags were then used to pack the sample and sealed after preparation. The data for the Cd samples are reported in table 4.2.

Sample	Cd solution conc. [mg/g]	Samples masses [mg]
Cd 1	0.9999	455
Cd 2	0.505	495

Table 4.2: *Concentrations of the samples for the k_0-values measurements of Cd.*

Measurements for the liquid samples were carried out in air. As long as analyte and comparator are inside the same sample, the irradiation conditions for the different measurements are not so important in this case. All the spectra were acquired until a low statistical uncertainty (around 0.1%) of the peak count-rate for H and the main lines of the analyte were achieved. In no case the measurement time was longer than 9000 s. The k_0-factors for these elements named above were then calculated according to eq. 2.15 and the results are shown in table 4.3.
The k_0-factors obtained for the FRM II facility are different from those tabulated by the IAEA PGAA Database (last column) [36]. Moreover, the neutron spectrum of our PGAA facility can not be considered Maxwellian, because the effective g-factors obtained by the comparison of the

Element	E [keV]	$k_0(H)$ meas.	$\hat{g}_x/\hat{g}_H$	$g_W(25\,\mathrm{K})$	$g_W(293\,\mathrm{K})$	k_0 corr. (25 K)	k_0 corr. (293 K)	$k_0(H)$ [36]
^{113}Cd	558.32(3)	40.2(2)	0.802	0.787	1.337	50.5(2)	29.7(1)	50.1(8)
^{149}Sm	333.97(4)	73.7(4)	0.747	0.631	1.718	115.6(6)	42.5(2)	96.5(12)
^{149}Sm	737.44(4)	8.80(6)	0.747	0.631	1.718	13.81(9)	5.07(3)	12.03(16)
^{151}Eu	89.847(6)	19.5(3)	0.685	1.266	0.900	15.3(2)	21.5(2)	28.5(6)
^{157}Gd	181.931(4)	130.4(7)	0.927	0.803	0.852	160.8(9)	151.5(8)	139(6)
^{157}Gd	944.174(10)	54.5(3)	0.927	0.803	0.852	67.2(4)	63.3(3)	59.5(13)

Table 4.3: *Measured k_0-values for the PGAA facility at FRM II compared with the k_0-value from the IAEA PGAA Database. Effective g-factor for this PGAA facility are compared with the Westcott g-factors for a 25 K and thermal Maxwellian neutron spectrum.*

measured k_0-values with literature values are different from the tabulated Westcott-factors. In the seventh and eighth column, the Westcott factors are used to correct the measured k_0-factors. For Cd, the corrected values for a 25 K Maxwellian spectrum are pretty much in agreement with the IAEA values (discrepancy $< 1\,\%$), while for Eu none of the corrected factors are in agreement (discrepancy nearly 50 %). Moreover, the effective g-factor for Eu estimated is pretty far away from the tabulated ones. For Sm and Gd, the effective g-factors are quite near the ones previewed from Westcott, however the discrepancy between the corrected k_0-values and the literature ones is between 15-20 %. The results obtained are quite evident proof that the neutron spectra available at the PGAA station cannot be described with a Maxwellian distribution.

4.2 Determination of Eu and Gd in thin films

Spintronics is a new high-tech field where the semiconductor devices can exploit the spin degree of freedom of the conduction electrons. This new concept opens a wide range of new possibilities in the field of semiconductor-based data processing and memory applications [39]. EuO is a potential material for spintronics applications, due to its numerous magnetic properties. However, the potential of this oxide is dependent on its Curie temperature. The Curie temperature is the temperature at which a ferromagnetic or a ferrimagnetic material becomes paramagnetic. For EuO based materials this temperature is at 69 K. Efforts to improve this latter property are actually extensively made.
Several possibilities are currently studied. One of these is a charge carrier doping by either oxygen vacancies or by substituting Eu^{2+} with trivalent ions like Fe^{3+}, La^{3+}, or Gd^{3+}. For optimised doping concentration in $Eu_{1-x}B_xO$, the Curie temperature reaches 170 K for B = Gd with x = 0.04 and 180 K for B = Fe with x = 0.077 [40].
The *Zentrum für elektronische Korrelation und Magnetismus* (Universität Augsburg) is studying $Eu_{1-x}Gd_xO$ films. A systematic measurement of the charge carrier densities and Curie temperature for a wide range of doping concentrations were carried out.
These thin films are produced by molecular-beam epitaxy (MBE). EuO films are grown by heating the substrate to temperatures high enough to evaporate the unoxidized europium metal and the deposition is controlled only by the oxygen flux. This way, all the available oxygen reacts to form EuO and the excess europium evaporates leaving pure stoichiometric EuO [40, 41]. In

case of EuO(Gd) films, Eu and Gd are co-evaporated in oxygen with a background pressure of $1 \cdot 10^{-9}$ Torr. The films are grown on an $YAlO_3$ single crystalline substrate, chosen because of its insulating properties. The thickness of these films is about 35 nm.
To obtain a precise amount of dopant within the batch of EuO(Gd) films, the fluxes of Gd and Eu have to be calibrated in order to chose the desired doping concentration. To establish if the calibration was correct the films with the highest Gd concentrations were measured with PGAA to extrapolate the lower values for the other films [40].

4.2.1 EuO(Gd) and PGAA

PGAA measurements were preformed to determine the elemental ratio between Gd and Eu. These two elements are easy to determine with PGAA, even in trace amounts, thanks to their high neutron capture cross sections. Matrix effects in thin films measurements can be a considerable problem. The high amount of the substrate (hundreds of mg) with respect to the thin film (35 nm) can compromise the measurements, yielding a very high matrix background that can cover the peaks of the elements contained in the film.
The first measurements carried out were feasibility measurements. A thin film made of pure Gd, one made of pure Eu and a thin film of EuO($5\%_{wt}$Gd) on a $YAlO_3$ substrate were measured. The two main goals of these test measurements were to check if it is possible to detect Gd and Eu on the massive substrate and to define possible peak-interferences in the doped EuO film. The test was successful its result can be seen in fig. 4.3. Eu and Gd can be clearly detected.

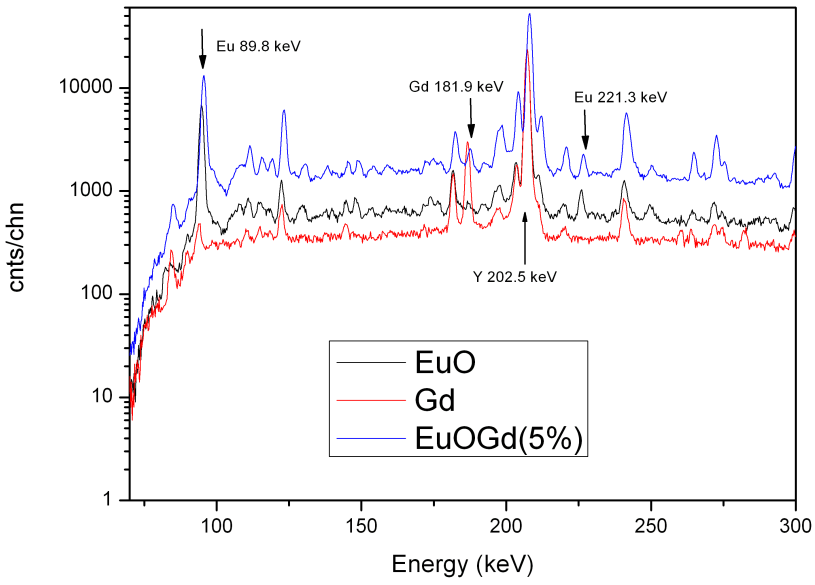

Figure 4.3: *Test measurements for EuO(Gd) films.*

The second most intense peak for Y at 202.53 keV is exactly in-between the Gd peak at 181.931 keV and the Eu peak at 221.30 keV, despite this no difficulties occur in the determination of the peaks of interest. The most intense peak for Eu at 89.847 keV is situated on the growing shoulder of the spectra. This peak would be the best choice for the ratio calculation but the electronic conditions even though they have a low threshold around 75 keV distort the low energy signal

and problems may arise for the fit of the 89.847 keV peak. In December 2009, measurements on three films with different Gd contents were carried out. The different Gd concentrations were 5 $\%_{wt}$, 8 $\%_{wt}$, and 16 $\%_{wt}$. The elliptical nose was used with vacuum conditions and two attenuators in the beam (A1+A3). For these measurements, the energy window of the detector was reduced and the high energy region of the spectrum was not considered. The irradiations were conducted for at least 3600 s.
Again, a high unknown electronic noise distorted the lower part of the spectrum from 75 keV up to 150 keV and prevented the use of the low energy peaks (see fig. 4.4). Therefore the alternative peak of Eu at 221.30 keV was used also this time.
The ratios between Gd and Eu were obtained using the standard k_0-method. In table 4.4, the

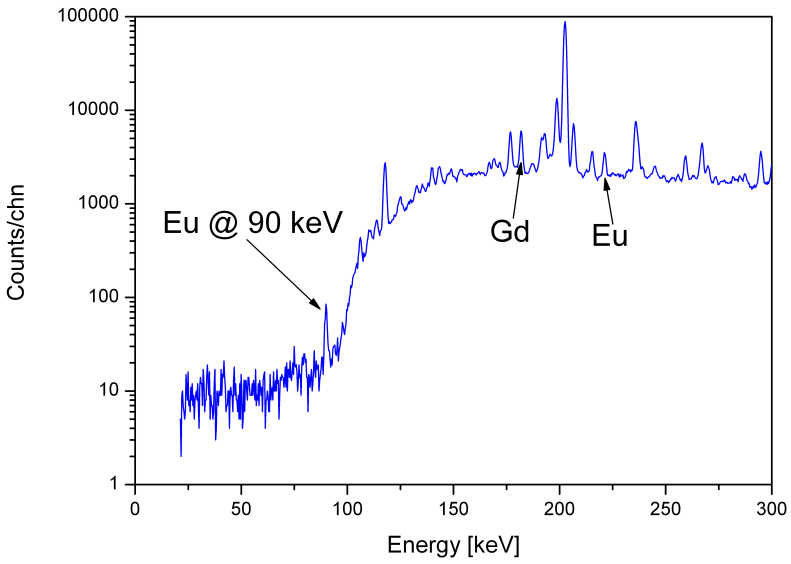

Figure 4.4: *Gamma spectrum for the EuO film with 5 $\%_{wt}$ Gd nominally. It is possible to see the start of the usable spectrum at 150 keV.*

spectrum data and the nuclear data (taken from [36]) used for the calculation are shown.

Energy [keV]	*Efficiency*	k_0
Europium		
221.30(8)	$2.01(4) \cdot 10^{-4}$	1.46(6)
Gadolinium		
181.931(4)	$2.13(4) \cdot 10^{-4}$	139(6)
944.174(10)	$9.20(16) \cdot 10^{-5}$	59.5(13)

Table 4.4: *Data for Eu and Gd.*

ID	Gd/Eu (PGAA)	$\%_{wt}$	Gd/Eu (XAS)	$\%_{wt}$
EuO-5%Gd	2.8(2)		10.6	
EuO-8%Gd	5.7(4)		9.7	
EuO-16%Gd	12.6(10)		19.9	

Table 4.5: *Gd/Eu ratio.*

The Gd/Eu ratios obtained are not in agreement with the nominal ones. Moreover they also disagree with the data obtained by X-ray Absorption Spectroscopy (XAS). A possible reason for this disagreement can be the so-called *summing-coincidence effect*. The counts area of the Eu peak at 221 keV is affected by this effect. This possibility is reasonable because of the complex nuclear structure of Eu and the huge amount of low energy transitions between the nuclear levels. As a cross-check, recalculations were done then with new gamma-rays from the (n,γ)-reaction on ^{153}Eu instead of those from ^{151}Eu. The latter ones were chosen considering the partial production cross section, eventual coincidence with ^{151}Eu and ^{157}Gd and the possible combination for summing-coincidences. In table 4.6 the chosen lines and the respective nuclear data are listed.

Energy [keV]	*Efficiency*	k_0
Europium		
179.83(13)	$2.14(4) \cdot 10^{-4}$	0.40(6)
187.37(8)	$2.12(4) \cdot 10^{-4}$	0.62(3)
281.78(9)	$1.80(3) \cdot 10^{-4}$	0.407(16)
Gadolinium		
181.931(4)	$2.13(4) \cdot 10^{-4}$	139(6)
944.174(10)	$9.20(16) \cdot 10^{-5}$	59.5(13)

Table 4.6: *Improved data for Eu*

The Gd/Eu ratio obtained with this second analysis are in a better agreement with the nominal concentrations. The ratio measured with XAS, however shows some consistent discrepancies also with the nominal values, especially for low Gd concentrations. At higher concentrations, all values are in agreement with each other, see table 4.7.

ID	Gd/Eu $\%_{wt}$ (PGAA)	Gd/Eu $\%_{wt}$ (XAS)	PGAA vs. XAS
EuO-5%Gd	4.33(15)	10.6	-59 %
EuO-8%Gd	8.9(3)	9.7	-8 %
EuO-16%Gd	18.6(10)	19.9	-6.5 %

Table 4.7: *Improved Gd/Eu ratios.*

The results in table 4.7 are obtained as a weighted average of the ratio between all the considered lines for Eu and Gd. The uncertainty on these mass ratios is between 3 and 5 %, these values can be lowered performing, in future measurements with improved electronics, the line with 90 keV of

^{151}Eu, that is free of summing-coincidences and has the highest partial production cross section. PGAA measurements showed to be more precise and trustworthy with respect to the XAS measurements. The latter ones are oscillating, in particular according to the different background correction considered, the values for the same sample can have discrepancies between 3 and 5 %.

4.3 Cd determination in biological tissues

Cadmium, as a contaminant in trace amounts in human tissues, has no essential function. Neonates have usually a negligible amount of Cd in tissues but with age this amount will increase with a rate of about 3 μg per day. Cd is present in food (sea foods, meat, dairy products, and whole grain), drinking water, tobacco, and air. The diet is considered the primary source of Cd intake. The attention on Cd amount in human tissue was caused by genotoxicity tests, epidemiological studies, and long-term animal experiments. The results of all these studies indicate that Cd can be considered a carcinogenic agent in humans [42, 43].

4.3.1 Toxicokinetics of Cd

The intake of Cd has three main routes: inhalation, oral and dermal.
Inhalation of Cd occurs mainly at the workplace. Cd can be inhaled as particulate matter, either as fumes with areosols or as dust. After intake, absorption of Cd depends on particle size and on their solubility. Large particles and dust (particle size >10 μm) usually are deposited in the upper airways, while small particles and fumes (particle size about 0.1 μm) tend to penetrate in the alveoli, which is the major absorption site. 10 - 30 % of the Cd absorption comes from the inhalation of Cd dusts, while absorption for Cd fumes (based on cigarette smoke studies) uptake may vary between 25 and 50 %.
On average an adult takes up Cd, through the oral route, with a rate of 1.4 - 25 μg per day depending on the diet. The Cd absorption through the gastrointestinal tract is about 5 %, however it may raise up to 10 % in subjects that have Fe deficiencies.
Absorption through the dermal route is very low (about 0.5 %), and it has a considerable impact only in case of a prolongated contact with highly concentrated solutions.
Cadmium is widely distributed in the human body; it is estimated that from the total intake of Cd 50 % are accumulated in the kidney, about 15 % in the liver and about 20 % in muscles. However, kidney and liver remain the major target organs. Accumulation in kidney and liver increases until 40-65 years of age. After that period it reaches saturation that is bound to the biological half-life. The biological half-life of Cd is comparably long; for the kidney it may vary between 6 and 38 years and for the liver between 4 and 19 years. In muscles, the accumulation of Cd is a life-long process.
After the uptake in the lungs and in the gastrointestinal tract, Cd is transported in the blood and plasma bound to albumin, which is then preferentially taken up by the liver. In the liver, Cd induces the synthesis of metallothionein that after few days reappears inside the blood plasma. Due to its lower molecular weight, this compound is filtered in the kidney through the glomeruli and then is taken up by the tubules (located in the kidney cortex) where they accumulate.
The major amount of Cd introduced orally or through inhalation is excreted with feces and represents the Cd that was not absorbed. The absorbed amount is cleared very slowly with urine and feces. It is also cleared through hair and breast milk, but these two routes are of minor importance [42, 44].

4.3.2 Determination of Cd in human tissues

The goal of this project was to establish a method for the determination of Cd in human tissues. Cd has a very large cross section for neutron capture and therefore PGAA is a convenient method for such measurements. The velocity of the measurements and the rather easy preparation of the samples allows a more systematical study on Cd in human tissues.
As Cd is suspected as potential cancer agent, the interest of oncologists in the study of the metabolism of Cd in tissues is high. For example, a possible application could be the study of the influence of Cd in ovarian cancer. Different studies demonstrate that Cd has potential estrogenic activity. That means that it can activate the estrogen receptors which control the growth of cells and may be a probable cause of ovarian cancer [45, 46].

First measurements - September 2009

In September 2009, first test measurements were carried out in collaboration with the *Institut für Rechtsmedizin* of the Ludwig-Maximilians-Universität (LMU, München). The first set of measurements were carried out in order to check if it was possible to detect traces of Cd inside biological samples. The samples were prepared at the Institut für Rechtsmedizin. Slices of kidney, liver, cerebrum, cerebellum, and mammal tissues were sealed in standard polyethylene (PE) bags and inserted in the neutron beam. Because of the high count-rate from the H peak, the test measurements were taken for 1200 s with the lowest beam intensity available and with air inside the chamber. For this measurements, the energy range of the gamma-ray detector was reduced (from 80 keV up to 3 MeV). The most intense peak of Cd has a relatively low energy (558.32 keV), thus the high energy part of the spectrum was not necessary for this purpose.
The first problem encountered was the extremely high spectral background of water. However, Cd was clearly detected in the kidney sample and it was possible to see a small peak in the spectrum for the liver sample. For all the other tissues it was not possible to detect any Cd peaks.
According to literature data, the average amount of Cd in the kidney cortex is highly dependent on the age and on the geographical provenience as shown in fig. 4.5. The kidney concentration of an non-smoker adult is around 14.8 μg/g, while in liver it is 1.38 μg/g [43]. From these latter data it was possible to estimate the detection limit for Cd in biological tissues (native tissues) which is about 1 μg/g.

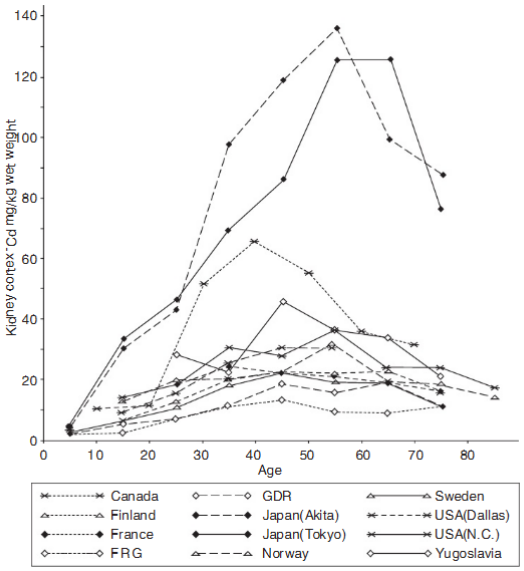

Figure 4.5: *Average Cd concentrations in the kidney cortex in relation to age. Results from 1970s and 1980s in ten countries are summarized from 12 different studies. The averages are based on smokers, non-smokers, males and females combined. For some studies kidney cortex concentrations in wet weight have been calculated from ash or dry weight or from whole kidney values [44]*

In order to reduce the signal of H and increase thus the Cd detection limit, two different methods for sample preparation were tested: drying and preconcentration. Both processes were tested on liver samples. Slices of liver were then put inside a small chamber, which was subsequently evacuated with a vacuum pump. This way, the water was removed from the sample. The advantage of this method is that the amount of the other elements inside the sample like Na, Cl, and S remain unchanged.
Preconcentration of the samples was obtained by dissolving the tissues in concentrated HNO_3 and then evaporating them. The residues were then sealed inside FEP-bags and measured. With this procedure, a larger amount of liver can be measured and the sample is also homogenized. The handling of the sample during this first trial was not perfect; some steps have to be improved, for example the packing of the samples with a proper material. Concerning the preparation procedure, short times for the drying did not allow a complete elimination of water. Also in this case the measurements were rather short (again 1200 s) under normal air conditions.
Nevertheless, encouraging results were obtained. The H contents were reduced up to a factor of 5 with the preconcentration of the sample, reducing the hydrogen Compton background. In fig. 4.6 the spectra obtained for kidney and liver slices without any treatment and the treated liver samples are shown.
The preparation techniques used require a suitable method to quantify Cd in the measurements. As already discussed, PGAA as an absolute method is not the preferable method for quantitative analysis, comparative methods are preferable. The problem in this case was that it was not possible to find an universal comparator for all the sample preparation procedures. The most used elements H and Cl were not usable: H cannot be used as the aim is to drastically reduce it and Cl amount is affected when the sample is preconcentrated. An possible comparator candidate could be K that qualitatively seems to remain constant with all sample treatments. Another

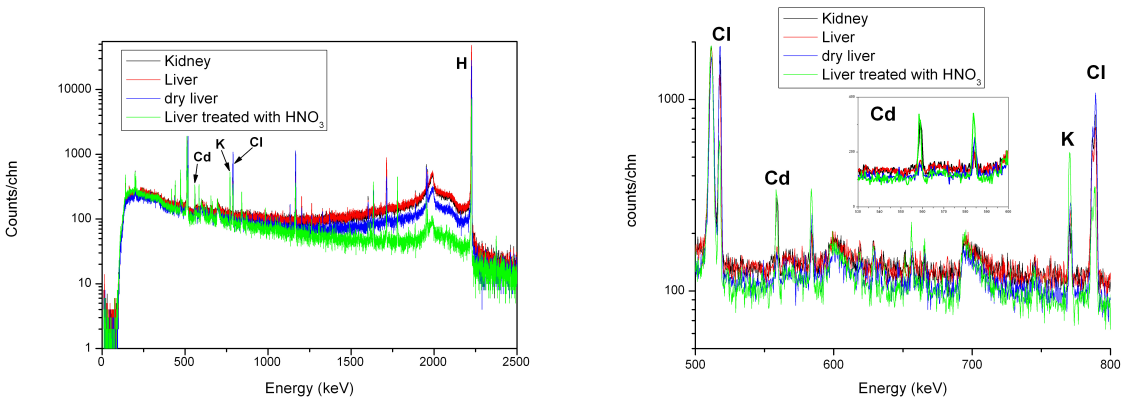

(a) Cd full spectra

(b) Detail in the Cd energy region

Figure 4.6: *Cd gamma spectra*

possible solution would be a calibration curve for Cd.

Measurements - February 2010

To find a proper method for the quantification of Cd inside biological tissues, a more systematic set of measurements was carried out in February 2010. A calibration curve was first measured. For these measurements, different samples with different concentrations were prepared, see table 4.8. The diluted solutions were prepared starting from a 0.999 mg/g standard solution and then diluted. Between 75-150 μl, according to the concentration, were pipetted on filter paper and then measured.

Concentration [ppm]	*Sample [μl]*	*cps*
100	75	7.92(13)
50	75	4.02(8)
30	75	1.93(8)
15	100	1.26(5)
10	100	1.06(7)
5	150	0.63(5)
1	150	0.17(11)
0.5	150	0.11(9)
0.1	150	–

Table 4.8: *Cd sample used for the determination of the calibration curve.*

In fig. 4.7 the calibration curve that was obtained with the linear regression is shown.

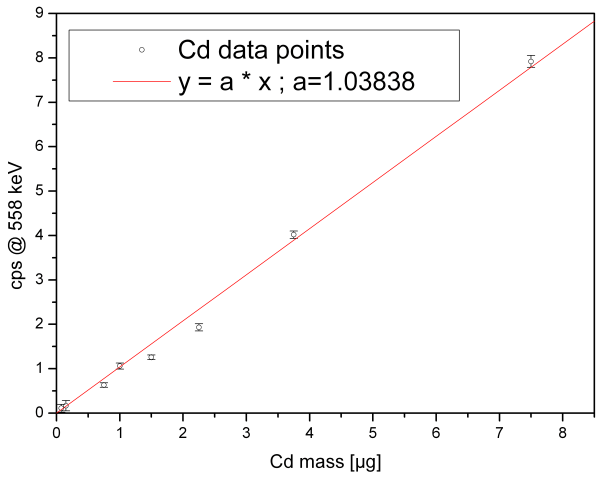

Figure 4.7: *Cadmium calibration curve.*

As described in chapter 2, the slope of the linear regression yields the analytical sensitivity for Cd: 1038.38 cps/mg.
For the measurements a kidney sample (Ki) was taken as check-samples. This sample comes from a 55 y smoker male (patient ID 1-55mS [2]). The amount of Cd in smoker subjects is higher than in non-smoker subjects, therefore it was chosen for the quality-check of the method. Three samples were prepared: one natural sample (packed in FEP-foil) - wet weight 0.934 g, one dried sample - wet weight 0.630 g and one preconcentrated sample - wet weight 0.991 g. The last sample was obtained dissolving the sample in 2 ml 65 % HNO_3.
Native tissue before the irradiation were stored in a freezer at -30 °C, this storage is needed because of the fast deterioration of the sample at room temperature. For the freezed native tissue the measurements were performed in normal air with a low neutron beam intensity (all the attenuators in the beam) and short irradiation times (1200 s). For the dried sample and the preconcentrated one the flux was increased (only A2 and A3 in the beam, for a flux of $1.92 \cdot 10^9\,\mathrm{cm^{-2}s^{-1}}$ and it was also possible to use vacuum conditions. The measuring time was chosen around 3600 s in order to have a reasonable peak statistics for the Cd peak between 0.1 - 3 %. The different irradiation conditions were then considered in the calculations. An appropriate correction factor for the different beam intensities was used. In table 4.9 the results of these measurements are reported.

ID	*mass [g]*	*cps*	*Cd mass [µg]*	*Cd conc. [µg/g]*
1-55mS-Ki-HNO_3	0.991	34.5(1)	13.6(2)	13.7(2)
1-55mS-Ki-dry	0.630	20.5(2)	8.1(2)	12.8(6)
1-55mS-Ki-native	0.934	8.8(1)	8.5(2)	9.1(2)

Table 4.9: *Cd concentration in kidney samples of patient 1-55mS.*

[2] Due to the data privacy protection, no information about the patience except age, sex and eventual information on the smoking history were provided. The ID of the samples were constructed as follows: patient number-age sex smoking history(S=smoking, NS=non smoking)-tissue-preparation procedure, for example 1-55mS-Li-HNO_3, for missing data a X was used.

The Cd concentration in the last column was calculated for the wet weight of the sample and the average Cd concentration obtained from the data is 11.58(14) μg/g.
Beside the kidney check-samples, three different kinds of tissues from another patient (ID 2-XXmNS) were also acquired and measured. In particular, these tissues were kidney (Ki), liver (Li) and prostate (Pr). This set of samples was used to cross-check the method already developed. For every tissue, three samples were prepared as previously described. In table 4.10 the results are summarized.

ID	*mass [g]*	*cps*	*Cd mass [μg]*	*Cd conc. [μg/g]*
2-XXmNS-Ki-HNO_3	0.992	4.92(6)	1.93(4)	1.95(4)
2-XXmNS-Ki-dry	0.547	1.27(4)	1.22(5)	2.24(8)
2-XXmNS-Ki-native	0.591	1.29(3)	1.2(9)	2.1(3)
2-XXmNS-Li-HNO_3	1.047	0.86(1)	0.339(3)	0.323(3)
2-XXmNS-Li-dry	0.401	0.112(8)	0.108(8)	0.27(2)
2-XXmNS-Li-native	0.764	0.153(9)	0.15(7)	0.19(3)
2-XXmNS-Pr-HNO_3	1.000	n. d.	–	–
2-XXmNS-Pr-dry	0.614	–	–	–
2-XXmNS-Pr-native	0.803	–	–	–

Table 4.10: *Cd concentration in kidney, liver and prostate samples of patient 2-XXmNS. n.d.= not determined.*

The Cd concentrations obtained for patient 2-XXmNS are relatively low. For example in the kidney, the average concentration obtained is 2.01(4) μg/g, nearly 6 times lower than the Cd concentration for the smoker kidney (see fig. 4.8). This may be an indication that patient 2-XXmNS was not a smoker. For liver, the amount of Cd is definitely lower with respect to kidney. In prostate tissues, no trace of Cd could be detected.

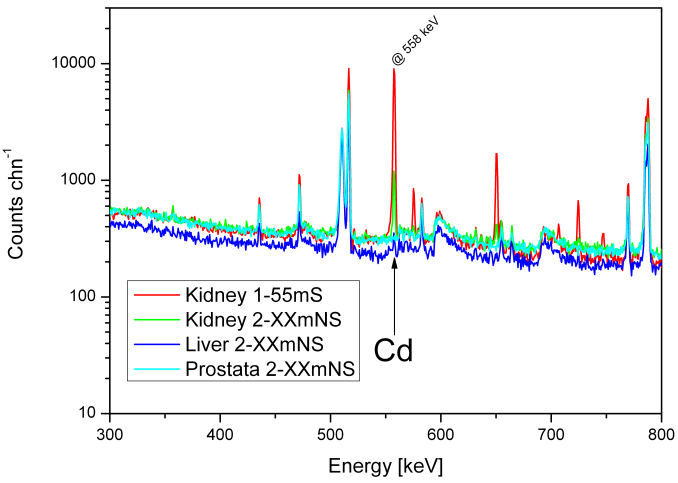

Figure 4.8: *Comparison of the gamma spectra between the tissues for patient 1-55mS and 2-XXmNS.*

Measurements - May 2010

In May 2010, a last set of measurements was carried out. This time, the samples were coming from 2 patients and the analysed tissues were kidney, liver, lung (Lu) and heart (He). Lung tissues were chosen because lungs are the main route of Cd intake through inhalation, and heart tissues because heart is a muscle and as previously discussed, about 20 % of Cd is distributed in muscles.
For this set of measurements, samples were collected from two patients, 3-71mXX and 4-87fXX. Both were relatively old (71 y and 87 y) and no record about their smoking history could be given. Moreover, for the first patient, two sets of the same tissues were collected. The measuring conditions were the same as those used in the former irradiations. In table 4.11, the results for this set of measurement for patient 3-71mXX and in table 4.12 for patient 4-87fXX are shown.

ID	mass [g]	cps	Cd mass [μg]	Cd conc. [μg/g]
3-71mXX-Ki1-HNO_3	0.9572	10.11(8)	4.99(10)	5.21(10)
3-71mXX-Ki1-dry	0.6709	7.79(4)	2.44(1)	3.64(2)
3-71mXX-Ki1-native	0.8151	2.71(5)	1.06(16)	1.31(20)
3-71mXX-Ki2-HNO_3	1.1607	5.48(5)	2.70(5)	2.33(4)
3-71mXX-Ki2-dry	0.7407	2.23(4)	1.71(4)	2.31(6)
3-71mXX-Ki2-native	0.5553	1.00(5)	0.31(5)	0.57(9)
3-71mXX-Li1-HNO_3	0.9334	2.52(2)	1.24(2)	1.33(3)
3-71mXX-Li1-dry	0.9253	1.65(4)	0.52(2)	0.56(2)
3-71mXX-Li1-native	0.7833	0.92(4)	0.36(6)	0.46(7)
3-71mXX-Li2-HNO_3	1.1607	n.d.	–	–
3-71mXX-Li2-dry	0.6462	0.418(9)	0.131(4)	0.202(6)
3-71mXX-Li2-native	0.4510	–	–	–
3-71mXX-He1-HNO_3	1.000	0.220(5)	0.108(3)	0.118(3)
3-71mXX-He1-dry	1.2784	0.176(6)	0.055(2)	0.043(2)
3-71mXX-He1-native	0.7054	0.94(2)	0.37(6)	0.53(8)
3-71mXX-He2-HNO_3	0.9964	0.095(4)	0.047(2)	0.047(2)
3-71mXX-He2-dry	0.6355	–	–	–
3-71mXX-He2-native	0.3727	–	–	–
3-71mXX-Lu1-HNO_3	1.0699	0.337(6)	0.166(4)	0.155(4)
3-71mXX-Lu1-dry	1.9930	0.234(7)	0.073(2)	0.037(1)
3-71mXX-Lu1-native	0.5833	–	–	–
3-71mXX-Lu2-HNO_3	0.9644	n.d.	–	–
3-71mXX-Lu2-dry	0.8971	–	–	–
3-71mXX-Lu2-native	0.6812	–	–	–

Table 4.11: *Cd concentration in kidney, liver, heart, and lung samples of patient 3-71mXX. n.d.= not determined.*

ID	mass [g]	cps	Cd mass [μg]	Cd conc. [μg/g]
4-87fXX-Ki-HNO_3	1.2956	30.06(8)	14.8(3)	11.5(2)
4-87fXX-Ki-dry	1.1730	33.66(15)	10.5(2)	9.0(2)
4-87fXX-Ki-native	0.5120	12.05(8)	3.8(6)	7.4(11)
4-87fXX-Li-HNO_3	1.1467	3.36(2)	1.66(3)	1.45(3)
4-87fXX-Li-dry	0.9117	3.33(4)	1.04(2)	1.15(2)
4-87fXX-Li-native	0.4296	1.22(3)	0.38(6)	0.89(14)
4-87fXX-He-HNO_3	0.9792	0.034(2)	0.017(1)	0.017(1)
4-87fXX-He-dry	1.0763	–	–	–
4-87fXX-He-native	0.4694	–	–	–
4-87fXX-Lu-HNO_3	1.4323	0.395(8)	0.195(5)	0.136(4)
4-87fXX-Lu-dry	0.9565	0.316(8)	0.100(3)	0.103(3)
4-87fXX-Lu-native	0.6594	–	–	–

Table 4.12: *Cd concentration in kidney, liver, heart, and lung samples of patient 4-87fXX.*

The concentrations of Cd in the dried and preconcentrated sample are near to each other, while for the native tissues there are some noticeable discrepancies. As an example, lets consider the results of the native samples for kidney from patient 3-71mXX. The values obtained for the native tissue, kidney 1, have a discrepancy of about 20 % with respect to the other results, and the same occurs for the second set for kidney. A possible explanation, of these huge discrepancies, is the thermalisation of neutrons inside water-rich samples (a detailed description of this process can be found in the next section) combined with the non-matching of the matrix used for the calibration.
Differences in the results for the same tissue can be due to inhomogeneities in the Cd distribution inside the tissue. For example, in the kidney, Cd accumulates selectively in the cortex and not in the medulla. In heart samples, the differences in the results can be due either by concentrations close to the detection limit or by an inhomogeneous distribution within the organ.
The treatment of the samples in order to diminish the amount of water was successful and it lowered the detection limit to about 0.05 ppm.

4.3.3 Biological samples and neutrons

Water is known to be a very effective thermalising material for neutrons. Biological samples contain mainly water. In the case of our PGAA facility, the neutrons used for the irradiation are cold neutrons, and a possible secondary process that can occur in measurements involving *water-rich samples* is the moderation of neutrons. In this particular case, the neutrons are accelerated up to the thermal energy of the sample (25 meV).
In order to verify if this secondary process influences the measurement, a simulation of a cold neutron beam through a 1 mm thick water slice was performed. For simplicity, the neutron spectrum considered was a Maxwellian spectrum with an average energy equal to the average energy of the PGAA neutron spectrum. The simulation was performed with the Monte Carlo software MCNP [47]. The simulation was carried out for two different descriptions of the water layer. The result obtained are shown in fig. 4.9.

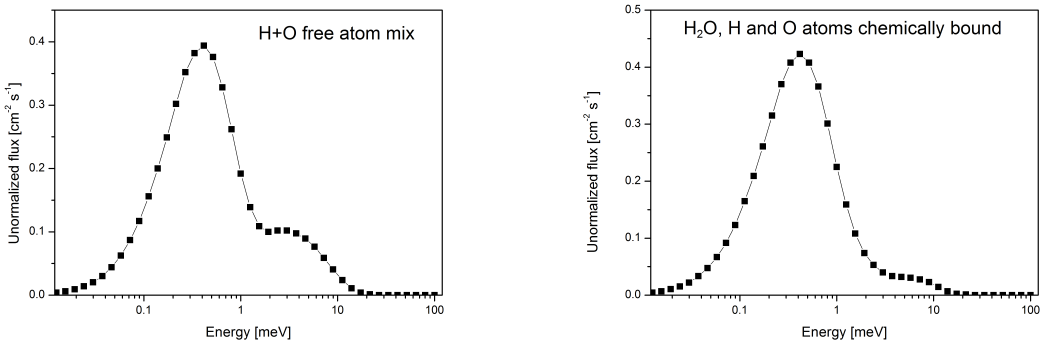

(a) $2\,H^+O$ free atom mixture (b) H_2O

Figure 4.9: *Neutron spectrum simulation.*

From the simulations it is possible to see that a small part of the neutron spectra is shifted to higher energies. Through the fit of the resulting neutron spectrum follows that about 7.1 % of the neutrons are accelerated to thermal energies. Probably due to this process, in combination also with the mismatching of the matrix of the first calibration curve, the Cd concentration for the native samples deviate from the values obtained from the treated samples, where the amount of water was drastically reduced.
The main discrepancies were found for the sample, 3-71mXX-Ki1-native, 3-71mXX-Ki2-native, and 3-71mXX-Li1-native. A rough calibration curve for water-containing samples was obtained from the samples used for the Cd k_0-values (see tab. 4.2). The analytic sensitivity obtained from the linear regression of the two samples is 269 cps/mg. The concentration for these tissues were calculated from this value. In table 4.13 the new concentrations are listed.

ID	mass [g]	cps	Cd mass [μg]	Cd conc. [μg/g]
3-71mXX-Ki1-HNO_3	0.9572	10.11(8)	4.99(10)	5.21(10)
3-71mXX-Ki1-dry	0.6709	7.79(4)	2.44(1)	3.64(2)
3-71mXX-Ki1-native	0.8151	2.71(5)	4.1(6)	5.0(8)
3-71mXX-Ki2-HNO_3	1.1607	5.48(5)	2.70(5)	2.33(4)
3-71mXX-Ki2-dry	0.7407	2.23(4)	1.71(4)	2.31(6)
3-71mXX-Ki2-native	0.5553	1.00(5)	1.2(2)	2.2(4)
3-71mXX-Li1-HNO_3	0.9334	2.52(2)	1.24(2)	1.33(3)
3-71mXX-Li1-dry	0.9253	1.65(4)	0.52(2)	0.56(2)
3-71mXX-Li1-native	0.7833	0.92(4)	1.4(2)	1.7(3)

Table 4.13: *New Cd concentration in the native samples for kidney and liver of patient 3-71mXX compared with the one obtained for the treated samples.*

The new concentrations for the native samples are in much better agreement with the ones obtained for the dried and preconcentrated samples. Another outcome from these calculation is that the water calibration does not work for all the native samples. This can be explained with the fact that the other samples were still frozen (H atoms are bound to a crystal structure) at

the moment of the measurement while these one were only partially frozen or already at room temperature.
With this experiment, it was shown that Cd can be detected successfully in human tissue. For the quantitative analysis of the spectra, a calibration curve is preferred to the k_0-method because of the difficulty to find a comparator element. Moreover, the detection limit can be lowered by drastically reducing the amount of water in the tissues. In this direction two techniques were studied: dehydration and preconcentration. The results obtained with the two methods are comparable, nevertheless some remarks have to be made. With the dehydration procedure, the overall elemental composition (except water of the tissue remains unchanged and it is possible to treat quite easily multiple samples at once. The preconcentration method allows a very precise Cd measurement; the samples are homogenized and it is possible to analyse much more material. The disadvantages of this treatment are the long sample preparation times and a higher risk of contamination due to the extensive handling of the samples.

4.4 PGAA and archeology

The main focus of archeology is to reconstruct events of the past starting from the remains of objects and artifacts. The use of classical archeology based on form, style, decoration and of the objects is not anymore sufficient to give a complete description or reconstruction of the events. Therefore, there is an increasing need to complete these analysis also with scientific analytical methods. Actually, the various analytical techniques available help in the determination of the age of the object (dating), in the definition of the technology, the provenience and in the reconstruction.
The danger in such an analysis, however, is the damage to the object itself. In a wider sense every analysis is destructive. The choice of one scientific method compared to an another is a complicated task for archaeologists and depends on the balance between costs and the amount of information that can be obtained.
The most widely used methods for archaeological samples are instrumental neutron activation analysis (INAA), inductively coupled plasma-mass spectrometry (ICP-MS), proton induced X-ray emission spectroscopy (PIXE). PGAA has some advantages compared to these methods. First of all, with PGAA it is possible to determine light elements. In most mineral-based artifacts the major components are alumina and silica and they are not precisely determined with INAA. Boron is an element that cannot be measured by INAA. Its detection is possible with ICP-MS but the uncertainties are significant compared with the uncertainties obtained through a PGAA measurement, that is particularly sensitive to this element. With PIXE only elements with atomic numbers Z between 20 and 90 can be detected with high sensitivity and due to the low penetration of protons only surface information can be achieved. Moreover, in order to perform INAA and ICP-MS measurements it is necessary to remove few μg to mg (or more) from the object. PGAA, in contrast, it is a non-destructive technique from a macroscopic point of view. The objects are not visibly damaged after a PGAA measurement. A PGAA measurement yields information on the bulk composition of the object, the objects do not need special preparation and the whole information can be delivered in a quite short time compared to other techniques [48].

4.4.1 Bronze coins

Between March and December 2007, a big excavation took place in the area of Lithochori of Kavala's prefecture in Greece. The area investigated with this excavation was around 3500 m^2. The antiquities found were partly damaged by the intensive cultivation in the area and the illegal excavations.
According to archaeologists, the site is strongly bound to an ancient settlement located in the north-west. In the area a building, a cemetery with several burial and cremation burials were found. The most important findings were a collection of clays, jewels, bronze and silver coins, a bronze vessel in the shape of Dionysus and an iron seat ornamented with a lion's heads [49, 50].
A small collection of coins found in this area was analysed with the PGAA method. The coins selected, fig. 4.10 and fig. 4.11, are described according to the archaeological classification in table 4.14 [51].

ID	Description
Coin 1	Coin of the city of Philippi, dated to the age of Augustus or Tiberius (27 BC-37 AD). Head of the emperor / Scene of ploughing. Diameter 16 mm, weight 3.393 g, material: bronze. **Mint: City of Philippi, local circulation.**
Coin 2	Coin of the city of Philippi, dated to the age of Augustus or Tiberius (27 BC-37 AD). Head of the emperor / Scene of ploughing. Diameter 18 mm, weight 3.966 g, material: bronze. **Mint: City of Philippi, local circulation.**
Coin 3	Coin of the city of Philippi (1^{st} - 2^{nd} century AD). Nike / three military standars. Diameter 20 mm, weight 4.278 g, material: bronze. **Mint: City of Philippi, local circulation.**
Coin 4	Coin of the city of Philippi (1^{st} - 2^{nd} century AD). Nike / three military standars. Diameter 18 mm, weight 4.301 g, material: bronze. **Mint: City of Philippi, local circulation.**
Coin 5	Coin of the city of Philippi dated to the age of Antonius Pius (138-161 AD). Bust of Antonius / Antonius (?) crowning Augustus. Diameter 23 mm, weight 6.937 g, material: bronze. **Mint: City of Philippi, local circulation.**
Coin 6	Sestertius of Antonius Pius (138-161 AD). Bust of Antonius / Quadriga (chariot drawn with four horses). Diameter 31 mm, weight 26.025 g, material: bronze. **Mint: City of Rome, circulation in the entire Roman Empire.**
Coin 7	Coin of the city of Topirus dated to the age of Antonius Pius (138-161 AD). Bust of Antonius / Enthroned Zeus. Diameter 25 mm, weight 7.826 g, material: bronze. **Mint: City of Topirus, local circulation**
Coin 8	Coin of the KONION of Macedonians dated to the age of Antonius Pius (138-161 AD). Bust of Antonius / Winged thunderbolt. Diameter 26 mm, weight 10.673 g, material: bronze. **Mint: uncertain city, local circulation**

Table 4.14: *Classification of the bronze coins founded in the archaeological excavation site.*

On these coins, different non-destructive analysis were carried out. The main goal was to determine the metallurgical composition of the coins that can help the archaeologists to determine the provenience of the coins. Other methods like X-Ray Diffraction (XRD) and Scanning Electron Microscope Energy Dispersive X-ray (SEM-EDX) were already used to analyse these coins. The results from these methods however can determine only the metallurgical composition of the surface. With PGAA, it is possible to obtain the bulk composition of the coins [52].
Cu as the major component of the copper-alloys has a relatively high cross section (3.795 b) compared to the other elements that contribute to the alloy, mainly Zn (1.30 b) and Sn (0.54 b). Moreover, the total number of gamma rays is around 600 and is distributed over the entire energy range. Therefore, the determination of trace elements or minor components is not always successful in these alloys. In addition, Cu is activated noticeably also in short measurements,

(a) Coins *heads*

(b) Coins *tails*

Figure 4.10: *Coins 1, 2, 3 and 4 analysed with PGAA.*

(a) Coins *tails*

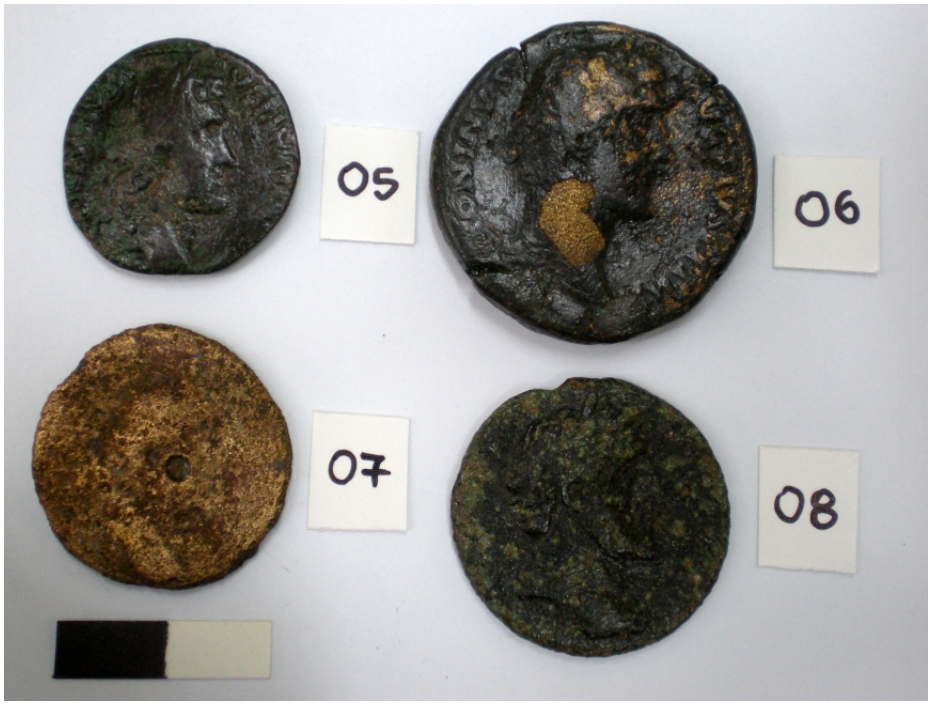

(b) Coins *heads*

Figure 4.11: *Coins 5, 6, 7 and 8 analysed with PGAA.*

because one of the daughter nuclei resulting from the (n,γ)-reaction is a relatively short lived radionuclide, ^{64}Cu, with an half-life of 12.7 h. The coins were measured with a low (all attenuators in beam) and collimated neutron beam. This was necessary primarily to reduce the count-rate produced by Cu, and secondly to reduce the activation of the coins. Vacuum conditions were used and the duration of the measurements were between 3600-7200 s. In table 4.15 the results for the bronze coins are listed.

ID	*Cu* $\%_{wt}$	*Zn* $\%_{wt}$	*Sn* $\%_{wt}$	*Pb* $\%_{wt}$	*Cl* $\%_{wt}$	*Ni* $\%_{wt}$
PGAA						
Coin 1	84.0(19)	2.45(7)	1.14(32)	2.06(9)	0.067(7)	–
Coin 2	83.6(19)	2.34(6)	13.3(4)	0.75(4)	–	–
Coin 3	94.5(22)	2.61(7)	2.75(11)	–	0.218(3)	–
Coin 4	94.0(21)	2.63(7)	3.28(12)	–	–	0.55(6)
Coin 5	94.4(21)	2.43(6)	3.14(11)	–	–	0.025(3)
Coin 6	84.7(19)	12.4(7)	2.91(7)	–	–	–
Coin 7	85.6(19)	2.25(6)	8.95(25)	3.06(10)	0.143(5)	0.036(5)
Coin 8	83.0(19)	2.38(6)	11.5(3)	2.98(10)	0.122(2)	–
SEM-EDX						
Coin 1	75.5	–	16.4	7.1	–	–
Coin 2	68.3	0.23	29.8	0.92	0.1	–
Coin 3	89.5	–	–	–	–	–
Coin 4	80.6	–	5.6	6.7	0.66	–
Coin 5	82.2	–	1.93	0.32	–	–
Coin 6	–	–	–	–	–	–
Coin 7	73.6	–	13.09	12.63	–	–
Coin 8	31.2	–	14.4	40.4	0.18	–

Table 4.15: *Elemental composition of the bronze coins (all the values are in weight percent).*

Non-destructive PGAA measurements on the coins revealed the bulk composition of the objects. In some cases it was also possible to find trace elements like Ni, that were not determined with SEM-EDX analysis. The main composition of the copper alloy may help the archaeologists in the determination of the geographical provenance of the coins as well as in the determination of possible remelting procedure of older coins. The metallurgical composition is also helpful for a correct dating of the coins.
The Cl traces result from surface contamination of the coins. Cl is a dangerous element for copper alloys, because it can induce the so-called *bronze disease* and it should be removed completely in the restoration phase. Copper reacts with Cl, forming CuCl and $CuCl_2$, where the first one is responsible for damages. Copper is corroded electrochemically. The first step in the electrochemical corrosion of copper and copper alloys is the production of cuprous ions. These combine with the chloride to CuCl, which is highly unstable. Exposed to air, CuCl hydrolizes with the moisture of oxygen and water to form HCl and $CuCl_2$:

$$4\,\mathrm{CuCl} + 4\,\mathrm{H_2O} + \mathrm{O_2} \longrightarrow \mathrm{CuCl_2} \cdot 3Cu(OH)2 + 2\,\mathrm{HCl}. \tag{4.5}$$

The acid produced in turn attacks the bronze and produces through corrosion more CuCl:

$$2\,\mathrm{Cu} + 2\,\mathrm{HCl} \longrightarrow 2\,\mathrm{CuCl} + \mathrm{H_2}. \tag{4.6}$$

This *chain reaction* will continue until all material is corroded or the chlorides are eliminated or converted to harmless Cu_2O .

CHAPTER 5

Instrumentation 2: 2D PGAA

The high flux of the PGAA facility makes it possible to carry out two dimensional mapping measurements of elements inside relatively large samples.
First test measurements for this new measurement mode were carried out with a setup newly developed for the European project ANCIENT CHARM. In a second step, a more dedicated setup, that was already used at PSI, was rebuilt and optimised.
In this chapter the, *Ancient Charm* setup is described only briefly. More room is given to the 2D dedicated setup.

5.1 ANCIENT CHARM setup

5.1.1 The ANCIENT CHARM project

Neutron-based analytical methods have the power to provide average elemental (or isotopic) compositions of a bulky samples. In recent years the interest in neutron-methods increased, especially for the analysis of archaeological samples mainly thanks to the non-destructiveness of the method.
Ancient Charm was a project funded by the European Community "New and Emerging Science and Technology" programme. The name *Ancient Charm* is an acronym for *Analysis by Neutron resonant Capture Imaging and other Emerging Neutron Techniques: new Cultural Heritage and Archaeological Research Methods*. The main aim of this project was to develop a powerful neutron-based imaging method for a non-invasive 3D investigation of cultural heritage objects. The final goal was to provide 3D information about the elemental and phase compositions of the samples [53].
The new imaging methods involved in this project were:

- Neutron Resonant Capture Imaging combined with Neutron Resonance Transmission (NRCI/NRT);
- Prompt Gamma Activation Imaging combined with cold Neutron Tomography (PGAI/NT);
- Neutron Diffraction Tomography (NDT).

The PGAA facility at FRM II was involved in this project, due to the high neutron flux available.

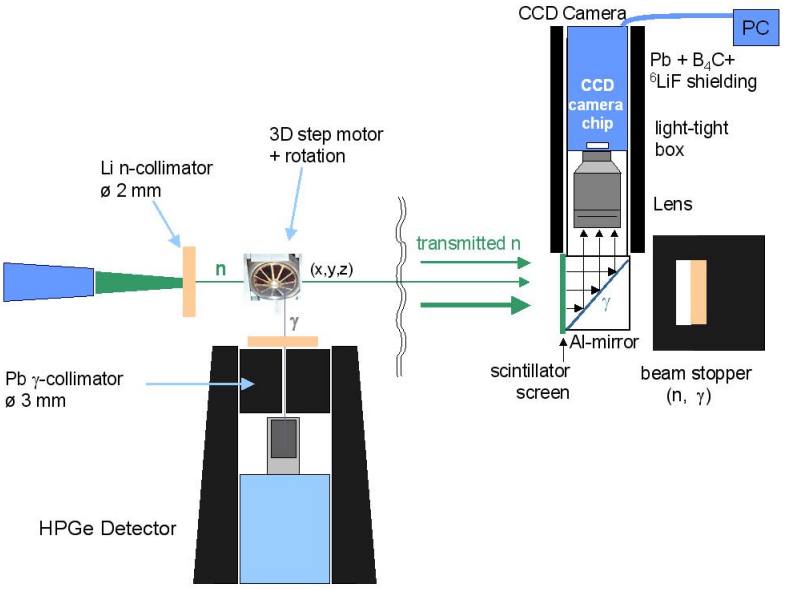

Figure 5.1: *Sample position for the PGAI-NT setup.*

5.1.2 Setup for PGAI - Prompt Gamma Activation Imaging

For PGAI/NT measurements the configuration of the PGAA setup was modified. The γ-collimator of the coaxial detector (60 % rel. efficiency, see fig. 3.6) was exchanged by a lead collimator with significantly smaller aperture (about 3 mm). The perpendicular detector (35 % rel. efficiency, see fig. 3.6) was not used.
The Al sample chamber in fig. 3.5 was completely removed to make space for a (x, y, z, ω)-positioning table. A CCD tomograph was placed behind the sample position for Neutron Radiography and Tomography (NR and NT).
A neutron flight tube was built for the NR and NT measurements. It is 160 cm long and lined with B rubber. The introduction of the flight tube was necessary in order to obtain a more parallel and homogeneous neutron beam at the sample position. Moreover, to improve the beam quality, two B-collimators were placed along the flight tube to cut the most divergent neutrons. An adjustable neutron collimator, with 2 mm diameter, was then placed near the sample position for PGAI measurements [54].
All the changes applied to the sample position *place* are shown in fig. 5.1.
The elliptical nose was not used for these measurements because of the very high divergence of the neutron beam. A divergent beam would not allow to describe precisely the *isovolume* irradiated, i.e. the volume of the sample illuminated by the intersection of the collimated neutron beam and the collimated γ-detector. A detailed description of the PGAI-NT setup and settings can be found in [54]. For 2D measurements, this setup was used first. In this case, the perpendicular detector was used because of the larger γ-collimator (1 cm in diameter), and only two stages of the (x, y, z, ω)-positioning table were used. The adjustable neutron collimator together with the neutron radiography system was used for the positioning of the sample and for the programming of the scanning grid.
With this setup a piece of the Allende meteorite was scanned. The results of these measurements can be found in chapter 6.

5.2 2D motor

A second setup, just for two dimensional measurements, was then built and tested. The setup is originally coming from PSI and it was already used for position sensitive PGAA [55]. In the first measurements at PSI, the neutrons were focused through a neutron lens and the dimension of the neutron spot was about 1 mm in diameter.
The two stage table used in this setup was also suitable for vacuum conditions that were not available with the PGAI-NT setup.
Only few changes had to be made to the PGAA instrument compared to the PGAI-NT setup. The only element that had to be removed is the six position sample changer, as in this case the sample chamber becomes more compact. The shielding materials around the sample chamber remained unchanged.

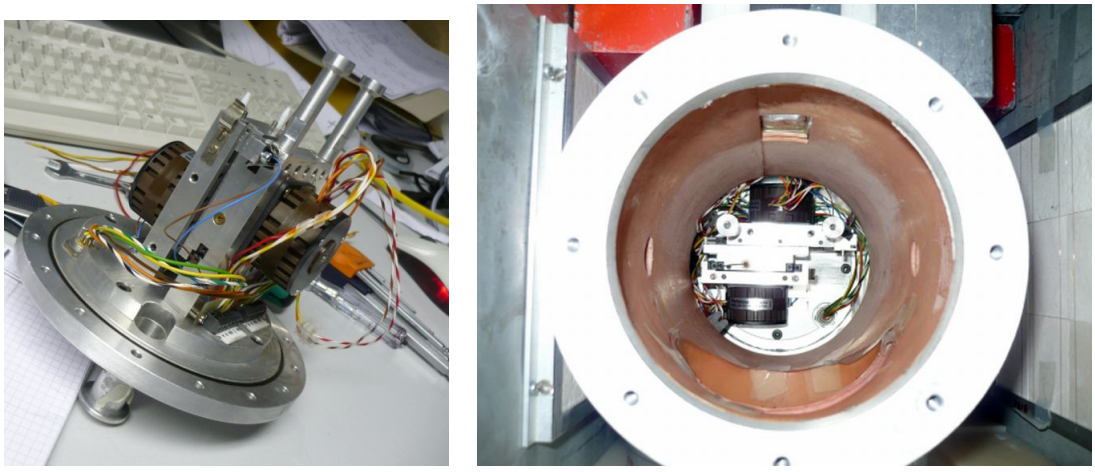

(a) Two stage motor

(b) Motor mounted on the sample chamber

(c) Vacuum valve

Figure 5.2: *Two stage table mounted at the PGAA instrument.*

The elliptical tapering of the neutron guide helped in focusing the neutrons on the sample, but the neutron field dimensions have to be reduced. Also in this case the elliptical nose was not used because of its high beam divergence. On the one hand to avoid a too large magnification of the

neutron field dimension due to the divergent neutrons, the neutron collimator should be placed as near as possible to the focus, i.e. near the sample. On the other hand, a close n-collimator increases significantly the background. Two options for the collimator material were available:

- a larger B_4C collimator + a LiF-polymer collimator or
- a LiF-ceramic collimator + a LiF-polymer collimator.

Both of these combinations have disadvantages. The boron carbide plus the LiF ceramic can produced a high prompt gamma radiation background due to the 477 keV B line. In contrast, the LiF-polymer collimator has no prompt gamma radiation but it produces a huge amount of fast neutrons (secondary reaction on Li) that can damage the germanium detector. Both solution were tested (fig. 5.3). Finally the LiF-polymer was chosen as neutron collimator, because the signal of the B_4C was too high and it did not allow to detect the lower energy part of the gamma spectrum. The aperture chosen was $2 \times 2\,\mathrm{mm}^2$.

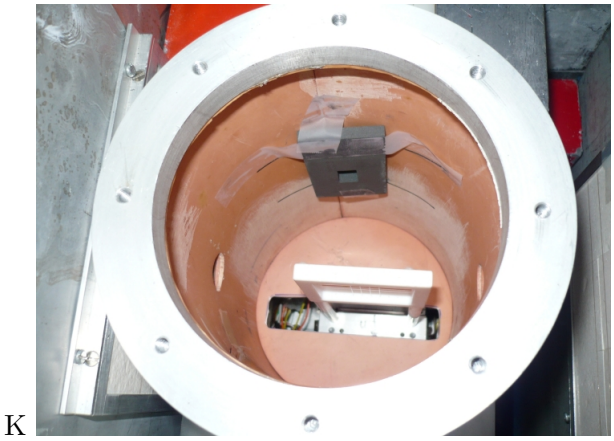

(a) B_4C aperture

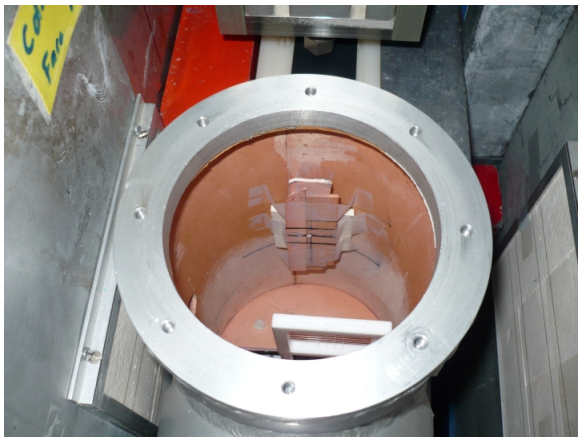

(b) LiF-ceramic + LiF-polymer collimator

Figure 5.3: *Position of the* $2\,x\,2\,\mathrm{mm}$ *neutron collimator. Two kind of collimator combinations were tested; in fig.(a) the* B_4C *collimator and in fig.(b) the LiF-ceramic + -polymer collimator combination.*

5.3 Tuning and tests

The first step in the fine tuning of the motor stages was to determine the conversion between motor coordinates and space coordinates. By measuring with a calliper the distance run by the motor within 1000 steps it was possible to calculate the conversion: 1000 steps = 6 mm.
In this case, no visualization system, like the neutron radiography system in the PGAI setup, is present. A simple solution to overcome this deficiency is the use of a Röngten film (from Advanced Materials - US, type: GAFCHROMIC RTQA-1010) to visualize the neutron field. In this way, it was possible to check the dimensions of the neutron field and the reference position as well as the maximum position of the two stages of the motor. In fig. 5.4 the neutron beam *photo* obtained with the Röngten film is shown .
From this image, the neutron field was deduced ($2.5 \times 2.5\,\mathrm{mm}^2$) and the maximum and reference

(a) Neutron beam (b) Cd wires and Gd Point

Figure 5.4: *Neutron beam at the sample position. The reference point and the maximum point defined by the two stages motor are shown. In fig. (b) is shown the sample for the centre coordinates search.*

positions were localized. The next step was the determination of the middle position of the sample holder. This task was done first visually from the photo of the neutron beam for the coordinates (3000;3000) (see fig. 5.4(a)).
A more systematic search was done afterwards using PGAA spectra. On the sample holder, two Cd wires were mounted on the two directions and the crossing point was in the centre of the holder. The two wires allowed to check the horizontal and the vertical coordinate for the centre. The results are shown in fig. 5.5(a) and fig. 5.5(b) respectively. Furthermore, to check if the coordinates obtained were correct, a Gd point sample was also mounted and a more refined 2D scan of the centre was done.
2D maps of the Cd wires and the Gd point sample showed a disagreement in the center position. The coordinates found by the analysis of the profiles of the Gd point (fig. 5.5(e)) were (2953;3220). This values were obtained fitting the profile data with a Gaussian function (for simplicity this function was chosen, a more detailed fitting procedure for this kind of measurements can be found in [54]). The coordinates obtained from the scan of the Cd wire along the two directions are (3012;3093).
Because the Cd wires and the Gd point were mounted manually on the sample holder, the positioning was not so precise. From the data obtained and some manual measurement with a calliper on the sample, the centre coordinates were defined: **(2953;3093)**. The uncertainty on the centre coordinates is around 1.5 mm and it is strongly cconnected to the dimensions of the

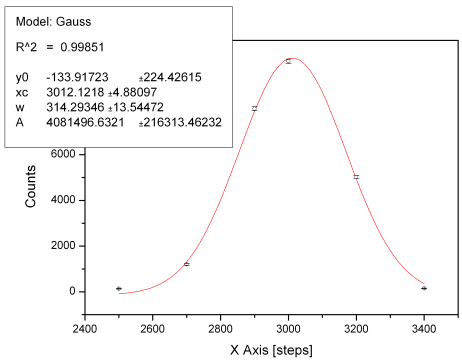

(a) Horizontal scan with Cd wire

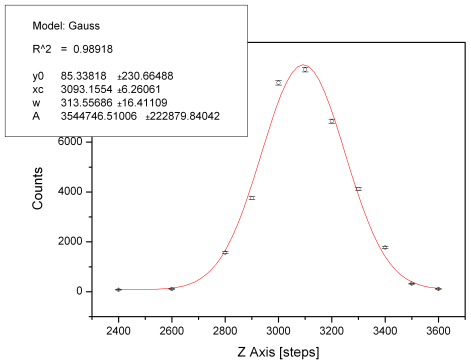

(b) Vertical scan with Cd wire

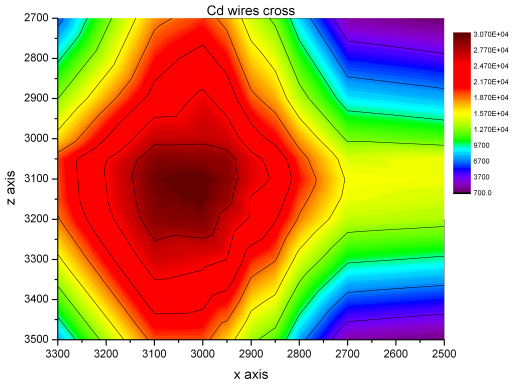

(c) 2D map Cd cross

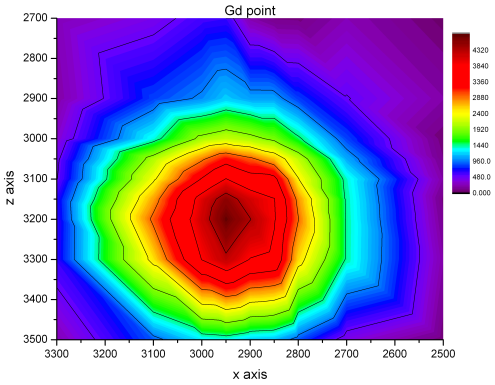

(d) 2D map Gd point

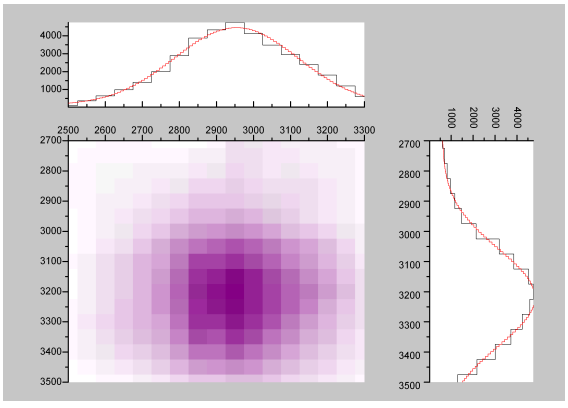

(e) Gd point profiles

Figure 5.5: *The centre of the sample holder was searched through an horizontal and vertical scan for the Cd wires and 2D scan for Cd wires and Gd point of the reference sample.*

neutron collimator.
Aside from considerations concerning the centre coordinates, it was possible to see a small difference in the alignment of the Cd wires and the Gd point sample from these measurements, as it is shown in fig. 5.6.

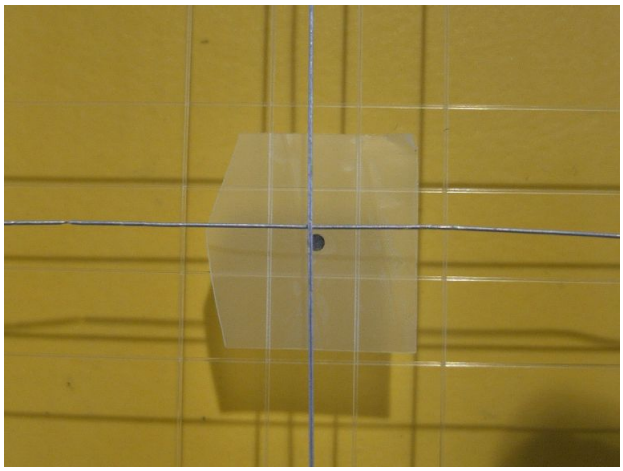

Figure 5.6: *Position of the Gd point compared to the crossing point of the Cd wires.*

5.4 2D Imaging

Once the centre coordinates were found a test measurement was carried out. In fig. 5.7 the sample built for the test measurement is shown.

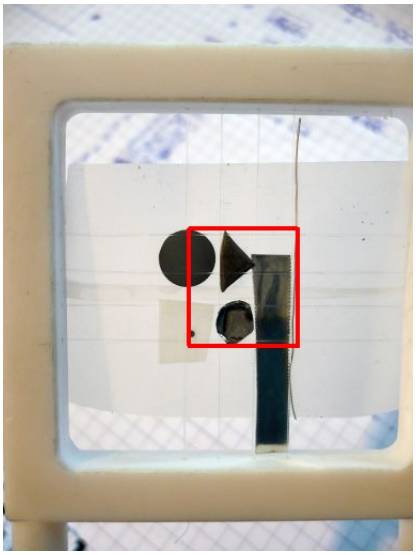

Figure 5.7: *Sample used for the 2D-PGAA imaging with different materials. The scanned area is highlighted.*

The sample was made of 6 different materials with an easy geometrical shape. For each material, the 2D maps are shown in fig. 5.8.

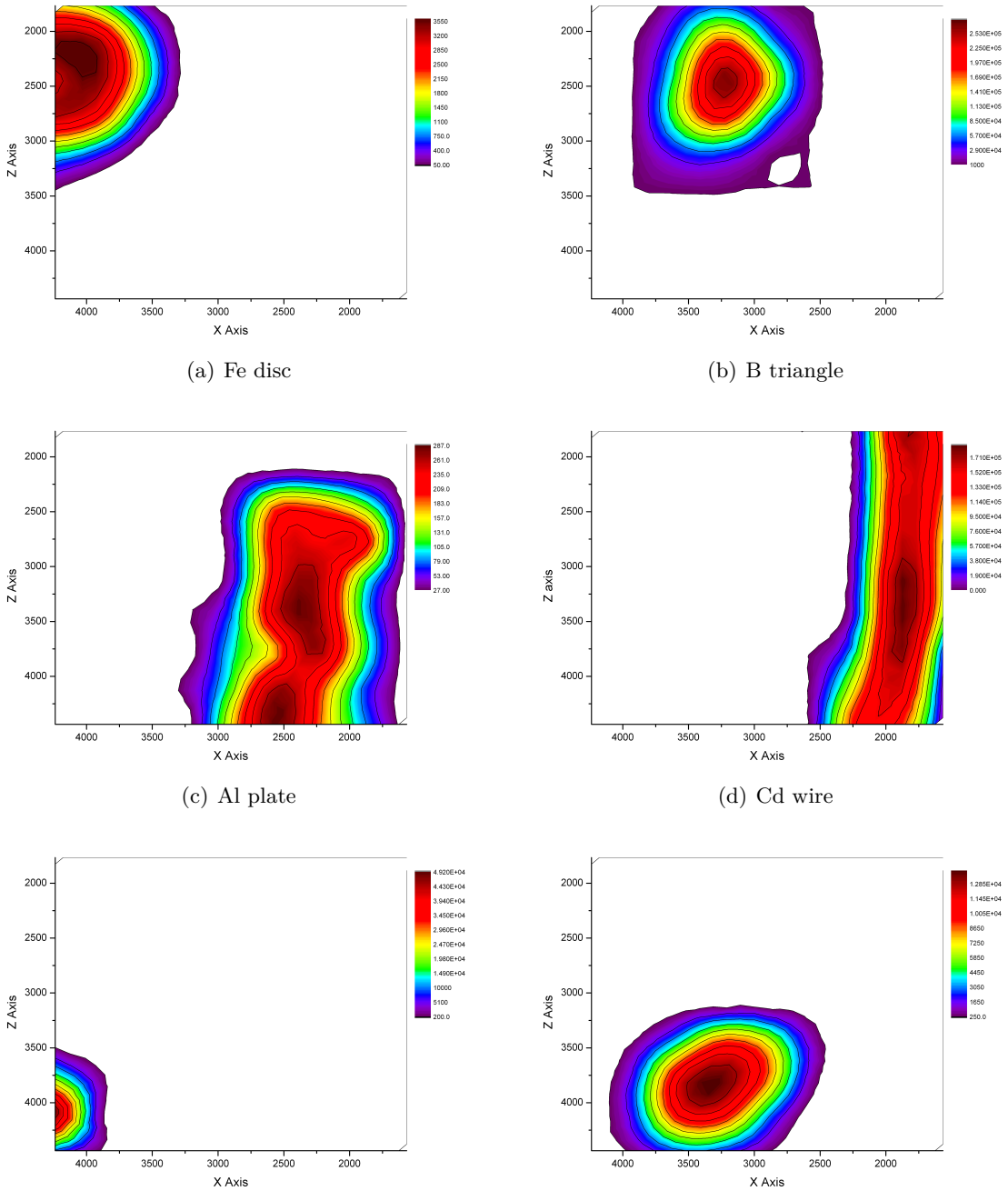

(a) Fe disc

(b) B triangle

(c) Al plate

(d) Cd wire

(e) Gd point

(f) Ti disc

Figure 5.8: *2D maps of the materials for the 2D imaging test.*

As it can be seen from the 2D maps, the different materials were correctly localized. However, a precise geometrical description of the materials is not always possible due to the poor spatial resolution of the neutron collimator ($2 \times 2\,\mathrm{mm}^2$). If the real dimensions of the material are larger compared to the collimator dimensions, a good approximation of the sizes can be estimated through the analysis of the profile of the counts. As an example the real diameter of the Fe disc is 8 mm and the value obtained by the 2D scan is 8.5 mm. In contrast, the Cd wire can be localized on the 2D map, but the estimation of diameter yields a deviation of more than 100% from the real size (0.25 mm).

CHAPTER 6

Allende Meteorite

PGAA is a competitive method for geological analysis thanks to its multi-elemental property. In the past, different measurements on geological samples were already carried out using the PGAA method. In this section, the focus is not on the ability of PGAA to determine the composition of geological samples, but on the potential analysis of non-homogeneous geological samples with the imaging method developed for PGAA. To test this, a small piece of the Allende meteorite (AL 1) was chosen.

6.1 Introduction

The Allende meteorite fell in February 1969 near a small Mexican village, Pueblito de Allende, and it is among the most studied meteorites. The structure of this meteorite is very heterogeneous, with lots of inclusion, also named *chondrules*. This puts this object in the group of CV3 carbonaceous chondrites. The dimensions of these inclusions are pretty large and they can also be seen by the naked eye [56, 57].
This particular structure makes this meteorite suitable for imaging investigations.

6.2 First comprehensive tests on the meteorite

A small part of the Allende meteorite was used to test for the first time all the possible measuring features available at the PGAA instrument. The full set of measurements was carried out on occasion of the installation of the PGAI setup developed for the EU project ANCIENT CHARM. Standard PGAA measurements were followed by 2D maps of the element distribution and finally a 3D tomography of the small meteorite was acquired.
The results of this first comprehensive study were encouraging. PGAA results were in good agreement with literature data, 2D maps of the major elements (Fe, Mg and Si) were obtained and, despite the small dimensions, the tomography images acquired were more accurate than previously thought. The results from this set of measurements, encouraged the development of a more dedicated setup for 2D imaging. The details of this comprehensive study of the Allende meteorite can be found in the following work published in the scientific journal “Applied Radiation and Isotopes”:

Applied Radiation and Isotopes 67 (2009) 2070–2074

Contents lists available at ScienceDirect

Applied Radiation and Isotopes

journal homepage: www.elsevier.com/locate/apradiso

PGAA, PGAI and NT with cold neutrons: Test measurement on a meteorite sample

Lea Canella [a,*], Petra Kudějová [a,b], Ralf Schulze [b], Andreas Türler [a], Jan Jolie [b]

[a] Technische Universität München, Institut für Radiochemie, Lichtenbergstr. 1, 85748 Garching, Germany
[b] Universität zu Köln, Institut für Kernphysik, 50937 Köln, Germany

ARTICLE INFO

PACS:
28.41.Rc
82.80.Jp
29.30.Kv
29.25.Dz

Keywords:
PGAA
PGNAA
PGAI-NT
Meteorite composition
Gamma spectrometry

ABSTRACT

First comprehensive analysis with PGAA, Prompt Gamma-ray Activation Imaging (PGAI) and neutron tomography (NT) techniques at the research reactor FRM II was tested on a piece of the Allende meteorite.

With the PGAA method the bulk elemental composition of the heterogeneous meteorite was determined. Due to the small dimension of the sample, only the 2D elemental distribution of the object was derived with position sensitive PGAI analysis. As an example 2D maps for Si, Fe and Mg are presented. Neutron tomography of the meteorite was carried out with the same cold neutron beam.

1. Introduction

The neutron beam guide NL4b at the research reactor, Forschungsneutronenquelle Heinz Maier-Leibnitz (FRM II), in Garching is dedicated to the new Prompt Gamma-ray Neutron Activation Analysis facility (PGAA or PGNAA) and to experiments that make use of a similar setup. The key feature of the PGAA station is the cold neutron beam with a very high intensity due to the elliptically tapered design of the neutron guide or (only the last 7 m). PGAA is a non-destructive radioanalytical technique that employ the (n,γ) reaction for the determination of the elemental composition of different kinds of samples. The main advantages of this technique, compared to the standard Neutron Activation Analysis (NAA), are the shorter irradiation times and the easy preparation of the samples and the possibility to have a complete analysis within one day. Moreover it is also possible to determine light elements like for example H, B and N (Baechler et al., 2003).

At the PGAA station at FRM II, the neutrons are focused at the sample position with a maximum thermal equivalent flux of 2.7×10^{10} n/cm^2 s (7.3×10^9 n/cm^2 s using the measured mean energy of neutron spectrum, 1.83 meV). Additionally, the neutron beam guide can be extended by a 1.1 m long Helium gas-flushed removable guide, the so-called *elliptical nose*. The neutrons are then focused in a smaller spot with a further gain in intensity, resulting in a flux of 2×10^{10} n/cm^2 s (thermal equivalent 7.4×10^{10} n/cm^2 s) (Forschungsneutronenquelle Heinz Maier-Leibnitz (FRM II), 2008; Kudějová et al., 2008).

The elliptical tapered design of the neutron guide was developed with the goal to have a focused and intense neutron beam for position-sensitive PGAA (Kudějová, 2005). This method, recently called Prompt Gamma-ray Activation Imaging (PGAI), gives a 3D information on the element distribution in the sample. The PGAI setup allows to acquire PGAA data for a small volume that can be repeated by scanning the whole object and, once the data are analysed, those measurements give the spatial distribution of elements inside the object under study. The positioning of the object for the PGAI measurements is possible with the help of a small neutron tomography (NT) setup. The combination of these two methods is called PGAI-NT.

Recently, in the frame of the EU project Ancient Charm (ACIENT CHARM project, 2008; Gorini, 2007), this new setup was developed and tested by the PGAA group at the NIPS facility in Budapest and the PGAA group at FRM II in cooperation (Kastovszky and Belgya, 2006; Belgya et al., 2008a). In June 2008 the PGAI-NT setup was installed at the PGAA station at FRM II. To test all the different measuring possibilities at the instrument, a small piece of the Allende meteorite was measured. On this small sample PGAA, PGAI and NT were performed.

* Corresponding author. Tel.: +49 89 289 14758; fax: +49 89 289 14911.
E-mail address: lea.canella@frm2.tum.de (L. Canella).

0969-8043/$ - see front matter © 2009 Elsevier Ltd. All rights reserved.
doi:10.1016/j.apradiso.2009.05.008

2. Experimental

2.1. Standard PGAA

The elliptical removable part of the guide allows to choose between two different measuring positions with different properties:

- Position 1: The neutron focus is at 35 cm from the end of the beam guide with a usable area of 14 mm × 38 mm (width × height).
- Position 2: With the elliptical nose, the focus is at 10 cm from the end of the beam guide and the useful area now is smaller: 4 mm × 10 mm.

Another factor that allows to have multiple measurement configurations are three neutron attenuators. These attenuators, and their combinations, allow different beam intensities, which means an additional optimisation of the irradiation conditions based on the sample itself.

For the data acquisition, two standard Compton-suppressed gamma spectrometers are in use:

- Det.1: HPGe detector with relative efficiency of 60% (ORTEC poptop) inserted in a annulus of BGO scintillators (coaxial geometry).
- Det.2: HPGe detector with relative efficiency of 36% surrounded by a NaI(Tl)/BGO scintillation system (perpendicular geometry).

The sample chamber can be evacuated in order to suppress the gamma-ray background coming from the neutron capture on air (mainly on nitrogen). The characterisation of the instrument, i.e. efficiency calibration curve, non-linearity curve and background determination, is a fundamental point for the reliability of the measurements (results and discussion about this topic will be published soon by L. Canella et al.).

2.2. Prompt gamma-ray activation imaging and neutron tomography

The intersection of a pencil neutron beam and a small gamma collimator in front of the detector defines the active measurement position (also called *isovolume*) inside the sample. The pencil beam is obtained introducing a ^{6}Li-neutron collimator that reduces the neutron beam to a spot of 2 mm in diameter. While the field of view of the detector is restricted by a Pb collimator of 3 mm in diameter (Belgya et al., 2008b). The scanning of the sample is with the help of a *xyzω* moving table. Moreover, a neutron tomography system is added to the setup. This second system allows to acquire a 3D image of the sample under study. The NT, which reveals the inner structure of the object is useful for the correct positioning of the sample into the pencil n-beam and for the navigation, which is a non-trivial task. The scheme in Fig. 1 helps to understand the basic concept of this setup. For automatic PGAI scans of the samples a digital acquisition system with configurable acquisition software is in use. The final goal of the PGAI-NT is to combine the 3D image of elemental distribution obtained by PGAI and the tomographic reconstruction to have complementary information of the objects structure. The PGAI-NT setup is described in more detail elsewhere (Schulze et al., to be published).

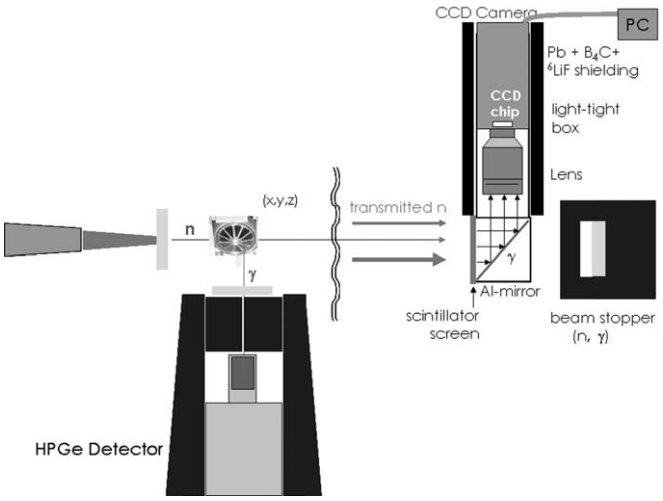

Fig. 1. Schematic view of the PGAI-NT setup.

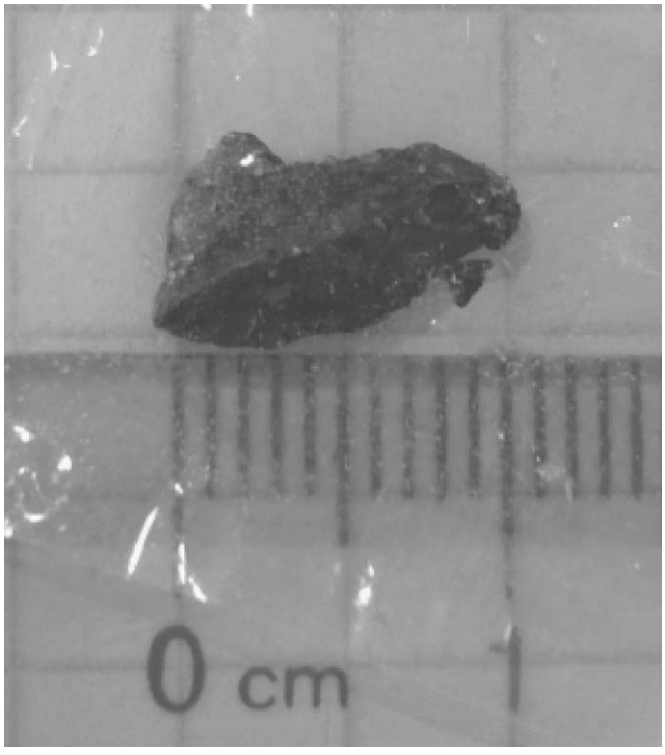

Fig. 2. The Allende meteorite under study (220 mg).

3. Results and discussion

A small meteorite was measured to test all the above described techniques and setups available. On this sample standard PGAA, PGAI and NT were carried out. The results are quite encouraging showing a good performance of the instrument. The sample under study was a piece of the Allende meteorite (220 mg), Fig. 2. This kind of meteorite belongs to the group of stony carbonaceous chondrites and it is very inhomogeneous.

3.1. PGAA measurement

The small meteorite was first measured with the standard PGAA setup and the results of the analysis are shown in Table 1.

Table 1
Comparison between the PGAA values obtain at FRM II and Budapest and literature values on the Allende meteorite obtained by Jarosewich (1990) and Kallemeyn and Wasson (1981).

El.	FRMII	Budapest[a]	Jaros.	Kall.
H	0.343 ± 0.004	0.2572 ± 0.0060	–	–
Na	0.239 ± 0.060	0.1155 ± 0.0067	0.334	0.329
Mg	13.00 ± 0.58	13.20 ± 0.69	14.85	14.80
Al	1.377 ± 0.060	1.406 ± 0.036	1.731	1.760
Si	14.81 ± 0.38	14.68 ± 0.34	16.00	–
S	0.930 ± 0.025	0.913 ± 0.021	1.470	–
Cl	0.0162 ± 0.0059	0.0102 ± 0.0006	–	–
K	–	0.0199 ± 0.0026	0.0249	0.0294
Ca	1.647 ± 0.052	1.444 ± 0.045	1.865	1.880
Ti	–	0.078 ± 0.016	0.0899	–
Cr	0.357 ± 0.010	0.334 ± 0.008	0.356	0.363
Mn	0.1350 ± 0.0039	0.1396 ± 0.0026	0.1394	0.1450
Fe	23.95 ± 0.46	23.85	23.85	23.70
Co	0.0410 ± 0.0015	0.0391 ± 0.0008	0.01–0.02	0.0662
Ni	0.879 ± 0.026	0.868 ± 0.015	0.36–0.85	1.33
Sm	–	20.1 ± 3.04 ppm	47.8 ppm	29.8 ppm

All the values are in $\%_w$ and errors are in $1-\sigma$ standard deviation.

[a] The values are normalised for the Fe concentration by Jarosewich (1990).

Fig. 3. Reconstructed image of the Allende meteorite fragment obtained with neutron tomography at the PGAA station.

For comparison, literature values for the composition are given there as well. The interesting part is the comparison with the PGAA measurement carried our for the same piece of the Allende meteorite at the Budapest PGAA station. The irradiation conditions at the PGAA station at FRM II were slight different from those of the facility in Budapest. The acquisition time was 3270 s and using the elliptical nose and two attenuators, the neutron flux was 1.8×10^9 n/cm^2 s thermal equivalent (4.9×10^8 n/cm^2 s for cold neutrons), while in Budapest, due to the lower flux intensity (5×10^7 n/cm^2 s thermal equivalent), the sample was measured for about 14 h (Molnár et al., 1997).

The results obtained at FRM II are in a good agreement with those obtained in Budapest, e.g. Mg, Si, S, Mn, Fe, and Ni give the same result within one standard deviation. Nevertheless there are some discrepancies in the amount of H, Cl and Na, moreover K, Ti and Sm were not detected. Probably the rather short measurement time did not allow to detect K, Ti, and Sm that are present in very low concentration. While the reason for the discrepancies in the concentration of H, Cl and Na could be the interference with the background, that could be not well calibrated for the purpose. Further investigation to solve this problem is necessary. Moreover, the differences between our measurement and the values given by Jarosewich (1990) and Kallemeyn and Wasson (1981), are probably caused by the heterogeneity of the Allende meteorite. Only a very small portion of the meteorite was analysed (220 mg), while the literature values give the average concentration on the whole pieces of the Allende meteorite.

In this measurement the sample chamber was not evacuated, so the background contribution was higher. Such background conditions make it difficult or even impossible to detect trace element like for example Sm. Thus a further optimisation of the background is needed. Aside these considerations, the results obtained are encouraging.

3.2. NT and PGAI

After the PGAA measurement the setup of the instrument was changed in order to acquire a neutron tomography by rotating and a PGAI by scanning the same sample. The reconstructed image of the Allende meteorite obtained through NT is shown in Fig. 3. Usually, depending on the divergence of the neutron beam, a full neutron tomography is obtained through 400 neutron radiographies of the sample taken on the whole rotational angle of 360° (a radiography every 0.9°). In this case the image was reconstructed using only 300 radiographies, because of an unexpected problem in the main shutter of the neutron guide hall occurred during the acquisition time that stopped the acquisition. The exposure time for each image was of 1 s.

The spatial resolution of the 3D image is only about 0.4 mm. This is mainly due to the divergence of the neutron beam, and due to the non-optimised field of view of the CCD camera. Moreover the sample holder used in this measurement (a polytetrafluoroethylene(-PTFE) holder) gave some difficulties in the reconstruction of the final image. This kind of sample holder was too massive for the purpose, thus less transparent to neutrons.

The NT is a very practical tool in the selection of the points to measure inside the sample with PGAI, because it reveals the deep structure of the sample itself and so the navigation to the interesting parts is possible. This method is of great interest for highly inhomogeneous samples and e.g. small museum object, also because it is a non-destructive technique (see Ancient Charm project). In this example unfortunately the achieved resolution and the small dimensions of the sample cannot offer a better view of the inner structure. Nevertheless this test measurement can be considered a good starting point for a future development of this feature.

The meteorite was measured with PGAI. The 2D charts for the main elements found inside the meteorite, i.e. Fe, Si and Mg are shown in Fig. 4. The profile lines defines the distribution of the counts for the given element. All the spectra were taken for the same measurement time so there was no need to normalise the counts for the time. The scanning grid was prepared based on the neutron radiographies and tomography of the meteorite. The grid for the motor movement covered the whole area of the sample (12.5 mm × 6 mm) with a resolution of about 2 mm × 2.5 mm per γ-spectrum, giving 15 spectra in total.

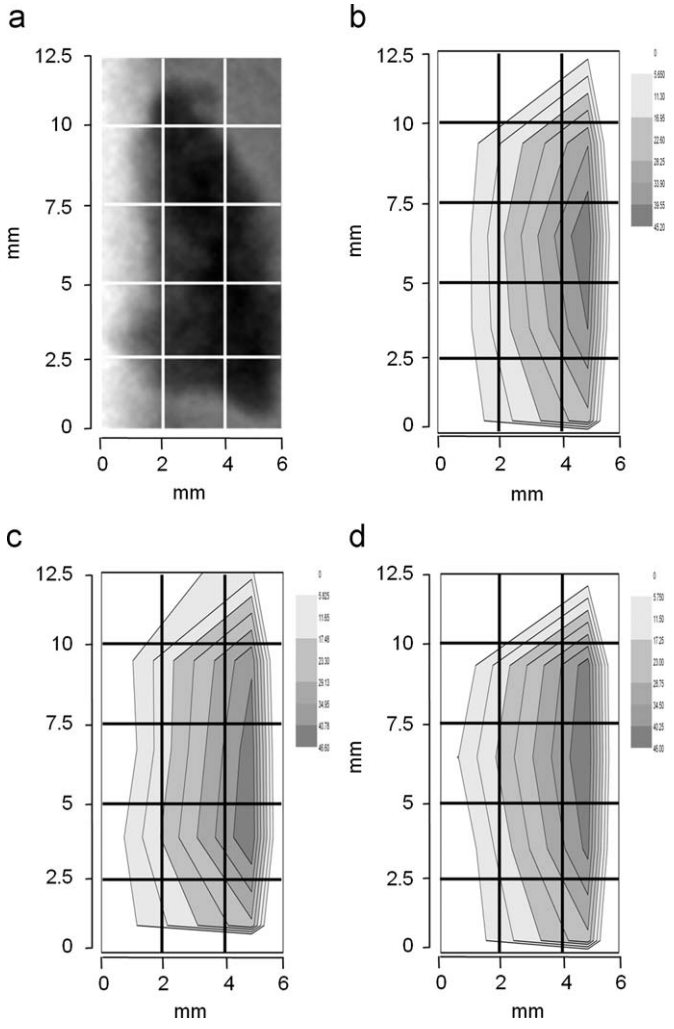

Fig. 4. 2D distribution of the main elements Fe, Si and Mg obtained with PGAI. (a) Radiography of Allende meteorite. (b) Si 2D distribution. (c) Fe 2D distribution. (d) Mg 2D distribution.

In this case the narrow γ-collimator for usual PGAI was not used because the thickness of the sample itself was exactly comparable with the thickness of the isovolume. This arrangement allowed only a 2D measurement and a higher count-rate that shortened the acquisition time to about 1 h (3557 s) per spectrum. The analysis of the spectra was performed with Hyperlab software (Hyperlab software, 2008). This software allows the analysis in a batch of all the spectra at once. The elemental maps are obtained using the counts found for the main prompt-γ-line of the element under study.

These are the prompt-γ-lines used for the distributions reconstruction:

- Si: 3538.966 keV;
- Fe: 7631.136 keV;
- Mg: 585.00 keV.

As it can be seen from Fig. 4 the distributions for Fe, Si and Mg are all different, but all the elements have the higher amount on the right side of the sample, where the object is thicker. The radiography in Fig. 4(a) was taken before the PGAI measurements and it helps in the visualisation of the distribution maps.

It is not yet possible to give some quantitative values of the element concentrations. Further improvement on the analysis of the gamma spectra should be done. It is a challenging task because there are many factors that have to be taken into account; for example, the different amount of material in the beam for each position. Corrections for the amount of material in beam and for the thickness have to be calculated and incorporated in the maps. This information is quite important in this case and in similar objects, where the structure is neither regular nor symmetric. In this measurement a first very rough correction for the amount of material in the beam is given. According to the grid the thickness of the meteorite was measured manually along the x and y axis trying to follow the lines defined in the scan grid, and for each measuring point the average thickness measured along the two axis was taken. The distributions in Fig. 4 are corrected with this rough mass correction factor but in a further development of the technique this information can be derived more precisely from the tomography made on the sample.

4. Conclusions

All the measuring possibilities at the PGAA station at the research reactor FRM II in Munich were tested on a small piece of the Allende meteorite. The information obtained are a bulk determination of the elemental composition, with standard PGAA, and 2D maps for the three major elements determined with the PGAI-NT technique. The elemental composition measured with PGAA was in a good agreement with the values obtained in Budapest and with the literature values. There are still some parameters to be optimised, but these first results are satisfactory.

The PGAI-NT technique needs more improvements, however, for a first trial the performance of the new method is encouraging. The main difficulty of this technique is the geometrical alignment of the setup, which is a challenging and time consuming task. Furthermore, the analysis of the data has to be further studied. Correction methods for gamma-attenuation and neutron-self-absorption have to be developed and calculated.

Acknowledgements

We would like to thank M. Mühlbauer for the help with the NT reconstruction, the Budapest PGAA group for the cooperation on the PGAI setup and Prof. H. Palme for providing us the Allende meteorite.

References

ACIENT CHARM project, 2008. Official web page of the ACIENT CHARM project, November. URL: ⟨http://ancient-charm.neutron-eu.net/ach⟩.
Baechler, S., Kudějová, P., Jolie, J., Schenker, J.-L., 2003. The k0 method in cold-neutron prompt gamma activation analysis. J. Radioanal. Nucl. Chem. 256, 239–245.
Belgya, T., Kis, Z., Szentmiklósi, L., Kastovszky, Z., Festa, G., Andreanelli, L., DePascale, M.P., Pietropaolo, A., Kudejova, P., Schulze, R., Materna, T., the Ancient Charm Collaboration, 2008a. A new PGAI-NT setup at the NIPS facility of the Budapest research reactor. J. Radioanal. Nucl. Chem. 278, 713–718.
Belgya, T., Kis, Z., Szentmiklósi, L., Kastovszky, Z., Kudejova, P., Schulze, R., Materna, T., Festa, G., Caroppi, P., the Ancient Charm Collaboration, 2008b. First elemental imaging experiments on a combined PGAI and NT setup at the Budapest research reactor. J. Radioanal. Nucl. Chem. 278, 751–754.
Forschungsneutronenquelle Heinz Maier-Leibnitz (FRM II), 2008. URL: ⟨http://frm2.tum.de/pgaa⟩, November.
Gorini, G., for the Ancient Charm Collaboration, 2007. Il Nuovo Cimento (1), 1–12.
Hyperlab software, 2008. URL: ⟨http://www.hlabsoft.com/⟩, November.
Jarosewich, E., 1990. Chemical analysis of meteorites: a compilation of stony and iron meteorite analysis. Meteoritics 25, 323–337.

Kallemeyn, G., Wasson, J.T., 1981. The compositional classification of chondrites—i. The carbonaceous chondrite groups. Geochim. Cosmochim. Acta 45, 1217–1230.

Kastovszky, Z., Belgya, T., the Ancient Charm Collaboration, 2006. Archeometriai Múhely III 2, 16–21.

Kudějová, P., 2005. Two new installations for non-destructive sample analysis: PIXE and PGAA. Ph.D. Thesis, Universität zu Köln.

Kudějová, P., Meierhofer, G., Zeitelhack, K., Jolie, J., Schulze, R., Türler, A., Materna, T., 2008. The new PGAA and PGAI facility at the research reactor FRM II in Garching near Munich. J. Radioanal. Nucl. Chem. 278, 691–695.

Molnár, T., Belgya, T., Dabolczi, L., Fazekas, B., Révay, Z., Veres, A., Bikit, I., Kiss, Z., Östör, J., 1997. The new prompt gamma-activation analysis facility at Budapest. J. Radioanal. Nucl. Chem. 1997, 111–115.

6.2.1 Measurements 2010

In 2010, the same piece of the Allende meteorite was investigated again with PGAA and the newly optimised 2D-PGAA (see chapter 5). The main aim was to compare the new results with the ones obtained from the 2009 campaign, especially for the 2D measurements.
In table 6.1, the determination of the elemental composition with PGAA for the Allende meteorite is presented and compared with the values obtained in 2009 and the literature ones.

Element	*AL 1 2009*	*AL 1 2010*	*AL 1 Budapest*	*Jarosewich [58]*	*Kallemeyn [59]*
H	0.343(4)	0.259(4)	0.257(6)	–	–
Na	0.24(6)	0.18(2)	0.116(7)	0.334	0.329
Mg	13.0(6)	13.4(7)	13.2(7)	14.85	14.80
Al	1.38(6)	1.44(4)	1.41(4)	1.731	1.760
Si	14.8(4)	14.5(5)	14.7(3)	16.00	–
S	0.93(3)	0.97(2)	0.91(2)	1.470	–
Cl	0.016(6)	0.0111(4)	0.0102(6)	–	–
K	–	0.0146(19)	0.0199(26)	0.0249	0.0294
Ca	1.65(5)	1.54(5)	1.44(5)	1.865	1.880
Ti	–	0.081(2)	0.078(16)	0.0899	–
Cr	0.357(10)	0.347(9)	0.334(8)	0.356	0.363
Mn	0.135(4)	0.144(4)	0.140(3)	0.1394	0.1450
Fe	24.0(5)	24.4(6)	23.85	23.85	23.70
Co	0.0410(15)	0.0376(9)	0.0391(8)	$0.01 - 0.02$	0.0662
Ni	0.88(26)	0.832(22)	0.868 ± 0.015	$0.36 - 0.85$	1.33
Sm	–	5.1(8) ppm	20.1(30) ppm	47.8 ppm	29.8 ppm

Table 6.1: *Elemental composition of the piece of the Allende meteorite*

The new PGAA results, under the same irradiation conditions, show lower uncertainties with respect to the 2009 measurements. Moreover, it was also possible to detect impurities like K and Sm, which demonstrates that the optimisation carried out on the instrument, improved the measuring conditions.
After the PGAA measurements, the 2D scan was prepared and measured. In order to check if the scanning field was centered on the meteorite, a neutron photo was taken for the maximum and minimum positions of the scanning field. In fig. 6.1, the piece of the Allende meteorite and the neutron scanning field are presented.
The scan grid was made of 15 positions each measured for 3600 s as in the former irradiation. This time, it was possible to use vacuum conditions thanks to the improved 2D setup (see chapter 5). In the following graphs (fig. 6.2) the results obtained for the major elements, i.e. Fe, Mg, and Si, are shown. In order to help with the visualization of the element distributions on the meteorite, a neutron radiography of the Allende meteorite acquired in the first set of measurements, in 2009, is added.
With the improved measuring conditions, also the 2D maps result in more details and the count-rates are higher than in the former measurement. Moreover, it was also possible to detect some impurities, like Co, Cl, and Sm and to locate them on the meteorite. This particular was

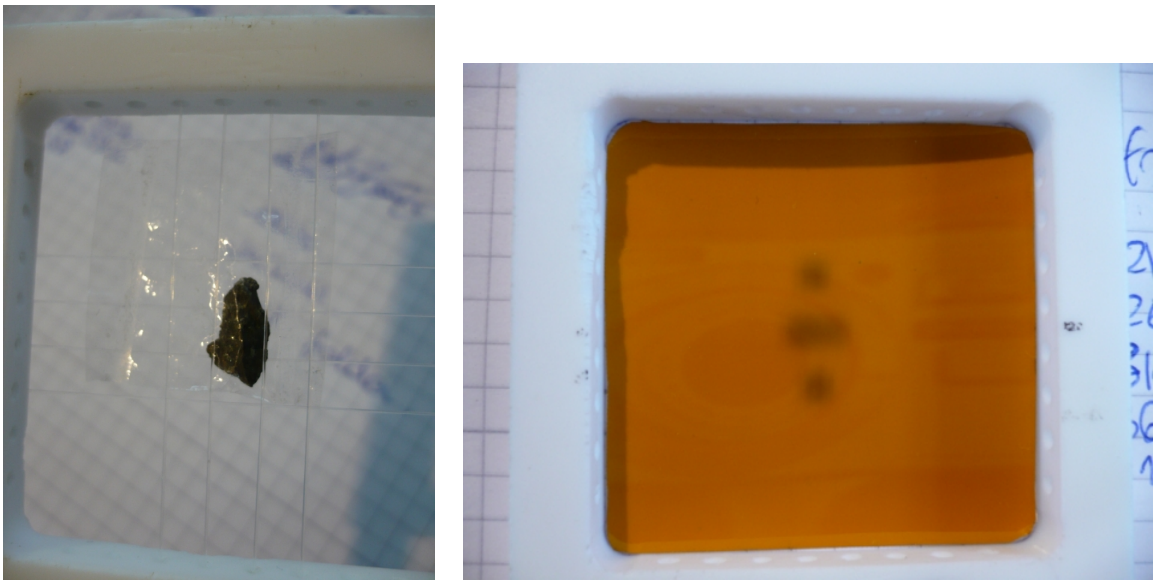

(a) Allende meteorite (b) Neutron scanning field

Figure 6.1: *Allende meteorite positioned on the sample holder and photo of the neutron scanning field.*

not obtained with the ANCIENT CHARM setup. The 2D maps for the trace elements found are shown in fig. 6.3.
The newly developed 2D-PGAA setup showed a better performance with respect to the first 2D measurements carried out with the ANCIENT CHARM setup.
A correction for the material amount irradiated per each position has to be done for this case, too, in order to reconstruct a more realistic 2D distribution of the elements. For the measurements carried out in 2009, a rough correction factor that considers the amount of material irradiated was estimated. According to the measuring scan-grid, the meteorite thickness was measured manually with a calliper along the two directions trying to follow the direction of the programmed grid. For each point defined by the grid the average thickness for each direction was taken and used to calculate a rough volume, i. e. the amount of the meteorite mass in that point. The introduction of this correction factor brought a very slight improvement in the 2D maps of the major elements. The same mass correction was used also on the data acquired in 2010. The normalized distribution maps obtained are again slightly different from the first maps for the major elements, while for trace elements, the differences are more remarkable. As an example, the normalized 2D maps for Si, Cl, and Sm are shown in fig. 6.4.
A more sophisticated method to correct for the mass amount is needed indeed. A more precise volume calculation could be obtained with a 3D imaging method, like for example neutron tomography. The spatial resolution of the method can be improved by the reduction of the neutron field, i.e. the neutron collimator dimensions, at the cost of (much) longer measurement times and a reduced sensitivity.

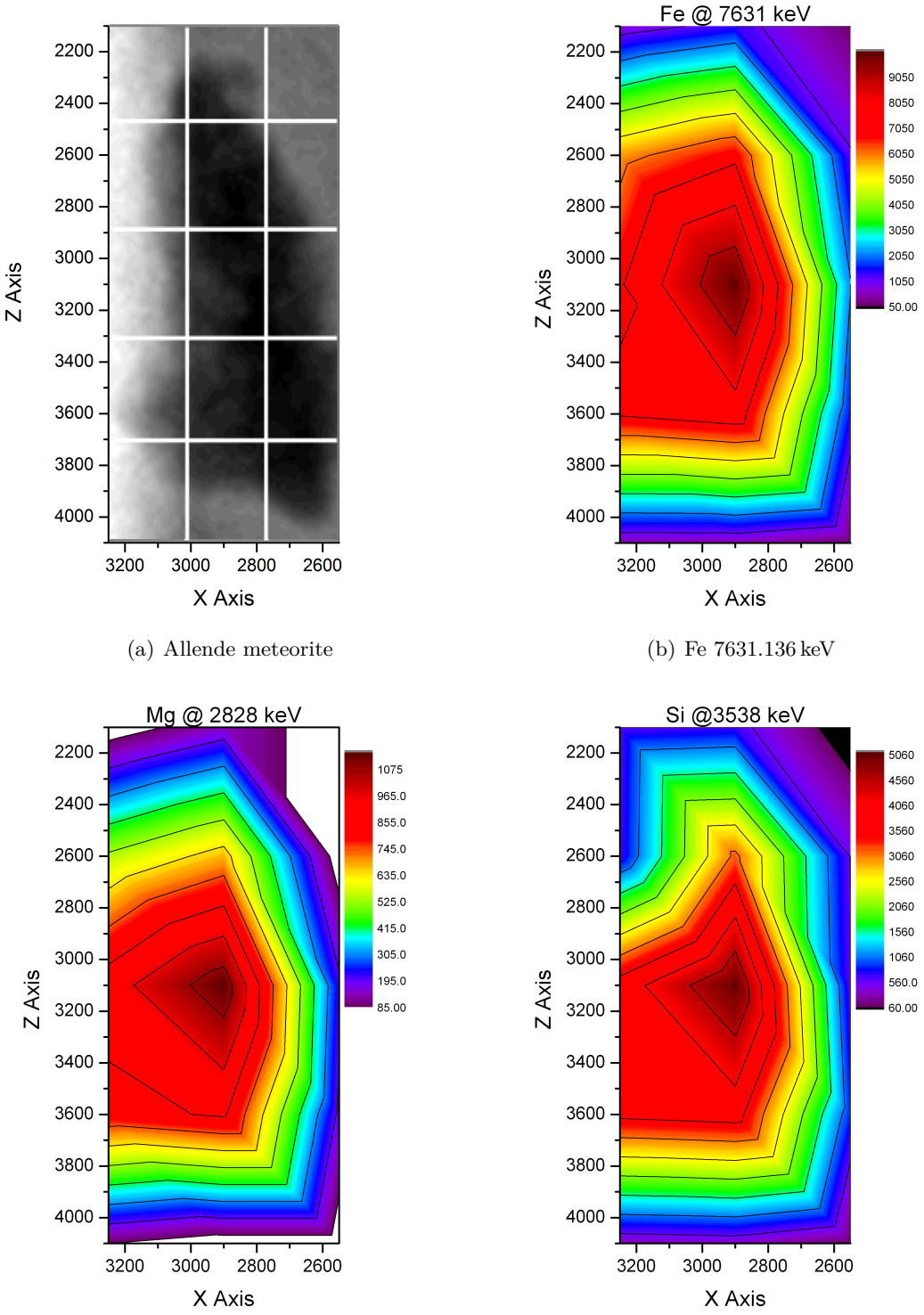

(a) Allende meteorite

(b) Fe 7631.136 keV

(c) Mg 2828.172 keV

(d) Si 3538.966 keV

Figure 6.2: *2D Elemental distributions for the major components of the Allende meteorite; Fe, Mg and Si. As reference the neutron radiography of the Allende meteorite with the scanning grid is also added.*

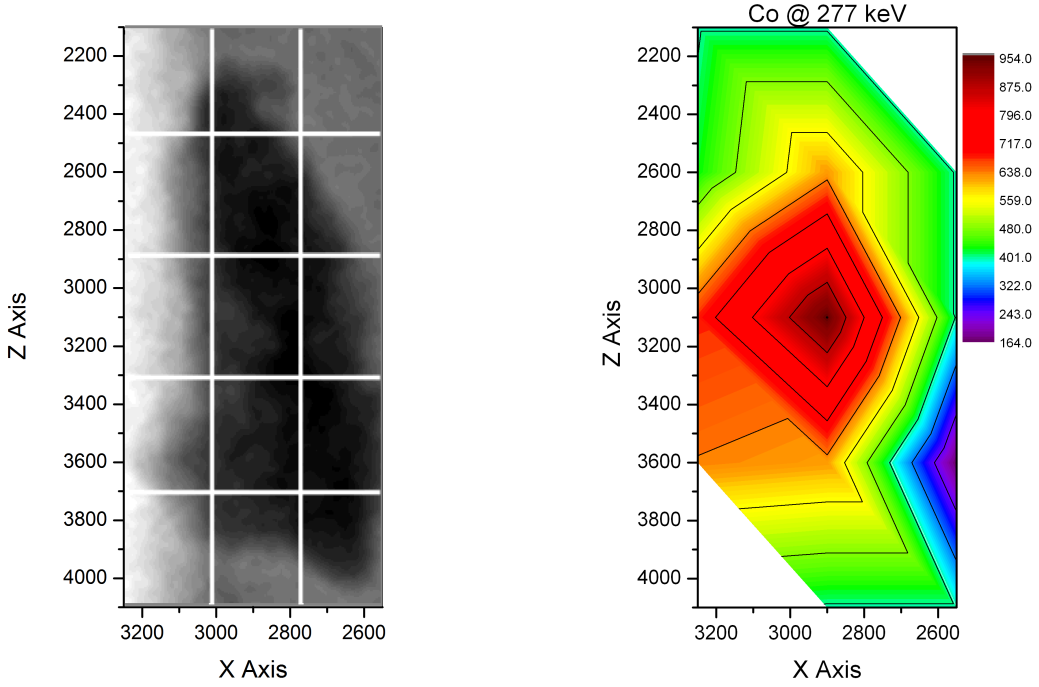

(a) Allende meteorite

(b) Co 277.161 keV

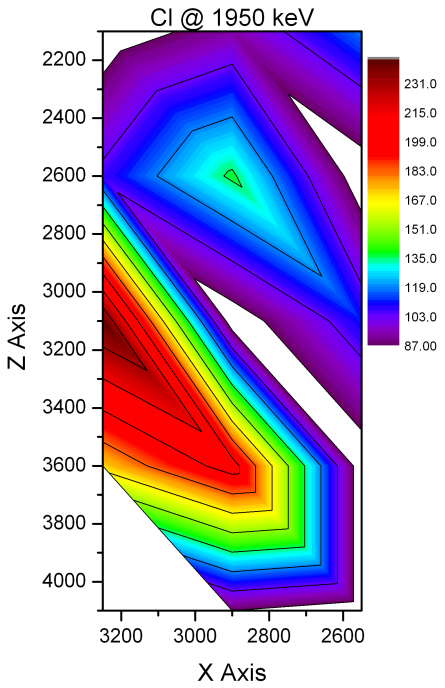

(c) Cl 1951.14 keV

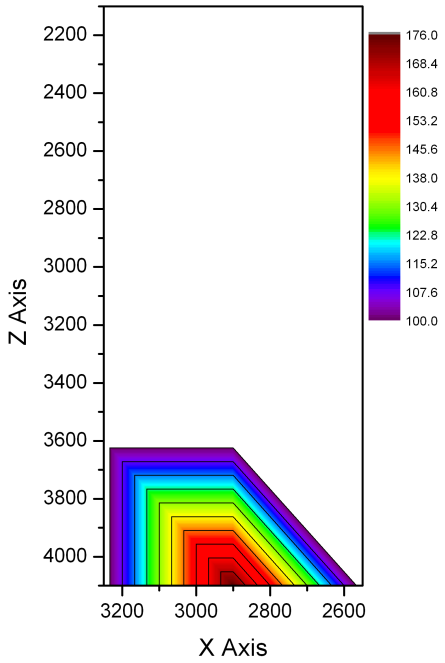

(d) Sm 333.97 keV

Figure 6.3: *2D maps of the trace elements found in the Allende meteorite. As reference the neutron radiography of the Allende meteorite with the scanning grid is also added.*

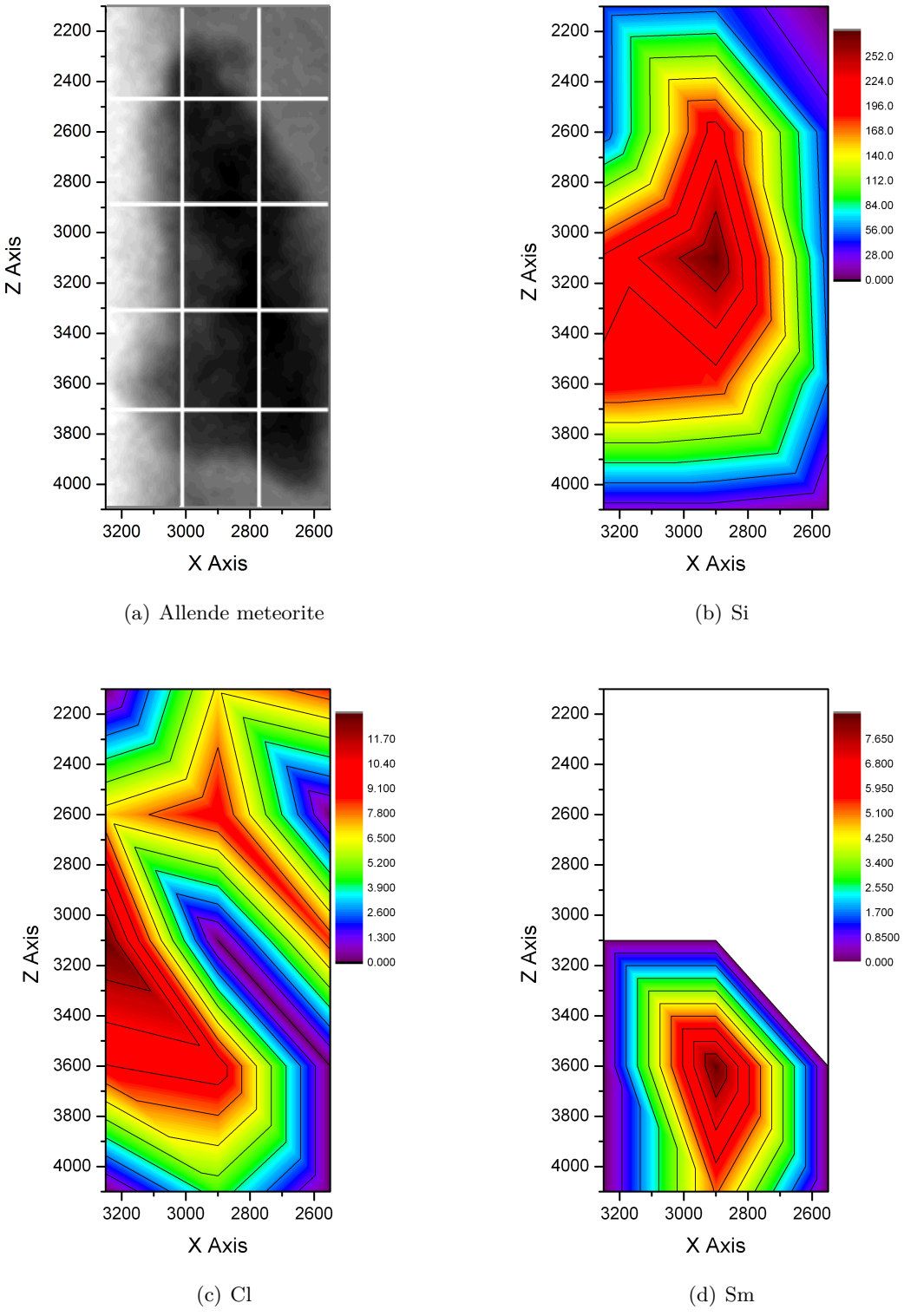

(a) Allende meteorite

(b) Si

(c) Cl

(d) Sm

Figure 6.4: *Mass-corrected 2D maps for the major element Si and for the trace elements Cl and Sm. As reference the neutron radiography of the Allende meteorite with the scanning grid is also added.*

CHAPTER 7

UMo alloy

The HEU-MEU group has purchased sputtering targets consisting of depleted uranium molybdenum alloy U-8Mo (DU-Mo) for the MEU sputtering project. The interest in PGAA measurements was driven by the wish to determine the exact composition of the target material before the sputtering process as well as the composition of the film deposited in the process.
The UMo target used in the sputter process was analysed with the new 2D system at the PGAA station. The goal of this experiments is to understand the distribution of U and Mo inside the target itself. Moreover, sputter deposited foils have been measured with the 2D system, too.

7.1 Introduction: UMo alloy, why?

The compact reactor core of FRM II consists of only one fuel element. Although the thermal power is only 20 MW, the unperturbed neutron flux is approximatively $8 \cdot 10^{14}\,\mathrm{cm}^{-2}\,\mathrm{s}^{-1}$. The particular design of the reactor core allows to build up of the maximum thermal neutron flux

density outside the core at about 12 cm from the fuel element surface. The fuel element is made of 113 involute shaped fuel plates. Each plate consists of U_3Si_2 embedded in Al. The U used in such a compact fuel element is altogether 8 kg with an enrichment of 93%.
In the next years, FRM II should decrease the enrichment of the fuel element. In order to keep the same cycle length with a lower enrichment, it is necessary to develop a high density nuclear fuel. The lowering of the enrichment is followed by a higher neutron absorption from ^{238}U, thus the amount of ^{235}U has to be increased. As the geometry of the fuel element is fixed the only way to increase the U density in the fuel.
The actual fuel element is made of disperse U_2Si_3 and has a maximum U density of $3.0\,g\,cm^{-3}$. The efforts of the actual nuclear fuel research is based on the study of disperse U-alloys with a density between 8.0-9.0 $g\,cm^{-3}$. Several U-compounds were taken into account and according to the performed tests the actual studies are focusing on UMo alloys. The reason was that this alloy (with a Mo concentration between 6 - 9 %) showed an excellent irradiation performance up to high U consumptions [60].
From the current scientific view, some UMo alloys can be a suitable fuel, but for an application at FRM II several issues have to be addressed first. One of these issues is the development of an easy and reliable processing technique for UMo. In this context, the fuel development group at FRM II investigates sputtering as a possible processing technique [2].

7.2 Sputtering process

Sputtering denotes the ejection of surface atoms form a target material induced by a particle bombardment. The projectiles used for bombardment can be molecules, neutral atoms, ions, nuclei and even photons. The energy of the projectile bombardment can have a wide range from few eV up to MeV. However, for technical applications, usually ions at energies between eV and few keV are used.
The energy transfer from the projectile ion to the target atom occurs in two ways: through the transfer of the energy and momentum vector (*physical sputtering*) or through the energy released from a chemical reaction on the surface of the target (*chemical sputtering*). In the first case, the ejected atom receives the necessary energy from a collision or ionizing cascade. In *chemical sputtering*, the chemical reaction between the incoming ion and the atoms of the target creates molecules that have a low binding energy and can be desorb at the current target temperature. Purely physical sputtering process occurs exclusively when noble gas ions are used as projectiles, while for mixed ions the sputtering is a results of both processes.
If an atom receives enough energy to overcome the local binding forces, it can be considered energetically unbound. If it can reach the target surface and the momentum vector is pointed away from the target, the atom is ejected. Sputtering is a threshold process. The energy threshold for an atom ejection corresponds to the ion energy required to remove an atom from the surface of the target. Usually sputtering threshold energies are around 20 and 50 eV, depending on the target material and on the type of ion.
The atoms ejected from the surface are mostly neutral atoms with a broad angular and energetic distribution. The so-called *sputtering yields* are used to describe these distributions. The total sputtering yield describe the absolute number of atoms ejected by one projectile [60].

7.2.1 Preferential sputtering and diffusion

The theory of sputtering alloys (like UMo) and multicomponent materials predicts a change of the composition of the sputtering target as well as of the sputtered deposits due to the so called *preferential sputtering*. Preferential sputtering means, that different atomic components in a material have different sputtering yields and are therefore sputtered not proportionally to their concentration on the surface of the material. The preferential removal of one component from the surface produces a so called altered layer, which is a near-surface region with a composition that is stoichiometrically different from the target bulk material. At sufficiently low temperatures, when thermal diffusion is not important, this altered layer stays at a finite thickness and steady-state conditions can be reached, where the amount of material sputtered from each species becomes proportional to the bulk concentration. If the target temperature gets too high on the other hand, thermal diffusion processes will let the altered layer grow until it envelopes the whole target. In this case the sputtering process will continuously deplete one component in the target resulting in a permanent change of the composition of the target material as well as of the sputtered films [60].
It is evident that for the sputtering of UMo alloys for fuel processing, a change of the composition during the sputtering process is not desired and could even be fatal for the usability of sputtering as a processing technique. Therefore, it is of main interest to clarify if a composition change within the sputtering target or within the sputtered deposit can be observed at the currently used operational conditions and to quantify it.

7.3 PGAA Measurements

The PGAA method is an suitable method for the measurement of uranium and for the determination of the U-enrichment [61]. The samples obtained from the HEU-MEU group were first measured with standard PGAA measurements. The information to gain were the measurement feasibility and a first check of the nominal concentration of Mo inside the alloy.
A piece of the A20 target with a nominal Mo concentration of 8.0 $\%_{wt}$ and with 0.220 $\%_{wt}$ of ^{235}U (data obtained from CERCA, Roman, France) and a piece of the sputter deposit were analysed . The samples were packed inside FEP-bags in order to avoid the contamination of the sample holder. Both samples, the target and the deposit, were measured twice. The first analysis was to determine the optimum irradiation parameters and the second one was to improve the results. The final value is calculated as a weighted average. The Mo/U ratio is calculated using the k_0-method.
The k_0-value for U is taken from the IAEA database as it is a regular $1/v$-nuclide. In this particular case, however, it has to be corrected for the enrichment in ^{238}U. The line chosen for the determination of U in the samples is the line at 4060.35 keV, which is also the most intense prompt-line. The k_0-value for this line for natural U (isotopic abundance 99.274 %) is 0.00237(4). According to the definition, this parameter (chapter 2 and 4) can be recalculated for the actual enrichment. In this way, the new k_0 for the 4060.35 keV line is 0.002382.
For Mo, the chosen line was the line at 778.221 keV, which is produced in the neutron capture by ^{95}Mo. This is the most intense line for Mo, but it is also subject to interference of the decay line 777.921 keV by ^{99}Mo and the decay line 778.29 keV by ^{101}Mo.
^{99}Mo and ^{101}Mo have two production routes; through the fission of ^{235}U with a chain yield of

6.161 % and 5.167 % respectively, and by neutron capture reactions on ^{98}Mo and ^{100}Mo (see fig. 7.1) which are both present in natural Mo and therefore part of the alloy.

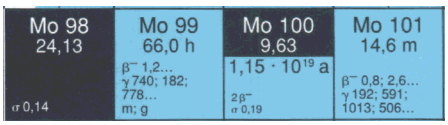

Figure 7.1: *Neutron capture route for the production of ^{99}Mo and ^{101}Mo [62].*

Concerning ^{99}Mo, the neutron capture production route is not so important because the growth rate of ^{99}Mo is strictly connected to the half-life of the nuclide that in this case is 66 h which is not comparable with the irradiation time of 3600 s. This is not the case for ^{101}Mo that has a half-life of only 14.6 m. The fission production route cannot be completely excluded, because even if the UMo samples are made from depleted U, the high cross section of the fission process of ^{235}U can contribute to the production of these two interfering nuclides. In order to check and, in case, to quantify the correction factor for the interference lines, immediately after a one hour long irradiation, a decay spectra was acquired for a duration comparable to that of the PGAA measurements. Fortunately, as it can be see in fig. 7.2 no decay line belonging to ^{99}Mo or/and ^{101}Mo was found.

All the other lines visible in the decay spectra belong to the decay of ^{239}U (half-life of 23.45 min)

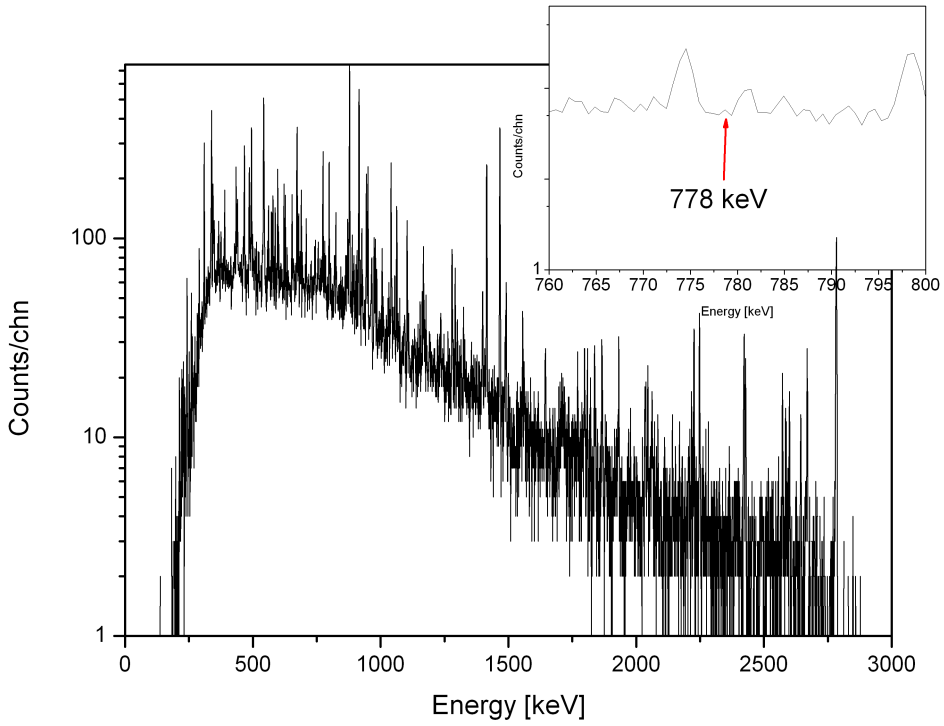

Figure 7.2: *Decay spectrum of UMo target acquired to detect possible interferences lines at 778 keV.*

and ^{239}Np (half-life 2.355 d). The decay of ^{52}V is also visible which is the main impurity found in the alloy. In table 7.1 the results of these first measurements are listed.

ID and irradiation time	U [$\%_{wt}$]	Mo [$\%_{wt}$]	V [$\%_{wt}$]
UMo target, 11.975 mg			
A0407 - 5400 s	92.5(26)	7.29(23)	0.195(7)
A0608 - 10240 s	92.1(25)	7.65(24)	0.222(7)
UMo deposit, 2.5 mg			
A0402 - 7200 s	90.8(46)	9.2(5)	–
A0618 - 16200 s	90.7(41)	9.3(4)	–

Table 7.1: *U and Mo concentration measured with standard PGAA.*

The rather large uncertainty is due to the very low amount of material, nevertheless the results for the sputtered deposit are in pretty good agreement with the ICP-OES result (9.2(6) $\%_{wt}$ Mo, Institut für Radiochemie, TUM), while the EDX measurement are not in agreement (7.5(9) $\%_{wt}$ Mo). The discrepancy between the Mo in the target material and in the foil may suggest the possibility of preferential sputtering effects, although the dimension of the samples were too small to confirm this assumption.

7.4 2D PGAA

The unsolved questions after PGAA standard measurements suggested to investigate the UMo targets as well as the deposits in more detail. The main open problem are the diffusion effects in the target material and preferential sputtering and ejection processes in the deposits. The newly optimised 2D PGAA method may help in the determination of local concentrations. Two samples of the target material and a bigger deposit were analysed with the 2D method. In particular for the target material 2 samples were provided, the first one was cut from the target before the sputtering process, the second one was cut out from the same target but at the end of its life.

7.4.1 UMo target

From the target A20, a small slice was cut out before it was mounted in the sputtering device. The slice was 120 μm thick with a surface of 20 x 10 mm^2, the mass was 0.474 g. The neutron beam as described in chapter 5 was collimated down to 2 x 2 mm^2 with a combined LiF-ceramic plus LiF-polymer aperture. The scanning grid planned for the sample covered an area of 8 x 23 mm^2. The dimensions did not match completely all of the area of the sample, this was due mainly to the manual positioning of the sample and the lack of a direct imaging device. In any case, more than 90 % of the sample area was covered. Each point of the grid was measured for 4500 s under vacuum conditions.
In fig. 7.3, the 2D maps are shown. In the coloured map, the distribution of the counts for the 4060 keV line of U and for the 778 keV line of Mo are shown, respectively. In the black and white graphs, the local ratios of Mo and U are shown. The local concentration of Mo varies between 5.5 and 6.9 % and, accordingly, the local concentration of U between 93.1 and 94.5 %. In this case it is possible to see that the local mass ratio of the two elements is not constant, which means that the two main components are not homogeneously distributed. This differences can only be connected to the production phase of the target material.
An interesting outcome of these measurement was the detection of impurities like V, Fe, Pb, and Cu. In fig. 7.4, the 2D-maps of the counts obtained are shown. The impurities are non-

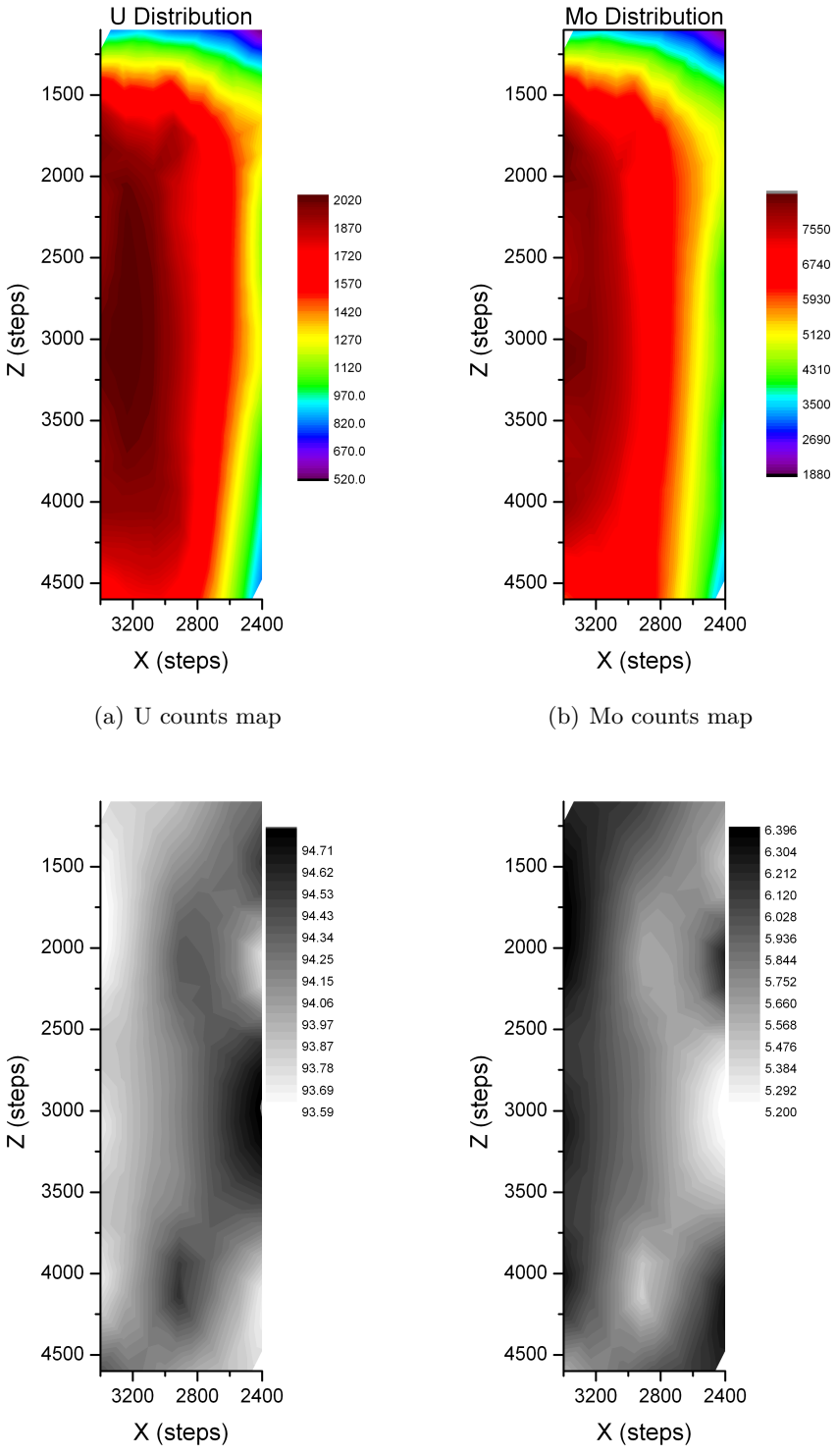

(a) U counts map

(b) Mo counts map

(c) Local concentration of U

(d) Local concentration of Mo

Figure 7.3: *U and Mo distribution in the fresh target.*

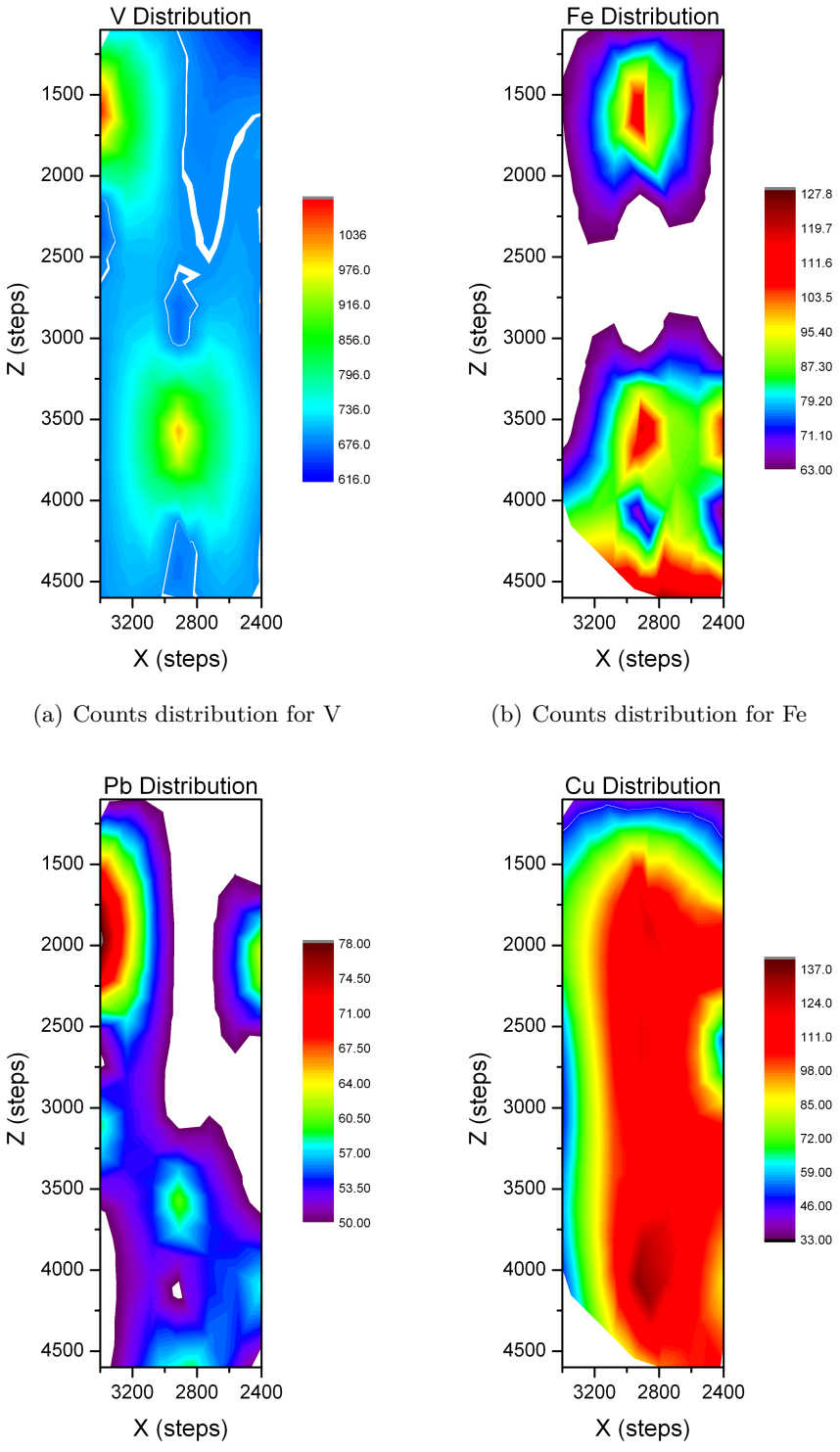

(a) Counts distribution for V

(b) Counts distribution for Fe

(c) Counts distribution for Pb

(d) Counts distribution for Cu

Figure 7.4: *Maps of the impurities found in the target material.*

homogeneously distributed in the material, the only exception is Cu. The reason of such a widespread presence of Cu can be explained only by Cu being a contaminant. The sample was cut out of the main target by using a wire saw whose wire was made of brass. From microscope measurements made on the same sample, a 5 μm brass layer was detected on both sides of the sample [63].
The second target sample that was analysed was coming from the exhausted A20 target. The thickness was about 500 μm and the mass was 1.086 g. The slice was taken in correspondence of the erosion region, the zone that faces the ion bombardment during the sputtering process. In fig. 7.5, the slice and the measured region are shown.

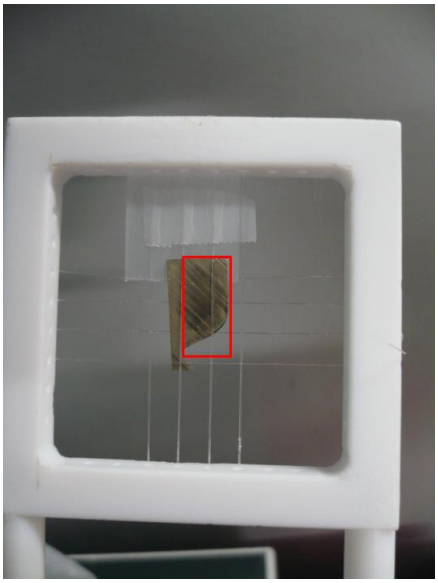

Figure 7.5: *Target after sputtering. The red zone is the scanned one.*

The scanned area was 8 x 20 mm^2 divided into 21 spectra, each acquired for 3600 s. Irradiation conditions were the same as for the previous measurement.

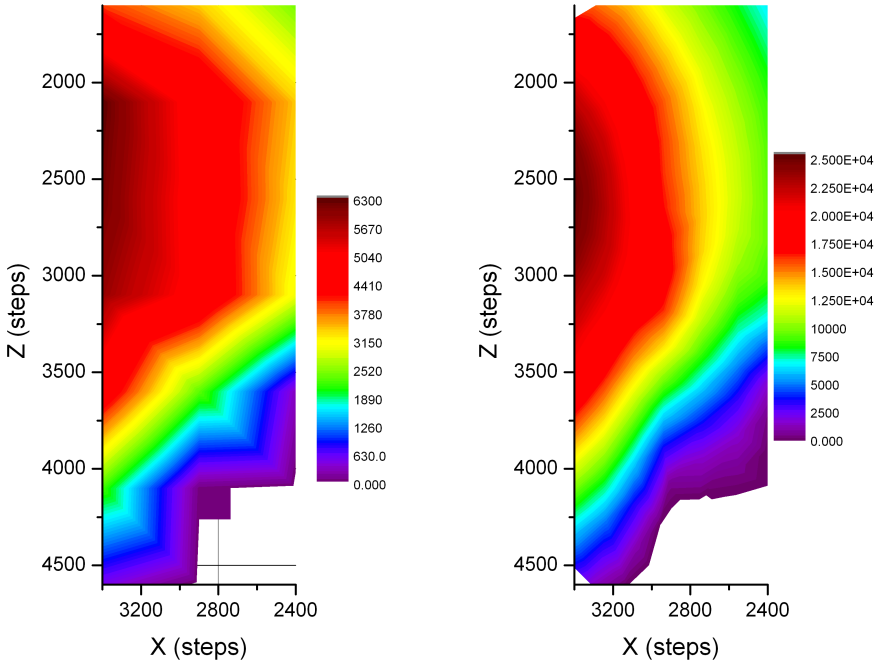

(a) Counts distribution of U

(b) Counts distribution of Mo

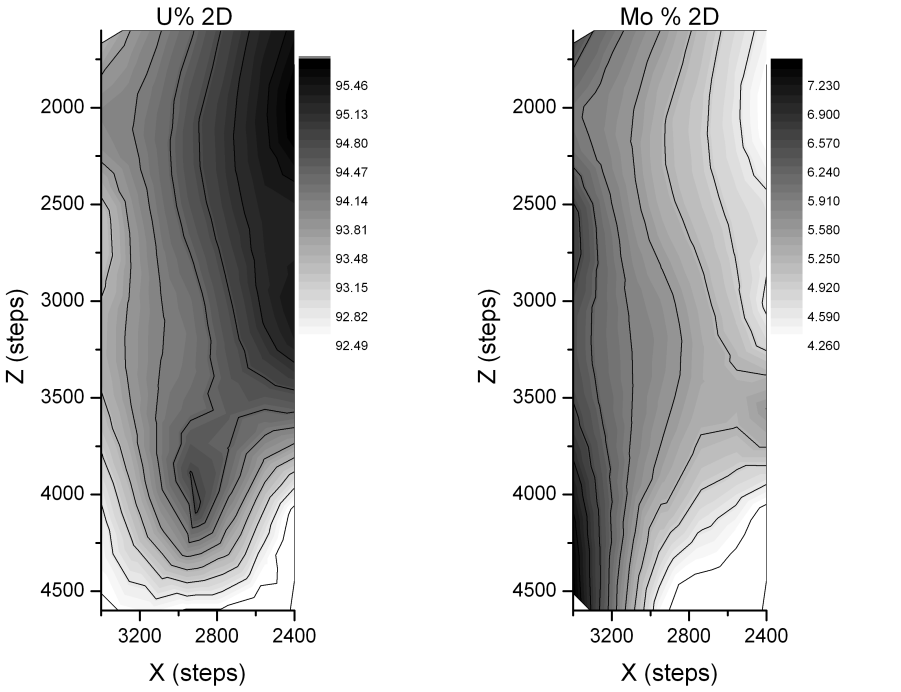

(c) Local concentration of U

(d) Local concentration of Mo

Figure 7.6: *2D maps of the counts for U and Mo and local concentration distribution of the target after sputtering.*

Also for this sample, 2D maps of the counts distribution for the U peak and the Mo peak were realized, see fig. 7.6. The Mo and U local concentration also in this case are not homogeneous. This time the Mo concentration varies in a wider range as for the fresh target. More precisely it varies between 4.3 and 7.5 %. From fig. 7.6(d) it is possible to notice that there is a gradient along the X direction. Moreover, the maximum Mo concentration is located in the erosion region of the sample. This effect can be a consequence of diffusion processes during sputtering, but also an inhomogeneity of Mo/U in the fresh material can be the cause of this gradient. Only two impurities were found: V and Fe. In fig. 7.7, the 2D maps are shown.

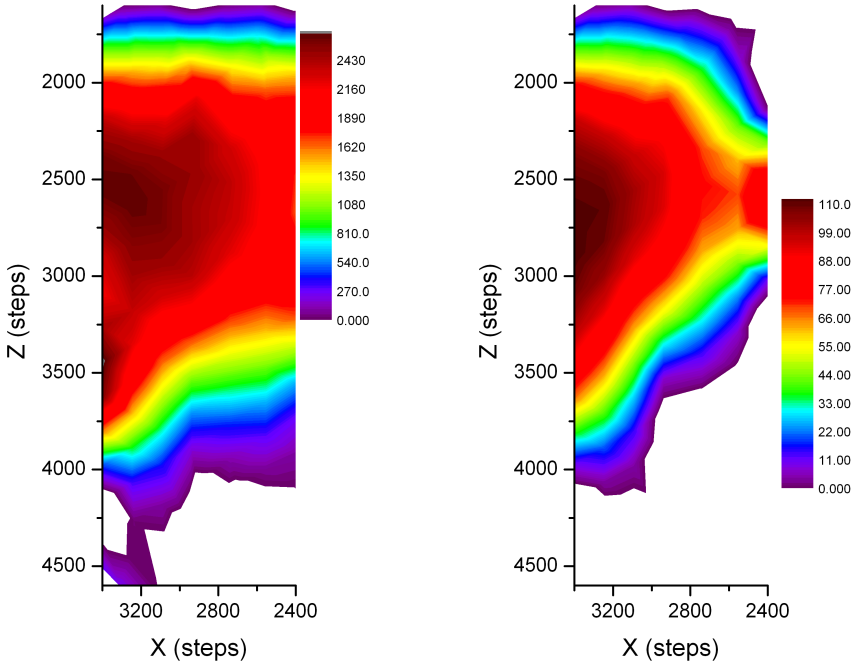

(a) Counts distribution V

(b) Counts distribution Fe

Figure 7.7: *Impurities found in the target after sputtering.*

As for Cu in the first sample, also in this case the distribution of the two elements is spread all over the sample surface. The cutting of the sample was performed with the same technique as before, but with a different wire. In this case, the wire was made of steel and diamond particles. V and Fe are typical elements used in steel alloys.

7.4.2 UMo foil

Besides the analysis of the target material before and after the sputtering process, a deposit of the target A20 was measured. The sample under study was a $10 \times 10\,\mathrm{cm}^2$ deposit of UMo alloy on a pure Zr substrate. The thickness of the UMo layer was $50\,\mu\mathrm{m}$ (1.99 g) sand the thickness of the substrate was $120\,\mu\mathrm{m}$. This particular substrate was chosen because Zr has a very low cross section (elemental capture cross section 0.19 b) in comparison with the cross section of the elements under study.
The whole layer was too big for the PGAA sample chamber, thus it was cut in 4 equal pieces each $5 \times 5\,\mathrm{cm}^2$. In principle, if the sample produced with the sputtering process is assumed to be

symmetrical, the information acquired by the analysis of one quarter can be projected over the entire original sample dimensions. In this case a full scan, of the sample was not possible due to the constraints posed by the beam-time schedule, therefore it was decided to scan only the two main lines of the foil. In fig. 7.8, the UMo layer and the analysis region are shown.

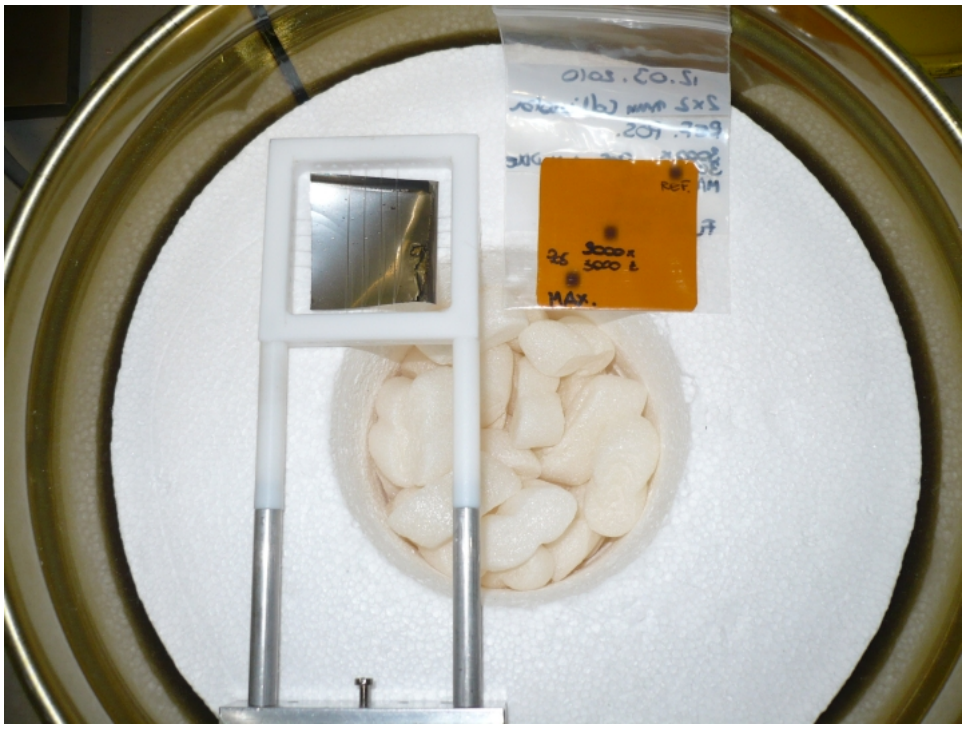

Figure 7.8: *Sputtered deposit on a Zr substrate. The red lines are the two lines analysed by 2D-PGAA.*

The two lines were scanned with 2.5 mm steps. The overall length of the scan lines was 34 mm due to the mechanical constraints of the 2D motor. The analysis of the 28 spectra (14 per direction) is shown in fig. 7.9.
The local concentration of Mo seems to decrease in the middle region of the foil for both lines. The concentration interval for the vertical scan line is 8.2 - 10.1 % and for the horizontal scan line 7.4 - 9.8 %. In the crossing point of the two lines the Mo concentration is comparable even though there is a small shift in the measuring positions. This effects can be connected with the preferential ejection of atoms on the substrate and it seems to be connected with the ring-shaped plasma, that creates the ion bombardment in the sputtering reactor.

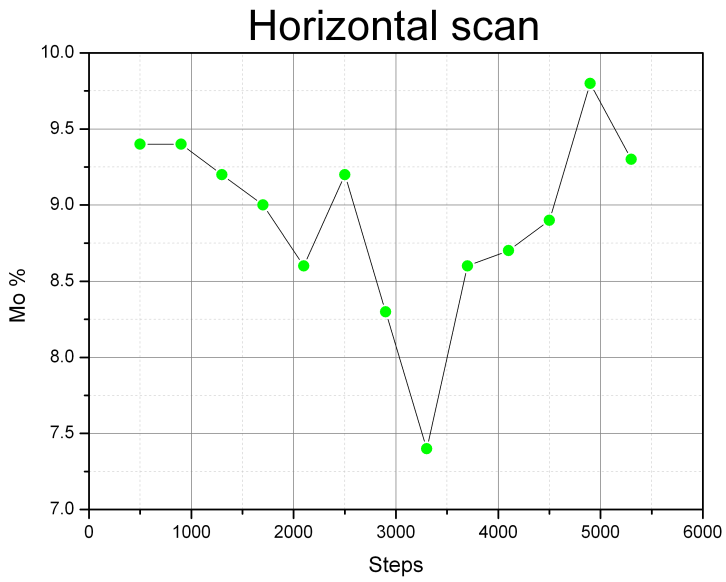

(a) Horizontal line

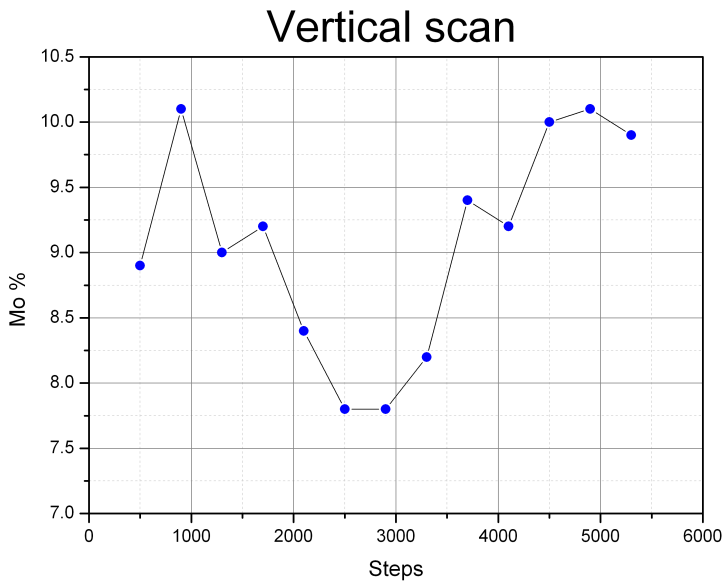

(b) Vertical line

Figure 7.9: *Mo local concentrations of a sputtered deposited film.*

7.5 Outlook

2D-PGAA is an effective tool for the study of local concentrations of U and Mo. Future developments of the 2D setup would be advisable, mainly the reduction of the neutron field. It would allow the investigation of a smaller region and a more precise analysis of the local concentrations. Systematic study of the sputtered deposits is advisable in order to understand how the sputtered elements are distributed on the substrate and if this distribution can be linked to particular parameters in the production phase. The 2D-mapping of a full size monolithic UMo fuel foils seems also feasible and promising. Especially to study their production phase.

CHAPTER 8

Conclusions and outlook

At the beginning of 2008, the new Prompt Gamma-ray Activation Analysis (PGAA) facility started operation at the Forschungs-Neutronenquelle Heinz Maier-Leibnitz (FRM II).

Formerly this instrument was located at the PSI in Switzerland and then moved to the new high flux research reactor in Garching. Thanks to the particular, elliptically shaped neutron guide (the last 6.9 m, moreover, the last 1.1 m, the so-called *elliptical nose*, is removable), the neutron flux available is considerably higher, moreover, the neutrons are focused in a spot that coincides with the sample position. The maximum thermal equivalent neutron flux reaches a value of $6.07 \cdot 10^{10}\,\mathrm{cm^{-2}\,s^{-1}}$ ($1.64 \cdot 10^{10}\,\mathrm{cm^{-2}\,s^{-1}}$ for cold neutrons). However, the intensity of the neutron flux is pretty flexible thanks to the installation of three neutron attenuator that allow the user to modulate the intensity of the neutron beam according to the samples and the desired results. The instrument is furbished with two gamma-ray spectrometers with an anti-Compton suppression system. The fine calibration of the two spectrometers is of vital importance for PGAA measurements. PGAA spectra are very complex with hundreds of gamma-ray energies, thus, for precise and reliable analytical results the precision of the energy calibration as well as the efficiency calibration are very important. Another important factor for a good quality measurements is the prompt-radiation background caused by construction materials hit by scattered neutrons. The main goal in the optimisation of the facility was the reduction of the background. The instrument has two main measuring configuration dictated by the presence of the removable 1.1 m long elliptical nose. At the beginning of the operation the total background count-rate with the elliptical nose was about 3000 cps with a reduced neutron flux of $1.71 \cdot 10^{9}\,\mathrm{cm^{-2}\,s^{-1}}$. Through the optimisation of the shielding materials and the introduction of a more efficient vacuum pump, the total background count-rate was reduced to only 192 cps for the same irradiation conditions. The same procedure was then carried out for the second setup (namely without the elliptical nose) and also in this case good improvement were obtained from 580 cps with a th. eq. neutron flux of $8.37 \cdot 10^{8}\,\mathrm{cm^{-2}\,s^{-1}}$ to 269 cps with a higher neutron intensity ($1.53 \cdot 10^{9}\,\mathrm{cm^{-2}\,s^{-1}}$).
The improvement of the background conditions improved the analytical sensitivity of the measurements. An estimation of the detection limits and of the analytical sensitivities for the most common elements was carried out and compared with the ones of other PGAA facilities around the world. From these preliminary data it is already possible to see the high potential of this new facility. Further measurements to experimentally determine the detection limits have to be carried out in the future.
To check the reliability of the analytical measurements, standard reference material were measured. The measurements were acquired in 2009 and after the main optimisation in 2010. From

the comparison of the results obtained in 2009 and 2010, it is possible to observe an overall improvement of the measurements sensitivity as well as more precise analytical results, e. g. lower uncertainties.

The PGAA measurements described in this work are underling some strong points of the facility. This technique has some *preferred elements*, like for example H, B, Gd, Cd, and Eu. In this work the attention is focused mainly on few elements which are particularly sensitive in PGAA measurements (non-$1/v$ nuclides Sm, Eu, Gd, and Cd).
The k_0-values for these elements were measured first. For non-$1/v$ nuclides the k_0-value are determined for each facility and they can only be used for that particular facility. This is mainly due to the low energy resonances in the cross section of these nuclides,combined with the neutron spectrum of the particular facility.
The k_0-values obtained for these elements were then compared with literature values and the effective g-factors were calculated using this comparison.
Following these measurements some samples, which contain these elements, were measured.
Thin films of europium oxide doped with Gd are a new material studied by the *Zentrum für elektronische Korrelation und Magnetismus* (Universität Augsburg) for the developement of new semiconductor materials for spintronics. The amount of the dopant Gd is derived from the growing process of the thin layer and a measurement of the real concentration in the sample is needed in order to calibrate the production of these thin films. Despite the difference between the amount of the sample (37 nm thick) and the amount of the substrate (about 200 mg of $YAlO_3$), the high neutron cross-section of Eu and Gd made measurements possible. The results obtained were then compared with those obtained by a different analytical method: X-ray Absorption Spectroscopy. The different concentrations of Gd in three differently doped samples were compared and the discrepancies between the two methods are in some cases huge. However, XAS measurement are less precise compared to PGAA measurements because the change of the background function creates an oscillation in the final concentration between 3 and 5 %.PGAA measurements are therefore more precise and reliable for the quantification of Gd in these particular thin films.

Cd is known to be a contaminant in trace amount in human tissues. The intake occurs following three main routes: inhalation, oral, and dermal. Cd is also recognized as a carcinogenic agent in human from different studies. The aim of these measurements was to determine a method for Cd determination in human tissues with PGAA. Thanks to the collaboration with the *Institut für Rechtsmedizin*, it was possible to determine Cd in some human tissues starting from samples belonging to the targets organs (liver and kidney) and samples taken from heart and lung.
The first measurements carried out were necessary to determine the feasibility, and to test some preparation techniques to decrease the amount of H, i. e. water. In particular drying and preconcentration procedure were tested. Preconcentration of sample was obtained by dissolution in concentrated nitric acid followed by evaporation. For each tissue three samples were prepared: one native sample, one dried sample and a preconcentrated one. As cross-check for all phases of the determination (preparation and Cd quantification through a calibration curve), samples taken from kidney of a male smoker subject were measured and analysed. Kidney is the major target organ for Cd accumulation and, in particular, smoker subjects have higher concentration due to the increased intake through cigarettes. Beside this cross-check measurements, samples from another patient were acquired and measured. In this case no record about the smoking habits were known. From the Cd concentration found in the kidney it was clear that he was not a smoker. The Cd concentration for the kidney of the smoker was 11.5 μg/g, while for the

second patient was only 2.0 μg/g.
A third measuring campaign was carried out and in kidney-, liver-, heart-, and lung samples from two patients. From the results in the kidney samples, it emerged that both were probably non-smokers.
Some problems were encountered during the quantification of Cd in native tissues. The Cd concentrations obtained with the calibration curve, in some cases, are not near the concentration obtained for the dried and preconcentrated samples. A possible explanation can be the thermalisation of neutrons in water-rich samples combined with the mismatching of the matrix between samples and calibration samples (that were water-deficient, more comparable with the dried and preconcentrated samples). The construction of a second rough calibration curve helped in the correction of the Cd concentration of the native samples.
The two methods used to reduce the amount of water inside the sample yield comparable results. The reduction of H inside the sample is effective with both preparation procedure. However, the drying procedure keeps the overall elemental composition unchanged and it is possible to treat quite easily multiple samples at once. The preconcentration method allows a very precise Cd measurement; the samples are homogenized and it is possible to analyse much more material. The drawback of this treatment are the long preparation times and a higher risk of contamination due to the extensive handling of the samples.

PGAA measurements are also very convenient for the analysis of archaeological objects. This technique can be considered non-destructive from a macroscopic point of view. Compared to other techniques, PGAA is a quick method to obtain information on the bulk composition.
A small set of ancient Greek coins, found in an excavation in the area of Lithochori, was analysed with PGAA. The information obtained on the coins was the metallurgical composition of the coins. This information helped archaeologists in the determination of the age of the coins as well as the provenance. The composition of the bronze of the coins was then compared with the one obtained by a different technique: Scanning Electron Microscope Energy Dispersive X-ray (SEM-EDX). As it can be seen the SEM-EDX technique is not able to detect all the elements being part of the bronze alloy mainly because it is a surface method,while PGAA yielded the bulk composition. Moreover, PGAA was able to detect also some trace elements like Ni inside the copper alloy. PGAA is also sensitive to Cl, that was found on 4 coins. This last element plays a role in the deterioration of bronze and it is extremely important to eliminate this element, for the good conservation of bronze artifacts.

Besides the standard PGAA measurements, a new analytical modality was developed. This new modality allows the analysis of spatial elemental distributions in two dimensions.
First tests were carried out with the setup developed for the Europen project *Ancient Charm*. The setup was developed for 3D imaging purposes on cultural heritage objects. For the 2D mapping only two stages of the setup were used (in air atmosphere) and as sample a small piece of the Allende meteoriten were used. This setup was also furbished with a neutron tomography system for a 3D visualization of the object. This part of the setup was used for a neutron radiography of the small meteorite for the positioning and for the planning of the 2D scan grid. Before the 2D scanning a standard PGAA measurement was carried out in order to obtain the composition of the meteorite and to establish major, minor and (when possible) trace element concentrations.
For the 2D PGAA measurements the neutron beam was collimated with a LiF-polymer aperture ($2\,\mathrm{x}\,2\,\mathrm{mm}^2$) and the scan grid was programmed. From the 15 spectra acquired, it was possible to

reconstruct the 2D-maps for the major components of the meteorite, i. e. Fe, Mg, and Si.
Thanks to the encouraging results, a more dedicated setup was subsequently built and tested. This second setup was made with a two stage motor only and the opportunity to evacuate the sample chamber in order to reduce the prompt background. Several tests were also made in order to improve the neutron collimation. Different materials for the aperture were tested and the best position for the collimation system was searched. This second task was necessary because of the shaping properties of the neutron guide. The elliptical tapering has the advantage of focusing the neutrons in a point but at the same time, after the focusing point, the neutron beam is divergent and this property is not helpful for a 2D scanning where the dimension of the collimator defines the spatial resolution of the method. In this case the most convenient position for the aperture was found to be near the neutron focal point. The setup was then calibrated and tested with a sample made of different materials with simple geometrical shapes.
The Allende meteorite was then remeasured with this second setup. The performance of the new setup was better than the former setup mainly due to the possibility to evacuate the sample chamber. The background reduction helped in the detection of some minor elements in the meteorite and made the reconstruction of 2D maps for Co, Sm, and Cl possible.
A general conclusion, which emerged from both setups, is the need of a correction for the amount of material in each measuring point. In the case of the meteorite the thickness is irregular thus the intensity of the count-rate of the element under study is dependent on the amount of the material irradiated (lots of material = high count-rate). The goal of the 2D measurements is to obtain the spatial distribution of the elements independently of the amount of the material irradiated. Therefore, in case of irregularly shaped samples a mass correction factor is necessary in order to obtain a more realistic distribution of the elements inside the object. For that purpose the tomography system can be helpful. From the 3D imaging reconstruction of the object a precise mass correction factor can be calculated.
In case of the meteorite, a rough mass correction factor was calculated from the manual measurements of the physical dimensions and then applied on the 2D distributions. For the major elements slight differences were observed while for the minor elements changes in the distribution were more noticeable.

The good performances of the new 2D setup was then applied to a second set of measurements. In this case depleted uranium-molybdenum alloy (UMo alloy) samples for nuclear fuel research were studied. This new material is currently under study thanks to its high uranium density. This property is actually of great importance for the switch from highly enriched uranium fuel elements used at the FRM II reactor to a medium enriched (50 %) uranium fuel element without changing the geometry of the reactor core. During this project, the sputtering process was investigated as a possible processing procedure for the production of UMo alloy. Because of side-effects of the sputtering process in case of multi-elemental alloys, like preferential sputtering and diffusion processes, the elemental distribution of U and Mo inside the deposited sample is of great interest. In this sense 2D PGAA is a suitable analytical technique.
First, PGAA measurements were carried out on the sputtering target material as well as thin deposits to check if the concentration of Mo inside the alloy remains unchanged. The nominal Mo concentration delivered by the producing company is 8.0 %. The Mo concentration found by PGAA measurements for the target material was of 7.3 % and for the deposit 9.2 %. The result of the UMo deposit was also compared with results obtained with Ion-coupled Plasma Optical Emission Spectroscopy (ICP-OES) and with Energy Dispersive X-ray (EDX) analysis. The results obtained with ICP-OES were found to be in agreement with the PGAA ones, while

those obtained with EDX, a surface method, were not. However, the discrepancies between Mo concentration in the target and in the deposit suggested the possibility of preferential sputtering effects, although the dimensions of the samples were too small to confirm this assumption.
The second step was to scan sections of the target material before and after the sputtering process and a larger UMo deposit with the 2D PGAA system. The 2D maps obtained for U and Mo for the target material before the sputtering process revealed a non-homogeneous distribution of the two elements. This can be a consequence of the production phase. Moreover, it was also possible to detect the distribution of some impurities in the material like V, Fe, and Pb and the contamination left by the cutting device, i. e. Cu (a brass wire was used). The target after the sputtering process was chosen taking into account the erosion zone of the ion bombardments. In this case in the 2D maps, a gradient in the concentration of Mo in correspondence of the erosion region was detected. This gradient cannot yet be explained; it can be a combination of diffusion effects as well as the inhomogeneity of the U/Mo distribution in the fresh material. As for the first target, the contamination left from the cutting device was detected again, in this case V and Fe (steel wire). The larger deposit, due to lack of beam time, was analysed only along two main directions, the vertical and the horizontal ones. From the analysis of the Mo concentration along the two directions it was possible to observe a pattern; the Mo concentration was lower in the middle region of the foil in both directions. This effect can be a due to the so-called preferential ejection process of the atoms on the substrate and, moreover, seems to be connected with the ring-shaped plasma, which creates the ion bombardment in the sputtering reactor.
In this case 2D PGAA demonstrates to be an effective tool for the study of local concentration of U and Mo.

The overall performance of the PGAA instrument at the research reactor FRM II was investigated in this work. The optimisation of the instrument carried out mainly in 2009, improved the analytical potential of the facility, however further improvements can be also carried out in the future. These efforts concern the reduction of the prompt radiation background. This development can be carried out in combination with high-count-rate applications. A new configuration of the HPGe detectors, like for example a higher sample-to-detector distance or a completely new geometry exploiting an inclined axes for the HPGe detector with respect to the neutron axes, can be applied. However this second suggestion signifies a huge effort and a complete rearrangement of the actual shielding materials as well as the experimental table.
A new system for the removal of the elliptical nose can also be taken into account. The development a new mechanism for the complete removal of the elliptical nose from the neutron guide can improve the efficiency of the shielding materials and solve some issues connected mainly to radiation safety regulations. Moreover, the study of an efficient shielding configuration behind the sample chamber and after the neutron stopper, for high flux applications, is highly advisable in order to start the use of the extremely high neutron flux available , which is not yet fully used because of radiation safety issues.
The main outlook is specially focused on the 2D-PGAA method. Further improvements should target the collimated neutron beam. The main problem encountered during the measurements was the high amount of fast neutrons produced by secondary reactions in the LiF-material of the aperture. Due to the high flux of the facility, fast neutrons are able to compromise the performance of the HPGe detector quite fast. A new configuration of the apertures, for example a series of apertures starting from the exit of the beam guide with an optimised choice of the materials can be studied in order to reduce the fast neutron production and at the same time describe more precisely the neutron beam, with the final goal to reduce the dimension of the

field, and thus to reach more accurate 2D elemental distributions.
Mass correction factors for the samples under study, derived from a neutron tomography image, have to be implemented in the analysis procedure for 2D PGAA measurements in order to obtain more realistic elemental distributions.
The two stage motor needs a new mechanic concept in order to reduce the weight of the whole system, and the reproducibility and stability of the positioning. Moreover, a lighter construction would allow to measure a broader set of samples. The measuring capacity of the actual system is limited by the weight of the samples themselves.
Last but not the least, a suitable analysis software should be developed for the handling of hundreds spectra that are easily produced with the 2D system. For 2D applications the analysis of the prompt spectra is simplified with respect to standard PGAA measurements. Usually the analysis is done with the help of few peaks (sometimes only with the major peak of the element under study, in the case of minor and trace elements) and thus the handling of the spectra with the common software used for standard PGAA requires a much larger amount of time.
In summary, the PGAA facility optimized during this thesis has the potential to become one of the best facilities in the world mainly due to the available extremely high neutron flux at FRM-II. The applications of PGAA are numerous and a few outstanding examples have been presented in this thesis.

APPENDIX A

Neutron self-shielding and gamma self-absorption

A.1 Neutron self-shielding

[15] When a sample contains a large amount of elements that have a high absorption cross section, the analytical sensitivity is affected by self-absorption within the sample itself. Neutron absorption decreases the analytical sensitivity and thus the measurements are compromised. Correction factors for this effect were calculated analytically for simple sample geometry in isotropic and parallel neutron fields.
In PGAA the neutron fields usually used are coming from neutron guides and therefore, are considered parallel. The self-shielding factor is defined as the ratio of the average neutron flux $\langle\phi\rangle$ through the sample to the incident flux ϕ_0 on the sample:

$$f = \langle\phi\rangle / \phi_0. \tag{A.1}$$

The magnitude of this factor is dependent on the size of the sample in terms of neutron free path and it is therefore proportional to the total macroscopic cross section Σ_t defined as the product of the microscopic cross section for neutron capture σ and the atomic density in the sample. According to the geometry of the samples and assuming that scattering effects are negligible, it is possible to calculate the correction factor for neutron self-shielding. In the following equations the correction factor f is expressed for simple sample geometry.
Slab geometry:

$$f = \frac{1 - e^{-x}}{x} \tag{A.2}$$

where $x = t\Sigma_t$ and t is the thickness.
Spherical geometry:

$$f = \frac{3}{x^3}\left[\frac{x^2}{2} - 1 + (1 + x)\, e^{-x}\right] \tag{A.3}$$

where $x = 2r\Sigma_t$ and r is the radius of the sphere.
Cylindrical geometry:

$$f = \frac{2}{x}\left[I_1(x) - L_1(x)\right] \tag{A.4}$$

where $x = 2r\Sigma_t$ and r is the radius of the cylinder and I_1 and L_1 are the modified Bessel function and the Struve function, respectively.

A.2 Gamma self-absorption

[18] Gamma self-absorption is dependent on the increasing thickness, density and atomic number (Z) of the sample.
Generally, starting from the attenuation law, it is possible to calculate the correction factor for gamma rays absorption a for radiation penetrating a uniform layer of thickness t in the normal direction:

$$a = 1 - (N/N_0) = 1 - e^{-\mu t} \tag{A.5}$$

where N is the number of photons emerging from the sample N_0 is the number of incident photons, μ is the attenuation coefficient and t is the thickness of the sample. In PGAA absorption occurs within the sample itself. In this case, assuming a planar sample of thickness t with an homogeneous distribution the number of emerging photons is calculated as:

$$N = \int_0^t N_0 e^{-\mu x} \frac{dx}{t} = N_0 \frac{1 - e^{-\mu t}}{\mu t}. \tag{A.6}$$

The self-absorption coefficient a_s becomes then:

$$a_s = 1 - \frac{1 - e^{-\mu t}}{\mu t}. \tag{A.7}$$

In case of a thin planar sample, when $\mu t << 1$ then

$$a_s = \frac{1}{2}\mu t. \tag{A.8}$$

In case the sample is spherical with a radius r and again $\mu t << 1$, a_s becomes:

$$a_s = \frac{3}{4}\mu r - \frac{2}{5}\mu^2 r^2. \tag{A.9}$$

Finally for a cylindrical source:

$$a_s = \frac{3}{8\pi}\mu r - \frac{1}{2}\mu^2 r^2. \tag{A.10}$$

APPENDIX B

Characterisation and optimisation of the new Prompt Gamma-ray Activation Analysis (PGAA) facility at FRMII

Characterisation and optimisation of the new Prompt Gamma-ray Activation Analysis (PGAA) facility at FRM II

Lea Canella [a,*], Petra Kudějová [b], Ralf Schulze [c], Andreas Türler [d] Jan Jolie [c]

[a] *Technische Universität München, Institut für Radiochemie, 85748 Garching, Germany*
[b] *Technische Universität München, Forschungs-Neutronenquelle Heinz Maier-Leibnitz, D-85748 Garching, Germany*
[c] *Universität zu Köln, Institut für Kernphysik, D-50937 Köln, Germany*
[d] *Paul Scherrer Institut, CH-5232 Villigen, Switzerland*

Abstract

At the research reactor Forschungs-Neutronenquelle Heinz Maier-Leibnitz (FRM II) a new Prompt Gamma-ray Activation Analysis (PGAA) facility was installed. The instrument was originally built and operating at the spallation source at the Paul Scherrer Institute in Switzerland. After a careful re-design in 2004-2006, the new PGAA instrument was ready for operation at FRM II.

In this paper the main characteristics and the current operation conditions of the facility are described. The neutron flux at the sample position can reach up $6.07 \cdot 10^{10}\,[cm^{-2}\,s^{-1}]$, thus the optimisation of some parameters, e.g. the beam background, was necessary in order to achieve a satisfactory analytical sensitivity for routine measurements.

Once the optimal conditions were reached, detection limits and sensitivities for some elements, like for example H, B, C, Si, or Pb, were calculated and compared with other PGAA facilities. A standard reference material was also measured in order to show the reliability of the analysis under different conditions at this instrument.

Key words: PGAA, FRM II, Cold neutrons, gamma spectrometry
PACS: 28.41.Rc, 82.80.Jp, 29.30.Kv, 29.25.Dz

1. Introduction

Prompt Gamma-ray Activation Analysis (PGAA) is a nuclear analytical technique that exploits the (n,γ)-reaction, i.e. neutron capture reaction, in order to determine the elemental composition of various samples. With this method major, minor and sometimes trace elements can be detected and quantified non-destructively.

With PGAA in principle, nearly all elements in the periodic table can be determined; in particular it is possible to quantify amounts of H, B, Na, Si, S, Cl, K, Ti, Mn, Co, Ni, Cd, Hg, Sm, Eu, and Gd. The detection limits for these elements are generally ranging from 1 ng/g for Gd up to 100 μg/g for Si. For all the other elements the detection limit is ranging from tenths of μg/g up to units of weight percent (e.g. for C, N, O, F, Sn, Pb and Bi) [1–3].

A new PGAA instrument has been built at the research reactor Forschungs-Neutronenquelle Heinz Maier-Leibnitz, FRM II, in Garching.

The fingerprint of this PGAA instrument is the design of the cold neutron beam guide. The total length of the beam guide is 52 m with a strong curvature (radius 390 m), in order to avoid a direct view of the reactor core. This way a very pure cold neutron spectrum (1.83 meV mean energy) is obtained free from hard gamma-rays and epithermal neutrons. Moreover, the last 6.9 m of the guide are elliptically tapered. This feature allows to focus the neutrons directly on the target with a gain in flux intensity.

The advantage of PGAA analysis with respect to other radioanalytical techniques are a rather easy handling of the samples and the quite fast measurements, i.e. in average between 30 minutes and 3 hours. In principle a complete PGAA measurements and analysis can be done within one day. Moreover an automated acquisition system of the setup allows to measure 6 samples in one run.

The first samples from external proposals analysed at the facility between 2008-2009 are coming from different science fields like geochemistry, material science, reactor physics, archeology and medicine. This shows a wide

* Corresponding author.
Address: Lichtenbergstr.1, D-85748 Garching, Germany;
Tel.: +49 (0)89 / 289-14758
Email address: lea.canella@frm2.tum.de (Lea Canella).

application for this kind of non-destructive analysis.

2. Instrument

The instrument was originally located at the neutron spallation source SINQ of the Paul Scherrer Institut (PSI) Villingen, Switzerland [4]. The main shielding materials (made of Pb, Cd, ^{6}LiF-polymer and ceramic) as well as the detectors configuration were kept, but some changes were applied especially around the end of the neutron guide. In fig.1 a sketch of the actual PGAA instrument at FRM II is shown.

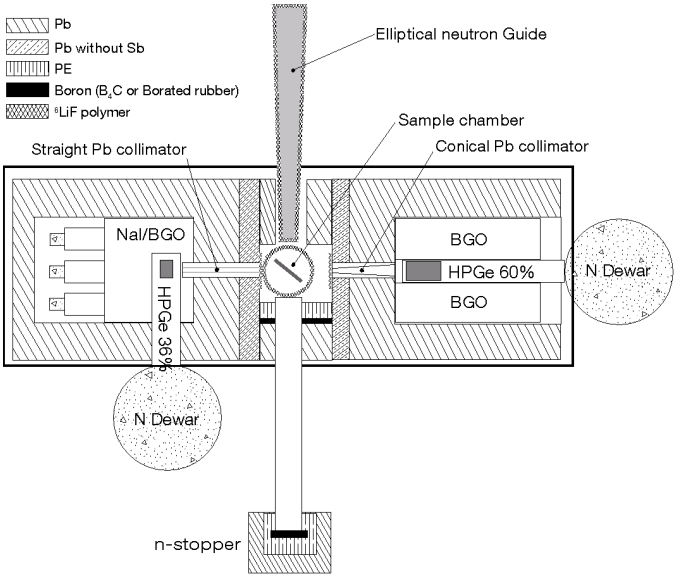

Fig. 1. Schematic sketch of the PGAA instrument at FRM II.

The neutron guide of the instrument looks at the cold source (liquid deuterium at 25 K) in the reactor tank [5]. This brings a white spectrum of cold neutrons with an average energy of 1.83 meV or in wavelength units 6.7 Å. The last 6.9 m of the neutron guide are straight and elliptically tapered and further divided in two units: a fixed 5.8 m long part and a removable one of 1.1 m, also called *elliptical nose*.
The position of the elliptical nose defines two different geometries for measurements. The first one, without the nose (Pos.1), has the neutron focus about 30 cm away from the end of the beam guide and the dimensions of the neutron field at the sample position are 34 mm x 50 mm. The maximum thermal equivalent neutron flux for this configuration is $2.42 \cdot 10^{10}\, cm^{-2}\, s^{-1}$ ($6.54 \cdot 10^{9}\, cm^{-2}\, s^{-1}$ real flux).
Using the elliptical nose (Pos.2) the dimensions of the neutron field are smaller (just 17 mm x 19 mm) but the maximal thermal equivalent neutron flux is increased about 2.5 times $6.07 \cdot 10^{10}\, cm^{-2}\, s^{-1}$ ($1.64 \cdot 10^{10}\, cm^{-2}\, s^{-1}$ real flux) [6,7]. In this second configuration the neutron focus was measured 9.5 cm away from the exit window. However, due to mechanical constraints, the sample can be only place at about 11 cm away from the exit window. The current flux values were measured at that position.

Table 1
Thermal equivalent neutron fluxes for the two setups and for some attenuator configurations. The uncertainty of the neutron flux value is 5%.

Setup	Attenuator	th. eq. Flux $[n\, cm^{-2}\, s^{-1}]$
No ell. nose	full beam	$2.42 \cdot 10^{10}$
No ell. nose	A1	$4.12 \cdot 10^{9}$
No ell. nose	A2	$4.40 \cdot 10^{9}$ [a]
No ell. nose	A3	$1.53 \cdot 10^{9}$
No ell. nose	A1 + A3	$7.32 \cdot 10^{8}$
No ell. nose	A2 + A3	$8.34 \cdot 10^{8}$
No ell. nose	A1 + A2 + A3	$3.61 \cdot 10^{8}$
Ell.Nose	full beam	$6.07 \cdot 10^{10}$
Ell.Nose	A1	$7.18 \cdot 10^{9}$
Ell.Nose	A2	$7.66 \cdot 10^{9}$
Ell.Nose	A3	$2.41 \cdot 10^{9}$
Ell.Nose	A1 + A3	$1.71 \cdot 10^{9}$
Ell.Nose	A2 + A3	$1.92 \cdot 10^{9}$
Ell.Nose	A1 + A2 + A3	$7.84 \cdot 10^{8}$

[a] Due to technical problems not measured. The given value is estimated.

Three attenuators (A1, A2 and A3) are installed about 20 m upstream of the sample position to have a more adjustable neutron flux. These attenuators are made of borated aluminum and are not in the direct view of the sample position, thus no additional gamma-ray background is created. Since two of them are made out of slits (comb-like horizontally for A1 and vertically for A2) and the third one has has round holes, the neutron spectrum is unchanged. The use of those attenuators and their combinations allow an high optimisation of the irradiation conditions. The 3 attenuators have a neutron transmission of about 17 % (A1), 18 % (A2) and 6 % (A3) for the setup without the elliptical nose (Pos.1). In table 1 the flux intensities for the two setups and for various attenuator configurations are given.

2.1. *Detection system*

For the gamma-ray spectra acquisition, two standard Compton-suppressed gamma spectrometer are in use:
– Det.1: HPGe n-type detector with a relative efficiency of 60% (ORTEC poptop) inserted in an annulus of BGO scintillators (coaxial geometry, in fig.1 on the right);

– Det.2: HPGe n-type detector with a relative efficiency of 36% (Canberra) surrounded by a NaI(Tl)/BGO scintillation system (perpendicular geometry in fig.1 on the left).

Standard NIM (Nuclear Instrument Module) modules are used for the electronic instrumentation. The analysis of the shaped detector signals is made by an integrated ADC-MCA system (16k channels) developed at the Institut für Kernphysik, Universität zu Köln.

2.2. *Data analysis*

For the evaluation of the spectra and the calibration of the spectrometer (efficiency curve and non-linearity), the software Hypermet PC is in use [8,9]. In fig.2 the efficiency curve for typical energy range for PGAA (from about 70 keV up to 11 MeV) is presented. The low energy region

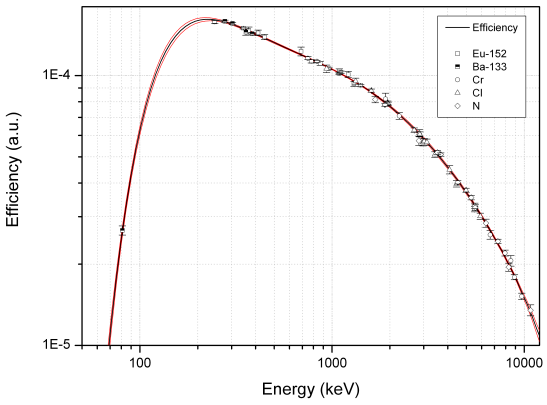

Fig. 2. Efficiency curve for the coaxial detector (60%).

of the efficiency curve was obtained with the radioactive source ^{133}Ba and the calibrated radioactive source ^{152}Eu. For the high energy range, neutron capture reactions on N, Cl and Cr were used.

For the determination of the elemental composition of samples an Excel macro and Excel sheet package called ProSpeRo (Prompt gamma Spectrum Rover) is used [10].

2.3. *Shieldings*

The main shieldings of the instrument remained, except for minor changes, the same as at PSI and are described in detail in ref.[4]. For high neutron-flux PGAA measurements the choice of the shielding materials is a very critical task and it should be a compromise between the need to keep the beam background as low as possible and to fulfill radiation safety rules.

Few changes were made for the coaxial spectrometer shieldings (see fig. 1). The Pb wall in front of the spectrometer was increased of 15 cm instead of 10 cm and the sample-detector distance was increased by about 5 cm to about 35 cm.

Removable lead shielding in U-form were built for the removable elliptical nose. They are made of 10 cm thick lead covered inside with Borated rubber. A sketch of the whole instrument, including the removable shielding *shells* for the elliptical nose is shown in fig.3.

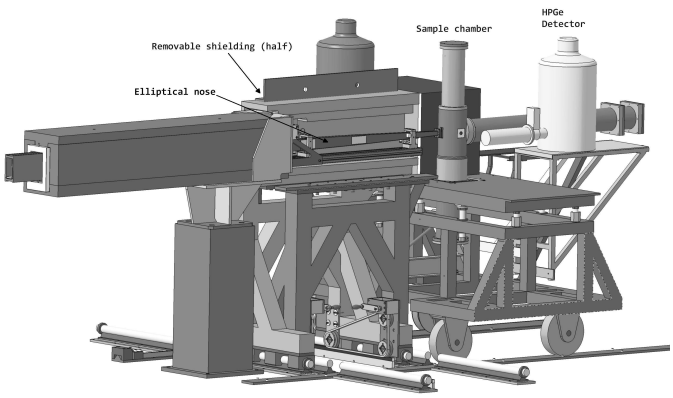

Fig. 3. 3D-CAD-drawing of the PGAA instrument (Pos.2). The removable shieldings for the elliptical nose are shown. Rails allow to shift the shieldings to the sides when the nose is not in use. The elliptical nose can be then tilted to a vertical position (Pos.1).

Due to the higher neutron flux than at PSI, the shieldings around the sample chamber had to be improved. A polyethylene wall was added between the sample chamber and the Pb wall with the rear surface cover by borated gum, in order to slow down and catch the fast neutrons produced by a secondary reaction in the ^{6}Li shielding materials. A polyethylene wall covered on one side with borated rubber and a 10 cm thick Pb wall were added behind the sample chamber (see fig.1).

3. Measurements

3.1. *Background*

Because PGAA measurements are done on-line, i.e. when the neutron beam is open, the acquired gamma-ray spectra are heavily influenced by neutron reactions that take place in the surrounding materials. A very low prompt gamma-ray background is necessary in order to achieve an high analytical sensitivity for the real samples.

A common source of background for both setups (i.e. with or without the elliptical nose) is air, mainly due to the high amount of N (ca. 78 %). To minimize this contribution nearly all measurements are carried out under vacuum conditions.

Due to the higher neutron flux, the optimisation of the total background count-rate for this facility was not a trivial task. At the beginning of the operation of the facility in 2008, the beam background was measured for both setups, Pos.1 and Pos.2.

At first, for Pos.1 a satisfactory result was achieved in collaboration with the Budapest PGAA group (580 cps for a

flux of $8.37 \cdot 10^9$ n/cm^2 s th.eq., no attenuators in beam). In this case a temporary boron carbide (B_4C) aperture was placed at the end of the neutron guide. The incoming beam was cut significantly in geometry (to about 20 mm x 16 mm) as well as in intensity.
The total count-rate for the setup for Pos.2 was not so encouraging; it was around 3000 cps with 2 attenuators in beam (A1+A3, for the flux value see table 1). Efforts to reduce the background in this configuration were then carried out extensively.
In table 2 the improvement of the total count-rate for background with the elliptical nose setup is presented. The configurations of attenuators chosen (A1+A3 and A2+A3) are the most common for standard PGAA measurements.

Table 2
Total count-rate for PGAA background measured with the elliptical nose. Measurements were carried out for 54 000 s, if not specified otherwise. The number of attenuators in beam is an indirect indication for the neutron flux (see table 1).

Date	Count-rate [cps]	Attenuators	Comment
04/2008	3 220	A1 + A3	Short measurement 1800s
05/2008	607	A1 + A3	Short meas., Pb shielding around elliptical nose
05/2008	325	A1 + A3	Short meas., Pb+Li shielding around elliptical nose
06/2008	339	A2 + A3	New detector shieldings
01/2009	455	A2 + A3	New Pb collimator in front of HPGe detector
04/2009	314	A2 + A3	^{6}LiF-polymer conical flight tube @ end of the n-guide
01/2010	192	A2 + A3	New vacuum pump, 0.9 mbar instead of 15 mbar

The measuring position with the elliptical nose is about 11 cm away from the end of the guide itself, thus the whole system is quite near the sample chamber, that has an inner diameter of 15 cm. From the analysis of the background spectra it was possible to identify the main sources of background: Si and Na. These two elements are the main components of the neutron guide glasses. In order to reduce the contribution of the glasses, an extra Pb shielding was built around the end of the elliptical nose. The result was a reduction in the count-rate from 3000 cps to 600 cps.
An extra ^{6}LiF-polymer tube was added between the exit window of the n-guide and the sample chamber's entrance window. This shielding cuts away most of the scattered and divergent neutrons along the path of the neutron beam. This detail brought a further improvement in the background count-rate to 325 cps.
In January 2009 the original Pb collimator (with 10 mm in diameter) in front of the 60% detector was exchanged with a conical one (entrance diameter 10 mm, exit diameter 40 mm). This change optimises the use of the larger Ge crystal of this detector (60% rel. eff.) with respect the one used in the original setup at PSI. In this case the background count-rate was slightly increased from 339 cps to 455 cps.
An optimisation of the ^{6}LiF-polymer tube, in April 2009, between the end of the n-guide and the sample chamber brought again a reduction in the background count-rate (314 cps). The purpose was to reduce the shadow due to divergent neutrons around the useful neutron area of the beam. The optimal shape of the new tube chosen was a linearly tapered shape. Dimensions were calculated based on the images of the neutron beam at the sample position.
The exchange of the vacuum pump in January 2010, brought a significant improvement of the vacuum conditions (from 10 mbar to less than 1 mbar) and of the background count-rate to only 192 cps.
The improvement brought from the introduction of the optimised ^{6}LiF-polymer tube for Pos.2, suggested to use the same solution also for Pos.1 instead of the boron carbide aperture. In this case the neutron flux is not drastically reduced as with the boron carbide aperture and the background count-rate of 269 cps was achieved with the attenuator 3 in beam (i.e. with a thermal equivalent neutron flux of $1.53 \cdot 10^9\, cm^{-2}\, s^{-1}$).
The main difference in the background count-rate with and without the elliptical nose is due to the dimension of the neutron field. For Pos.1 the slightly higher count-rate is given by the irradiation of a larger amount of fluorinated ethylene propylene (FEP), the material used for the samples holder and to pack the samples.
In table 3 the main elements that affect the background are listed. The values given in table 3 are calculated as a ratio, thus they are not absolute masses (the latter are contributing to the background count-rate). Nevertheless, it is possible to notice how the neutron guide materials (especially Si and Na) have a higher contribution to the background when the elliptical nose is used.

Table 3
Elements found in the background spectra without and with the elliptical nose.

Element	Pos.1 (A3) μg	Pos.2 (A2+A3) μg
H	$2.80(3) \cdot 10^{-3}$	$2.34(7) \cdot 10^{-4}$
B	$1.67(2) \cdot 10^{-5}$	–
C	11.3(5)	0.33(1)
F	34.9(21)	1.03(6)
Na	$5.0(9) \cdot 10^{-3}$	$1.15(3) \cdot 10^{-2}$
Al	$4.42(10) \cdot 10^{-2}$	$5.1(2) \cdot 10^{-3}$
Si	$4.4(8) \cdot 10^{-3}$	$3.04(9) \cdot 10^{-2}$
Ca	$1.7(2) \cdot 10^{-3}$	$3.28(16) \cdot 10^{-3}$
Fe	$4.31(17) \cdot 10^{-3}$	$7.1(6) \cdot 10^{-4}$
Pb	$6.6(4) \cdot 10^{-2}$	$8.8(11) \cdot 10^{-3}$

3.2. *Analytical sensitivity and detection limits*

Every PGAA facility has different sensitivities to elements. This is mainly due to the counting efficiency and the partial gamma-ray production cross sections for the energies of the gamma lines and the neutron flux. The analytical sensitivity can be derived as follow:

$$s = \frac{\rho_\gamma}{m} = \frac{N_a}{M}\,\sigma_{\gamma,0}\,\phi_0\,\epsilon\,(E) \tag{1}$$

where m is the mass of the element under analysis, ρ_γ is the recorded count-rate, $\sigma_{\gamma,0}$is the partial gamma-ray production cross section, ϕ_0 the thermal equivalent neutron flux and $\epsilon\,(E)$ is the peak counting efficiency. In more practical cases this value can be measured using a standard with different concentrations. The analytical sensitivity is thus given by the slope of the linear regression of the variation of the count-rate (in cps) versus the net elemental mass (in mg) of the standard [4].
Detection limits (DLs) are generally estimated based on the background spectrum. Commonly DLs are calculated as three times the standard deviation of the number of background counts in the corresponding position of the considered peak (N_{bgr}). The DL in mass units is then obtained with the following equation:

$$DL = \frac{3\sqrt{N_{bgr}}}{s\,t_m} \tag{2}$$

where s is the analytical sensitivity defined in eq.1 and t_m is the duration of the background measurement [1,11].
Actually, it was not yet possible to carry out a systematic measurements of the analytical sensitivity for the major elements measured at this PGAA instrument. Therefore an estimation was done using eq.1 and the measured neutron flux for standard PGAA measurements, see table 4.
DLs for some elements were also calculated using a background spectrum with an empty FEP bag taken for 54 000 s.

The DLs given in table 4 are just a qualitative indication on "how well" an element can be detected. For real samples there is always the influence of the main elements of the sample (sample matrix) that will modify the background for the minor or trace elements, thus the detection limit.

3.3. *Analytical measurements*

For a good analytical measurement the gamma spectrometer should be well calibrated. The calibration of the two detectors was made following the procedure described in ref. [15]. In order to check the reliability of the facility a standard reference material (SRM) was measured in 2010 at both newly optimised positions. The SRM chosen was the number 1646a: Estuarine Sediment, provided by NIST (National Institute of Standards and Technology). A measurement was already performed at the beginning of 2009 with the elliptical nose (A2+A3 attenuators), the background count-rate was 455 cps (see table 2) and the acquisition time was 4600 s. The measurements carried out in 2010 were taken for 10800 s, with a total background count-rate of 192 cps for Pos.2 (A2+A3 attenuators) and 269 cps for Pos.1 (A3 attenuator in beam). The results are presented in table 5.

Already in 2009, the instrument demonstrated a good performance. With the improvement of the background conditions in 2010, it was also possible to detect some trace elements like: V, Mn, Cd, Sm and Gd. Moreover, the uncertainties were lowered compared to the measurement carried out in 2009 (this is quite evident in the determination of Cl). In the first case, uncertainties were between $3-5\,\%$ while in 2010 the maximum uncertainty was $3\,\%$, of course also thanks to the prolonged measuring time.
Aside general considerations, there are few differences in the determination of Na between the two different setups. In particular Na is overestimated without the elliptical nose. A possible explanation can be the difficulty to estimate precisely the amount of Na in the background spectrum.
Concerning the determination of trace elements, it is shown that for elements like Sm and Gd (that have an high capture cross section), the results are in a good agreement, while for Mn and V there are some discrepancies. In particular the determination of Mn with the elliptical nose is not in agreement with the certified value. An explanation can be the higher background in the low energy region due to the high flux achieved in Pos.2 that made the determination for this element more difficult. On the other hand thanks to this property the determination of Cd was possible.

4. Conclusion

In this paper the new PGAA facility installed at the research reactor FRM II, Garching, was described. The available neutron flux at the PGAA station is very flexible (from $3.61 \cdot 10^8$ up to $6.07 \cdot 10^{10}$ $[cm^{-2}\,s^{-1}]$ thermal equivalent), thanks to two different measuring setups and three neutron attenuators that help the optimisation of the irradiation conditions. The high intensity of the neutron flux contributes positively on the measurements (shorter measuring times and lower detection limits) but in the same time introduces a number of challenges concerning mainly the beam background (higher count-rate and more interferences from the shielding and construction materials).
The main shielding materials were kept as in the original configuration at PSI. A number of modifications were done in order to optimise important parameters such as the beam background characteristics and intensity. Detection limits and sensitivities for some elements, e.g. like H, B or Pb, were calculated for this facility to give some informative values , however a more systematic measurements of the sensitivities has to be carried out. Standard reference material, Estuarine sediment 1646a, was measured at Pos.1 and Pos. 2, the data were analysed and compared with the

Table 4
Detection limits for few elements and comparison with other PGAA facilities.[1,12–14]

El.	Energy [keV]	Sensitivity [cps/mg]	DL FRM II [μg]	DL PSI [μg]	DL JRR-3M [μg]	DL Budapest [μg]	DL NIST [μg]
H	2 223.2	29.93	0.11	0.69	1.0	0.3	3
B	477.6	10 687.05	0.0018	0.0039	0.0023	0.0015	0.02
N	1 884.9	0.10	40.5	235	95	100	1100
N	5 269.2	0.08	11.3			60	
Si	3 539.0	0.29	14.9	63		24	400
S	841.0	1.50	7.48	23.8	9.4	10	75
S	5 420.6	0.44	1.73			10	
Cl	1 951.1	17.31	0.19			0.6	
K	770.3	3.19	2.00	7.8		4	44
Ca	1 942.7	0.86	4.89	26.7		11	140
Ti	1 381.7	12.17	0.29	2.05		0.9	10
Fe	352.3	0.91	11.7		16	20	140
Fe	7 631.1	0.36	1.98	28		9	
Ni	465.0	2.34	4.15	12	5.1	7	70
Ni	8 998.4	0.62	0.65			4	
Cd	558.3	2548.66	0.0028	0.0142	0.0070	0.006	0.05
Sm	334.0	5802.65	0.0019	0.0060	0.0030	0.003	0.03
Gd	182.0	10 131.11	0.0011	0.0035	0.0047	0.0022	0.015
Hg	368.0	201.92	0.051	0.143	0.045	0.08	0.44
Pb	7 367.8	0.02	28.1	330		150	2 600

Table 5
Standard Reference material #1646a: Estuarine sediment. Comparison between different setups (ell. stands for elliptical nose) and with the measurement made at PSI. If not specified all the values are in weight percent.

El.	NIST	Ell.2009	Ell.2010	No ell.2010	PSI[2]
H	–	0.209(2)	0.186(3)	0.194(3)	–
B *ppm*	–	39.5(5)	45.1(6)	43.6(6)	41.8(11)
Na	0.741(17)	0.69(7)	0.690(21)	0.99(3)	–
Al	2.297(18)	2.18(9)	2.41(6)	2.17(6)	2.14(5)
Si	40.00(16)	40.1(6)	40.1(8)	40.2(8)	40.00
S	0.352(4)	0.37(2)	0.316(12)	0.312(11)	0.347(10)
Cl	–	0.66(22)	0.648(17)	0.615(17)	0.636(8)
K	0.864(16)	0.881(19)	0.87(3)	0.85(3)	0.84(2)
Ca	0.52(2)	0.65(3)	0.61(5)	0.615(25)	0.516(4)
Ti	0.456(21)	0.476(15)	0.494(12)	0.448(14)	0.473(10)
V *ppm*	44.8(8)	–	59.4(77)	64.0(64)	–
Mn *ppm*	234.5(28)	–	184.7(61)	232(12)	–
Fe	2.01(4)	2.00(5)	1.97(7)	1.90(6)	1.86(48)
Cd *ppm*	0.148(7)	–	0.12(5)	–	0.150(23)
Sm *ppm*	–	–	2.05(5)	2.11(5)	2.45(11)
Gd *ppm*	–	2.0(2)	2.4(1)	2.4(1)	2.64(8)

certified NIST values as well as the former results obtained at PSI.

Acknowledgment

Financial support of the Ancient Charm project by the European Community "New and Emerging Science and Technology" Contract No 15311 is acknowledged.The authors want also to acknowledge the excellent collaboration with the PGAA group at the Budapest Neutron Center.

References

[1] G. L. Molnár (Ed.), Handbook of Prompt Gamma Activation Analysis, Kluwer Academic Publishers, 2004.

[2] S. Baecheler, P. Kudějová, J. Jolie, J.-L. Schenker, *The k0 method in cold-neutron prompt gamma activation analysis*, J. Radioanal. Nucl. Chem. 256 (2003) 239–245.

[3] Molnár, T., Belgya, T., Dabolczi, L., Fazekas, B., Révay, Zs., Veres, A., Bikit, I., Kiss, Z., Östör, J., The new prompt gamma-activation analysis facility at Budapest, J. Radioanal. Nucl. Chem. 215 (1997) 111–115.

[4] M. Crittin, J. Kern, J.-L. Schenker, The new prompt gamma-ray activation facility at the paul scherrer institute, switzerland, Nucl. Instrum. Methods Phys. Res., Sect. A 449 (2000) 221–236.

[5] Forschungsneutronenquelle Heinz Maier-Leibnitz (FRMII). URL `http://www.frm2.tum.de/en/technik/secondary-sources/cold-source/index.html`

[6] Forschungsneutronenquelle Heinz Maier-Leibnitz (FRMII). URL `http://frm2.tum.de/pgaa`

[7] P. Kudějová, G. Meierhofer, K. Zeitelhack, J. Jolie, R. Schulze, A. Türler, T. Materna, *The new PGAA and PGAI facility at the research reactor FRM II in Garching near Munich*, J. Radioanal. Nucl. Chem. 278.

[8] Hypermet PC. URL `http://www.iki.kfki.hu/nuclear/hypc/index_en.shtml`

[9] Révay, Zs., Belgya, T., Molnár, T., Application of Hypermet-PC in PGAA, J. Radioanal. Nucl. Chem. 265 (2005) 261–265.

[10] Révay, Zs., Determining Elemental Composition Using Prompt Gamma Activation Analysis, Anal. Chem. 81 (2009) 6851–6859.

[11] K. Debertin, R. G. Helmer, Gamma- and X-ray spectrometry with semiconductor detectors, Elsevier Science Publishers B. V., 1988.

[12] P. Kudějová, T. Materna, J. Jolie, A. Türler, P. Wilk, S. Baechler, Zs. Kasztovszky, Zs. Révay, T. Belgya, On the construction of a new instrument for cold-neutron prompt gamma-ray activation analysis at the FRM-II, J. Radioanal. Nucl. Chem. 265 (2005) 221–227.

[13] C. Yonezawa, A. K. H. Wood, M. Hoshi, Y. Ito, E. Tachikawa, The characteristics of the prompt gamma-ray analyzing system at the neutron beam guides of JRR-3M, Nucl. Instrum. Methods Phys. Res., Sect. A 329 (1993) 207–216.

[14] R. L. Paul, R. M. Lindstrom, A. E. Heald, Cold neutron prompt gamma-ray activation analysis at NIST - Recent developments, J. Radioanal. Nucl. Chem. 215 (1997) 63–68.

[15] Molnár, T., Révay, Zs., Belgya, T., Wide energy range efficiency calibration method for Ge detectors, Nucl. Instrum. Methods Phys. Res., Sect. A 489 (2002) 140–159.

List of Figures

List of Tables

Bibliography

[1] E. by Zeev B. Alfassi, ed., *Non-destructive elemental analysis*. Blackwell Science Ltd., 2001.

[2] "Forschungsneutronenquelle Heinz Maier-Leibnitz (FRMII). http://frm2.tum.de, August 2010.."

[3] M. D. Glascock, "Overview of Neutron Activation Analysis."

[4] W. D. Ehmann and D. E. Vance, *Radiochemistry and Nuclear Methods of Analysis*. John Wiley & Sons, 1991.

[5] N. Eby, "Instrumental Neutron Activation Analysis (INAA)," November 2010.

[6] J.-M. Mermet, M. Otto, M. Valcarel, R. A. Kellner, and H. M. Widmer, eds., *Analytical chemistry*. WILEY-VCH, 2004.

[7] G. F. Knoll, *Radiation detection and measurements*. John Wiley & Sons, 2000.

[8] J. Chadwick, "Letter to the Editor: Possible Existence of a Neutron," *Nature*, vol. 129, p. 312, 1932.

[9] D. E. Lea, "Combination of Proton and Neutron," *Nature*, vol. 133, p. 24, 1934.

[10] E. Fermi, E. Amaldi, O. D'Agostino, F. Rasetti, and E. Segré, "Artificial Radioactivity produced by Neutron Bombardment," in *Proceedings or the Royal Society of Londos. Series A, Containing papers of a Mathematical and Physical Character*, vol. 146, pp. 483–500, 1934.

[11] T. L. Isenhour and G. H. Morrison, "Modulation Technique for Neutron Capture Gamma Ray Measurements in Activation Analysis," *Anal. Chem.*, vol. 38, pp. 162–167, 1966.

[12] T. L. Isenhour and G. H. Morrison, "Determination of Boron by Thermal Neutron Activation Analysis Using a Modulation Technique," *Anal. Chem.*, vol. 38, pp. 167–169, 1966.

[13] R. Henkelmann, "Low Energy Gamma Rays from Thermal Neutron Capture," *Z. Physik*, vol. 258, pp. 315–320, 1973.

[14] R. Henkelmann and H. -J. Born, "Analitycal use of neutron-capture gamma-rays," *J. Radioanal. Nucl. Chem.*, vol. 16, pp. 473–481, 1973.

[15] G. L. Molnár, ed., *Handbook of Prompt Gamma Activation Analysis*. Kluwer Academic Publishers, 2004.

[16] R. L. Paul and R. M. Lindstrom, "Prompt gamma-ray activation analysis: Fundamentals and applications," *J. Radioanal. Nucl. Chem.*, vol. 243, pp. 181–189, 2000.

[17] Krane K. S., *Introductory Nuclear Physics.* John Wiley & Sons, 1988.

[18] K. Debertin and R. G. Helmer, *Gamma- and X-ray spectrometry with semiconductor detectors.* Elsevier Science Publishers B. V., 1988.

[19] E. Brooks Shera and D. W. Hafemeister, "Study of the ^{59}Co(n,γ)^{60}Co Reaction and the Level Structure of ^{60}Co," *Phys. Rev.*, vol. 150, pp. 894 – 905, 1966.

[20] C. Yonezawa, "Multi-Element Determination by a Cold Neutron-Induced Prompt Gamma-Ray Analysis," *Anal. Sci.*, vol. 12, pp. 605–613, 1996.

[21] Currie L. A., "Limits for Qualitative Detection and Quantitative Determination," *Anal. Chem.*, vol. 40, pp. 586–593, 1968.

[22] M. Crittrin, J. Kern, and J.-L. Schenker, "The new prompt gamma-ray activation facility at the Paul Scherrer Institute, Switzerland," *Nucl. Instrum. Methods Phys. Res., Sect. A*, vol. 449, pp. 221–236, 2000.

[23] P. Kudějová, T. Materna, J. Jolie, A. Türler, P. Wilk, S. Baechler, Zs. Kasztovszky, Zs. Révay, and T. Belgya, "On the construction of a new instrument for cold-neutron prompt gamma-ray activation analysis at the FRM-II," *J. Radioanal. Nucl. Chem.*, vol. 265, pp. 221–227, 2005.

[24] P. Kudějová, G. Meierhofer, K. Zeitelhack, J. Jolie, R. Schulze, A. Türler, and T. Materna, "The new PGAA and PGAI facility at the research reactor FRM II in Garching near Munich," *J. Radioanal. Nucl. Chem.*, vol. 278, pp. 691–695, 2008.

[25] "Specifications of the integrated ADC/MCA developed at IKP, Universität zu Köln."

[26] "Hypermet PC, http://www.iki.kfki.hu/nuclear/hypc/index_en.shtml."

[27] Révay, Zs., Belgya, T., and Molnár, T., "Application of Hypermet-PC in PGAA," *J. Radioanal. Nucl. Chem.*, vol. 265, pp. 261–265, 2005.

[28] Molnár, T., Révay, Zs., and Belgya, T., "Wide energy range efficiency calibration method for Ge detectors," *Nucl. Instrum. Methods Phys. Res., Sect. A*, vol. 489, pp. 140–159, 2002.

[29] Révay, Zs., "Determining Elemental Composition Using Prompt Gamma Activation Analysis," *Anal. Chem.*, vol. 81, pp. 6851–6859, 2009.

[30] C. J. Glinka, J. W. Lynn, and R. Lindstrom, "PNPI Lithium-6 Fluoride/Polymer for Neutron Shielding Applications," tech. rep., National Institute of Standards and Technology, NIST.

[31] C. Yonezawa, A. K. H. Wood, M. Hoshi, Y. Ito, and E. Tachikawa, "The characteristics of the prompt gamma-ray analyzing system at the neutron beam guides of JRR-3M," *Nucl. Instrum. Methods Phys. Res., Sect. A*, vol. 329, pp. 207–216, 1993.

[32] R. L. Paul, R. M. Lindstrom, and A. E. Heald, "Cold neutron prompt gamma-ray activation analysis at NIST - Recent developments," *J. Radioanal. Nucl. Chem.*, vol. 215, pp. 63–68, 1997.

[33] S. Baecheler, P. Kudějová, J. Jolie, and J.-L. Schenker, "*The k0 method in cold-neutron prompt gamma activation analysis*," *J. Radioanal. Nucl. Chem.*, vol. 256, pp. 239–245, 2003.

[34] G. M. Sun, S. H. Byun, and H. D. Choi, "Prompt k_0-factors and relative gamma-emission intensities for the strong non-$1/v$ adsorbers ^{113}Cd, ^{149}Sm, ^{151}Eu and ^{155,157}Gd," *J. Radioanal. Nucl. Chem.*, vol. 256, pp. 541–552, 2003.

[35] Zs. Révay, "Comparison of the analytical sensitivities for non-$1/v$ elements in different neutron beams," *Nucl. Instrum. Methods Phys. Res., Sect. B*, vol. 263, pp. 79–84, 2007.

[36] "Database of Prompt Gamma Rays from Slow Neutron Capture for Elemental Analysis," tech. rep., Internaltional Atomic Energy Agency, 2007.

[37] N. E. Holden, "Temperature dependence of the Westcott g-factor for neutron reactions in activation analysis," *Pure Appl. Chem.*, vol. 12, pp. 2309–2315, 1999.

[38] J.-Ch. Sublet, J. Kopecky, and R. A. Forrest, "The European Activation File: EAF-99 cross section library, ukaea fusion, report ukaea fus 408, december 1998," tech. rep., UKAEA Fusion, Report UKAEA FUS 408,, 1998.

[39] A. Schmehl, V. Vaithyanathan, A. Herrnberger, S. Thiel, C. Richter, M Liberati, T. Heeg, M. Roeckerath, L. Fitting Kourkoutis, S. Muehlbauer, P. Boeni, D. A. Muller, Y. Barash, J. Schubert, Y. Idzerda, J. Mannhart, and D. G. Schlom, "Epitaxial integration of the highly spin-polarized ferromagnetic semiconductor EuO with silicon and GaN," *Nature Material*, vol. DOI:10.1038/nmat2012, 2007.

[40] T. Mairoser, A. Schmehl, A. Melville, T. Heeg, L. Canella, P. Böniand W. Zander, J. Schubert, D. E. Shai, E. J. Monkman, K. M. Shen, D. G. Schlom, and J. Mannhart, "Charge Carrier Induced Increase of the Curie Temperature of EuO - Is There an Intrinsic Limit?." submitted to Phys. Rev. Lett.

[41] R. W. Ulbricht, A. Schmehl, T. Heeg, J. Schubert, and D. G. Schlom, "Adsorption-controlled growth of EuO by molecular-beam epitaxy," *Appl. Phys. Lett.*, vol. 93, p. 102105, 2008.

[42] "Carcinogenic Risk In Occupational Settings (CRIOS)," November 2010.

[43] G. P. Lewis, W. J. Jusko, and L. L. Coughlin, "Cadmium accumulation in man: influence of smoking, occupation, alcoholic habit and disease," *J. Chron. Dis.*, vol. 25, pp. 717–726, 1972.

[44] G. F. Nordberg, B. A. Fowler, M. Nordberg, and L. Friberg, *Handbook on the toxicology of Metals*. Elsevier Science Publishers B. V., 2007.

[45] A. Stoica, B. S. Katzenellenbogen, and M. B. Martin, "Activation of Estrogen receptor-α by the Heavy Metal Cadmium," *Mol. Endo.*, vol. 14, pp. 545–553, 2000.

[46] M. D. Johnson, N. Kenney, A. Stoica, L. Hilakivi-Clarke, B. Singh, G. Chepko, R. Clarke, P. F. Sholler, A. A. Lirio, C. Foss, R. Reiter, B. Trok, S. Paik, and M. B. Martin, "Cadmium mimics the *in vivo* effects of estrogen in the uterus and mammary gland," *Nature Medicine*, vol. 9, pp. 1081–1084, 2003.

[47] X-5 Monte Carlo Team, *MCNP - A General Monte Carlo N-Particle Transport Code, Version 5. Los Alamos National Laboratory.* Los Alamos National Laboratory, 08 2005.

[48] K. Biró, "Non-destructive research in archeology," *J. Radioanal. Nucl. Chem.*, vol. 265, pp. 235–240, 2005.

[49] V. D. Poulios and D. D. Mengidis, "Lithochori of Kavala's Prefecture 2006. Excavation at Modern Via Egnatia," *AEMΘ*, vol. 20, pp. 151–163, 2006.

[50] V. D. Poulios, D.-D. Mengidis, and E. Kosmidou, "Lithochori of Kavala's Prefecture 2007. Excavation at Modern Via Egnatia," *AEMΘ*, vol. 21, p. in press, 2007.

[51] Y. Siouris, "Private communication."

[52] I. M. Siouris, S. Katsavounis, and K. Kosmidou, "Non-distructive PGAA elemental evaluation of metallic 1st century AD, Greco-Roman artefact and coins," tech. rep., Forschungs-Neutronenquelle Heinz Maier-Leibnitz, 2009.

[53] G. Gorini for the Ancient Charm Collaboration, "Ancient Charm: A research project for neutron-based investigation of cultural-heritage objects," *Il Nuovo Cimento*, vol. 30, pp. 47–58, 2007.

[54] R. Schulze, *Prompt Gamma-ray 3D-Imaging for Cultural Heritage Purposes.* PhD thesis, Universität zu Köln, 2010.

[55] S. Baechler, T. Materna, J. Jolie, P. Cauwels, M. Crittin, V. Hnkimaki, H. U. Johner, B. Masschaele, W. Mondelaers, J. Kern, and M. Piboule, "Non-destructive analysis of a bulky sample from a natural fossil reactor," *J. Radioanal. Nucl. Chem.*, vol. 250, pp. 39–45, 2001.

[56] P. Kudějová, *Two new installations for non-destructive sample analysis: PIXE and PGAA.* PhD thesis, Universität zu Köln, 2005.

[57] L. Canella, P. Kudějová, R. Schulze, A. Türler, and J. Jolie, "From Prompt Gamma Activation Analysis to Prompt Gamma Activation Imaging," tech. rep., Technische Universität München, Forschungs-Neutronenquelle Heinz Maier-Leibnitz, 2009.

[58] E. Jarosewich, "Chemical analysis of meteorites: a compilation of stony iron meteorite analysis," *Meteoritics*, vol. 25, pp. 323–337, 1990.

[59] G. Kallemeyn and J. T. Wasson, "The compositional classification of chondrites - i. The carbonaceous chondrite groups," *Geochim. Cosmochim. Acta*, vol. 45, pp. 1217–1230, 1981.

[60] W. Schmid, *Construction of a sputtering reactor for U-Mo fuel coating and tailored sample production.* PhD thesis, Technische Universität München, 2011.

[61] G. Molnár, Zs. Révay, and T. Belgya, "Non-destructive interrogation of uranium using PGAA ," *Nucl. Instrum. Methods Phys. Res., Sect. B*, vol. 213, pp. 389–393, 2004.

[62] J. Magill, G. Pfennig, and J. Galy, "Karlsruher Nuklidkarte, 7. Auflage 2006," 2006.

[63] R. Hengstler, "Thermal and electric conductivity of a monolitic uranium-molibdenum alloy for research reactor fuels," Master's thesis, Technische Universität München, 2008.

Acknowledgments

The first thanks goes to my supervisor Prof. Dr. Andreas Türler for the opportunity to do this work and for the freedom he gave me to develop my own ideas.
I would like to thank also Dr. Petra Kudejova for the introduction to this new technique.
Many thanks to the PGAA group in Budapest that trained me and helped me in the setting up the instrument here in Garching, in particular I would like to thank Dr. Zsolt Révay and Dr. Laszlo Szentmiklósi.
Concerning the PGAA measurements I have to thank many people that helped me: for the Cd measurements Dr. Roman Gernhäuser and Dr. med. Jutta Schöpfer, for the EuO(Gd) Dr. Andreas Schmehl, for the greek coins Dr. Ioannis M. Siouris, and for the UMo measurements the whole HEU-MEU group at FRM II.
I also acknowledge the interest and support of Prof. Dr. Jan Jolie, university of Cologne, and Prof. Dr. Winfried Petry, director of FRM-II.
And finally I would like to thank also Dipl. Phys. Franz Wagner for all the interesting talks and last-minute experiments.

Special acknowledgments

"Ich habe fertig!"
This PhD was the best adventure I ever had in all possible meanings.
This page is dedicated to special thanks...
A special thanks goes to Dr. Ralf, for the immense opinions exchange and the great teamwork at the PGAA facility (lead job, tequila and PC destruction) :-).
Another super-special "grazie" to my office room-mates: Wolfgang for his "niveau-limbo" skills, the ROFL-copters and the nice talks, Harald for his infinite help in any occasion and especially for my new passion for climbing, Rosi for the female support between all the guys and the nice chat, Robert because he is just the scheissRobert (no offense!), Rainer for his good tips on cars, Bombing Bogi-Christian without his laugh the office is empty, Stefan as colleague and friend in the PGAA misadventures and then Jürgen, Toni, Stefan2, Marta (my favorite latina), Michi, Tom and all the other!
How can I forget the Strahlenschutzbüro! Thank you all for the immense support at the PGAA! Martina and Christian, well we met exactely at the FRM II! Work bring also new friends sometimes :-)
A very important thanks goes to my Family, and now i have to write in italian: Un grazie gigante alla mia famiglia in Italia che hanno sempre creduto in me e non mi hanno mai lasciato sola anche con 500 km tra di noi. Grazie Mamma, Papa' e Deia!
I miei amicicci italiani, Sara prima fra tutti nonostante la lontananza.
And then the last but not the less important Mr. Ronny Preuss.... my big luck and big desperation! I would have never met him without this PhD. I thank him mainly because he stayed with me in this crazy time without killing me. :-) He is my chocolate planet in the universe of neutrons!
A small thank also to Flippi my favorite, white and hairy room-mate.
And finally i would like to thank myself for the job, for the german, for the never ending energy, for the patience and for the courage.

1095 days, 835 μSv, hundreds kg of lead...one girl!